NON-NORMAL DYNAMICS AND HYDRODYNAMIC STABILITY

A Dissertation

Presented to the Faculty of the Graduate School

of Cornell University

in Partial Fulfillment of the Requirements for the Degree of

Doctor of Philosophy

by

Jeffrey Scott Baggett

August 1996

NON-NORMAL DYNAMICS AND HYDRODYNAMIC STABILITY

Jeffrey Scott Baggett, Ph.D.

Cornell University 1996

This thesis explores the interaction of non-normality and nonlinearity in continuous dynamical systems. A solution beginning near a linearly stable fixed point may grow large by a linear mechanism, if the linearization is non-normal, until it is swept away by nonlinearities resulting in a much smaller basin of attraction than could possibly be predicted by the spectrum of the linearization. Exactly this situation occurs in certain linearly stable shear flows, where the linearization about the laminar flow may be highly non-normal leading to the transient growth of certain small disturbances by factors which scale with the Reynolds number.

These issues are brought into focus in Chapter 1 through the study of a two-dimensional model system of ordinary differential equations proposed by Trefethen, *et al.* [*Science*, **261**, 1993].

In Chapter 2, two theorems are proved which show that the basin of attraction of a stable fixed point, in systems of differential equations combining a non-normal linear term with quadratic nonlinearities, can decrease rapidly as the degree of non-normality is increased, often faster than inverse linearly.

Several different low-dimensional models of transition to turbulence are examined in Chapter 3. These models were proposed by more than a dozen authors for a wide variety of reasons, but they all incorporate non-normal linear terms and quadratic nonlinearities. Surprisingly, in most cases, the basin of attraction of the "laminar flow" shrinks much faster than the inverse Reynolds number.

Transition to turbulence from optimally growing linear disturbances, streamwise vortices, is investigated in plane Poiseuille and plane Couette flows in Chapter 4. An explanation is given for why smaller streamwise vortices can lead to turbulence in plane Poiseuille flow. In plane Poiseuille flow, the transient linear growth of streamwise streaks caused by non-normality leads directly to a secondary instability.

Certain unbounded operators are so non-normal that the evolution of infinitesimal perturbations to the fixed point is entirely unrelated to the spectrum, even as $t \to \infty$. Two examples of this phenomenon are presented in Chapter 5.

BIOGRAPHICAL SKETCH

Jeffrey Scott Baggett was born and raised in Hermiston, Oregon. After nearly failing kindergarten, Jeff fared better in school. He did not want to go to college after graduating from Hermiston High School, but Jeff's parents sent him packing to the University of Portland, where in 1990, he received a B.S. in mathematics. This time, without his parents urging, Jeff found his way to Cornell University to pursue a doctorate in Mathematics. In 1993 he received a Master's in mathematics from Cornell. In 1996, twenty-two years after his wobbly start in education, Jeff earned his Ph.D. in mathematics under the supervision of Lloyd N. Trefethen. He will continue his education as a postdoctoral researcher in the Center for Turbulence Research at Stanford University.

For Mom and Dad, who knew me better than I did.

ACKNOWLEDGEMENTS

This thesis would not have been possible without the guidance, support, and boundless enthusiasm of Nick Trefethen. His constant friendship and encouragement helped me to excel. Nick's many careful readings of drafts of this thesis, and the resulting suggestions, were invaluable. I could not have hoped for a better teacher.

Much of the work in this thesis originated from collaborations and discussions with Nick. Chapter 4 was motivated by work with Satish Reddy and Peter Schmid. The investigations in Chapter 4 were made possible by the Navier–Stokes simulation code of Anders Lundbladh, Dan Henningson, and Arne Johansson, and the linear stability analysis code written by Satish. The simulations were made feasible by Anne Trefethen, who ported the code to the IBM SP2 at Cornell's Theory Center, and for whose support I am also grateful. I thank Sid Leibovich and Fabian Waleffe for many discussions about hydrodynamic stability, and also thank Nick, John Guckenheimer and Lars Wahlbin for their service on my committee.

Financially this work was supported in part by NSF Grant DMS-9500975CS, NSF Grant DMS-9116110, DOE Grant DE-FG02-94ER25199, and ARO Grant DAAL03-91-C0027.

There are many people whose friendship and help were indispensable; among them are Shirley Allen, Ed Bueler, Patty Hough, Kaila Patel, Dolores Pendell, Ivelisse Rubio, Hal Schenck, Eric Shrader, and Katy Simonsen. I am especially grateful to my academic siblings Toby Driscoll and Kim-Chuan Toh.

I could never thank my family enough for their years of love and support, and my fiancée Jennifer, who was with me every step of the way.

Table of Contents

1 Introduction **1**
1.1 Instability and transition to turbulence of flows in pipes and channels 2
1.2 A two-variable model problem 7
1.3 Outline of the thesis 14

2 Non-normality meets nonlinearity: The shrinking basin of attraction **16**
2.1 The mathematical setting 18
2.2 Bounds based on $\|e^{tA}\|$ 21
2.3 Bounds based on eigenvectors 25
2.4 A model problem 29
2.5 Infinite dimensions 33

3 Low-dimensional models of subcritical transition to turbulence **35**
3.1 Models without selection rules 39
3.1.1 The TTRD model 40
3.1.2 The BDT model 44
3.1.3 The GG model 46
3.2 Models with selection rules 49
3.2.1 The BT model 50
3.2.2 The W model 52
3.2.3 The KLH model 56
3.2.4 The JRB model 58
3.2.5 The W2 model 60
3.3 Why these figures all look alike 63
3.4 Summary 66

4 Why plane Poiseuille flow is less stable than plane Couette flow: The dual nature of shear **68**
4.1 Streamwise vortices and streaks in transition to turbulence 68

4.2 Streak generation 77
4.3 Streak breakdown 81
4.4 Direct numerical simulations of the streak instability 88
4.5 Linear stability analysis of the streak instability 95
4.6 The threshold scaling in plane Poiseuille flow 103
4.7 The threshold scaling in plane Couette flow 105
4.8 Conclusions 112

5 Pseudospectra of the Hille-Phillips operator 114

5.1 $\|e^{tA}\|$ as $t \to \infty$ and pseudospectra 115
5.2 The Zabczyk operator 119
5.3 The Hille–Phillips operator 122
5.4 Computations 125
5.5 A corollary 129

A Outline of numerical methods used in streak stability investigations 131

A.1 Direct numerical simulations 133
A.2 Simulations with frozen streamwise independent velocity field . . . 139
A.3 Matrix analysis methods 140

Bibliography 143

List of Tables

3.1 Summary of the models and some of their properties. 66

A.1 The numerical method used to generate each figure in Chapter 4 . 132

List of Figures

1.1 Transient linear growth in plane Couette flow. 6
1.2 Transient linear growth for a model problem 8
1.3 Nonlinear behavior of solutions to the model problem. 9
1.4 Global phase portrait for the system (1.2) with $R = 10$. 10
1.5 Phase portraits near the origin for the system (1.2). 11
1.6 Stable manifolds of the saddle points for the system (1.2) 12
1.7 Stable manifolds, near the origin, of the saddle points for system (1.2). 13

2.1 $\|e^{tA}\|$ for a typical non-normal matrix A. 19
2.2 Comparison of unit balls in the the Euclidean norm and the V-norm. 26
2.3 Comparison of the theoretical lower bounds for a model problem . 32

3.1 Schematic view of transition to turbulence as non-modal amplification and nonlinear mixing. 40
3.2 Evolution curves for model (TTRD). 42
3.3 Evolution curves for model (BDT). 45
3.4 Evolution curves for model (GG). 46
3.5 Evolution curves for model (BT). 51
3.6 Schematic view of a self-sustaining mechanism of turbulence developed at the Center for Turbulence Research 53
3.7 Evolution curves for model (W). 54
3.8 Evolution curves for model (KLH). 57
3.9 Evolution curves for model (JRB). 59
3.10 Evolution curves for model (W2). 61

4.1 Energies in selected wave components for transition to turbulence in plane Couette flow. 71
4.2 Neutral stability curves for linear instability of streaks and transition to turbulence (adapted from [79]). 72
4.3 Streamwise streaks evolve into wavy streaks in plane Couette flow . 73
4.4 Formation of vertical vortices in plane Couette flow. 75

4.5 The shear tilting mechanism. 78
4.6 Optimal streamwise vortices in plane Couette flow. 79
4.7 Optimal streamwise vortices in plane Poiseuille flow 80
4.8 Streamwise streaks in plane Couette flow. 81
4.9 Streak "roll up" for the inviscid model problem. 85
4.10 "Roll up" of vertical vortices in plane Couette flow. 86
4.11 Streak instability growth rates versus initial vortex amplitudes in plane Couette flow; from Navier–Stokes simulation 91
4.12 Neutral stability curve for linear instability of streamwise streaks in plane Couette flow. 92
4.13 Streak instability growth rates versus initial vortex amplitudes in plane Poiseuille flow; from Navier–Stokes simulation. 93
4.14 Neutral stability curve for linear instability of streamwise streaks in plane Poiseuille flow. 94
4.15 Streak instability growth rates versus initial vortex amplitudes in plane Couette flow; from linear stability analysis. 98
4.16 Spectra of the streak instability operator in PCF. 99
4.17 Comparison of streak instability growth rates as computed by linear stability analysis and Navier–Stokes simulations. 100
4.18 A vertical vorticity component of the eigenfunctions. 101
4.19 Spectrum of the streak instability operator in PPF. 102
4.20 Comparison of streak profiles from Navier–Stokes simulation with model streak profiles. 109
4.21 Neutral stability curves for the streak instability in the streaks model for plane Couette flow. 110

5.1 Pseudospectra of the Zabczyk operator 119
5.2 Evolution norms for the Zabczyk operator. 121
5.3 Pseudospectra of the Hille–Phillips operator 123
5.4 Model of the pseudospectra of the Hille–Phillips operator 124

Chapter 1

Introduction

This dissertation explores the interaction of non-normality and nonlinearity. Mathematically, these are fundamental notions of dynamical systems. In science and engineering, they appear in numerous fields where the stability and instability of time-dependent systems are important, for example, in fluid dynamics, plasma physics, and weather forecasting. The motivation for this dissertation, however, is one particular scientific problem in which the interaction of non-normality and nonlinearity plays a central role: the problem of instability and transition to turbulence of shear flows.

This dissertation makes four principal contributions. One (Chapter 5) is solely mathematical, one (Chapter 4) is primarily physical, and the other two lie in between, concerning mathematical developments motivated by the fluids problem in question but of potentially wider applicability. In this Introduction, we begin with the physical motivation, describing the problem of transition to turbulence of shear flows in pipes and channels, whose curious history stretches back well over a century. We then bring some of the mathematical issues into focus by presenting as a model a two-variable system of ordinary differential equations that illustrates how non-normality and nonlinearity may combine to yield surprising results. We conclude with an outline of the dissertation.

1.1 Instability and transition to turbulence of flows in pipes and channels

In a series of experiments in 1883, Reynolds [83] observed three different flow regimes in water flow through a circular pipe. Reynolds injected a stream of ink near the pipe inlet and followed the path of the ink as it flowed downstream. At sufficiently low velocities "the streak of colour extended in a beautiful straight line through the tube," showing that the flow was laminar. At intermediate velocities "the streak would shift about the tube, but there was no appearance of sinuosity." At higher velocities "the colour band would all at once mix up with the surrounding water," that is, the flow was turbulent. Reynolds demonstrated, in his experiment, that the laminar flow broke down when the ratio of inertial force to viscous force, a dimensionless quantity now known as the Reynolds number, exceeded approximately 13000.

Despite over a century of research, the problem of explaining the phenomenon of transition to turbulence is not fully solved. Why a given flow becomes turbulent and at what Reynolds number are still largely open questions. The traditional approach to this problem, developed by Kelvin [47], Stokes, and Rayleigh [76] in the 1880's, is normal mode analysis. This consists of linearizing the Navier–Stokes equations about the laminar flow, diagonalizing the resulting operator, and looking for eigenvalues in the unstable half plane. If there is a smallest Reynolds number R at which an eigenvalue first crosses into the unstable complex half-plane, this is known as the critical Reynolds number, R_c.

Normal mode analysis accurately predicts the onset of instabilities for some flows, notably Taylor–Couette flow, that is, flow between concentric rotating cylinders, and Rayleigh–Bénard convection, that is, convection driven by a temperature gradient between parallel plates. However, for some flows, notably many parallel shear flows, transition to turbulence occurs at theoretically subcritical Reynolds numbers R. In plane Couette flow, that is, flow between oppositely moving infinite parallel walls, eigenvalues predict a critical number $R_c = \infty$ [86], yet transition is observed for R as low as 280 [60], though values of R in the range $325 \leq R \leq 370$ [17, 19, 92] are more typical. For pipe Poiseuille flow, that is, flow driven by a pressure gradient in an infinite cylindrical pipe, the critical Reynolds number is again $R_c = \infty$ (though a mathematical proof of this has yet to be obtained), but Reynolds observed transition for $R \approx 13000$ and transition can be observed for R as low as 2000 [100, 101]. Even in the case of plane Poiseuille flow, that is, flow driven by a pressure gradient between infinite parallel walls, for which $R_c = 5772$, transition is observed for R as low as 1000 [20] (or as high as 8000 [69]).

With the failure of the classical linear analysis, nonlinear theories such as weakly nonlinear theory, secondary instability theory, and global energy methods were proposed to shrink the gap between theory and experiments. Weakly nonlinear theory predicts a nonlinear critical Reynolds number of 2935 in plane Poiseuille flow [41]. Secondary instability theory based on Tollmien–Schlichting waves is successful at predicting transition from artificially generated two dimensional disturbances [71], but natural transition is three dimensional from the onset [52]. Global energy methods establish Reynolds numbers below which all disturbances monotonically decay, but these are far lower than the critical Reynolds numbers observed in experiments. The interested reader can learn about the details and history of normal mode analysis in [22].

While eigenvalues may fail to predict the onset of instabilities which lead to turbulence in certain parallel shear flows, this does not mean that the linear analysis is meaningless. The eigenvalues yield information about the behavior of certain perturbations as $t \to \infty$. However, some important linear effects, unrelated to the eigenvalues, occur at *finite* times. Small perturbations to the laminar flow may undergo linear transient growth, that is, there may be structures which grow algebraically, independent of their initial amplitude, before decaying due to the effects of viscosity. Physically, the possibility of linear transient growth has been known since at least 1907 [70], but the mathematical description has lagged behind. Sometimes, algebraic growth has been attributed to degeneracies and exact resonances in the spectrum of the linearized Navier–Stokes equations [5, 31, 32, 34, 87, 90]. However, resonances and degeneracies only appear at particular parameter combinations, while the underlying physical phenomena are much more robust [78]. An equally robust mathematical framework was needed.

A new mathematical explanation for transient linear growth has emerged recently [7, 11, 78, 95]. This idea questions the use of eigenvalues in normal mode analysis rather than the linearization itself, because in the case of parallel shear flows, the linearized operator can be highly non-normal — its eigenvectors can be far from mutually orthogonal. A consequence of the non-normality is that even when all the eigenmodes asymptotically decay, solutions can exhibit transient linear growth by factors that scale with the Reynolds number, even in the absence of degeneracies or resonances in the spectrum. Figure 1.1 illustrates the possibility of transient linear growth due to non-normality in plane Couette flow. Shown is the norm of the linearized operator governing the evolution of small purely streamwise disturbances at a particular spanwise wavenumber.

Finally, we arrive at the context for this thesis. Many of the studies of algebraic or linear transient growth of small perturbations to the laminar flow have not included nonlinear effects. In this thesis, we consider the interaction of linear algebraic growth caused by non-normality with nonlinearity. In linearly stable shear flows, one of the consequences of this interaction is that increasingly small perturbations may lead to transition to turbulence as the Reynolds number increases. The idea that the basin of attraction of the laminar flow decreases in size as R increases dates to Lord Kelvin in 1887 [48], who wrote "It seems probable, almost certain indeed, that... the steady motion is stable for any viscosity, however small; and that the practical unsteadiness pointed out by Stokes forty-four years ago, and so admirably investigated by Osborne Reynolds, is to be explained by limits of stability becoming narrower and narrower the smaller is the viscosity."

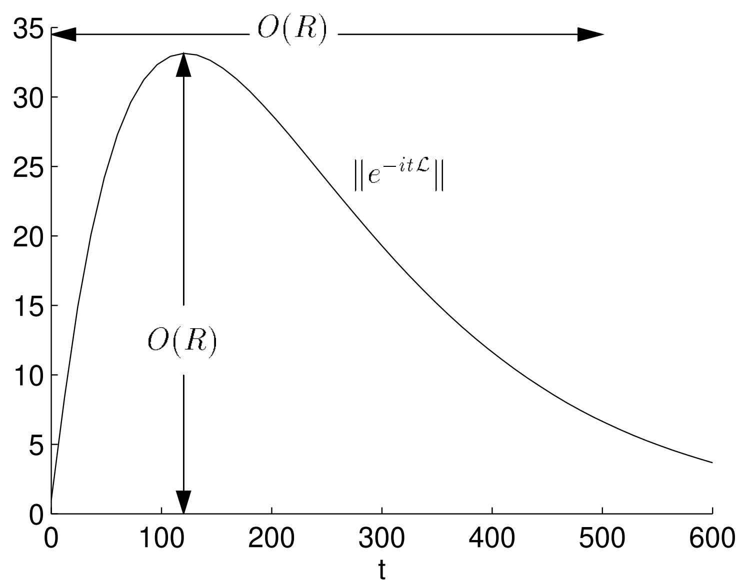

Figure 1.1: Transient linear growth in plane Couette flow. Shown is $\|e^{-it\mathcal{L}}\|$ versus t, where $\mathcal{L}$ is the linear operator governing the evolution of purely streamwise infinitesimal perturbations with fixed spanwise wavenumber 2 in plane Couette flow with Reynolds number 1000. The curve $\|e^{-it\mathcal{L}}\|$ is the envelope of all solutions $\|e^{-it\mathcal{L}}v\|$ with $\|v\| = 1$, where $\|\cdot\|$ is the energy norm. The spectrum of $\mathcal{L}$ is contained in the negative imaginary half-plane, so all solutions asymptotically decay.

Trefethen, *et al.* [95] attempted to quantify this phenomenon, conjecturing that the size of smallest perturbation to the laminar flow which can lead to turbulence in shear flows such as plane Couette flow, plane Poiseuille flow, pipe Poiseuille flow and related flows scales as

$$\epsilon_{\text{min}} = O(R^{\alpha}) \tag{1.1}$$

for some $\alpha < -1$, where the size of a perturbation is measured in the energy norm. We refer to α, for a given flow, as the *threshold exponent.* (In the case of plane Poiseuille flow, this refers to transition mechanisms unrelated to the linear instability of Tollmien–Schlichting waves for $R > 5772$.) This conjecture has been confirmed in plane Couette flow and plane Poiseuille flow. In plane Couette flow, Lundbladh, Henningson and Reddy [62] used direct numerical simulations to show that a pair of oblique waves of size $O(R^{-5/4})$ can lead to turbulence, thus showing that $\alpha \leq -5/4$ for plane Couette flow. They also showed that optimal streamwise vortices or a pair of oblique waves of size $O(R^{-7/4})$ lead to turbulence in direct numerical simulations at subcritical Reynolds numbers in plane Poiseuille flow.

This thesis has two primary emphases. One is the explanation of the mathematical and physical aspects of subcritical transition to turbulence that might lead to threshold exponents $\alpha < -1$ in plane Couette flow, plane Poiseuille flow, and pipe Poiseuille flow (though we do not discuss the latter in this thesis). The second is the demonstration that the algebraic growth caused by non-normality of certain perturbations to the laminar flow leads to interesting nonlinear effects — that non-normality triggers nonlinearities.

1.2 A two-variable model problem

In order to clarify the mathematical issues and to demonstrate how non-normality and nonlinearity can combine to yield interesting effects, we examine a model problem proposed by Trefethen, *et al.* [95]. This two-dimensional system,

$$\begin{aligned} \frac{d}{dt}\mathbf{x} &= A\mathbf{x} + \|\mathbf{x}\|B\mathbf{x} \\ &= \begin{pmatrix} -R^{-1} & 1 \\ 0 & -2R^{-1} \end{pmatrix}\mathbf{x} + \|\mathbf{x}\|\begin{pmatrix} 0 & -1 \\ 1 & 0 \end{pmatrix}\mathbf{x}, \end{aligned} \tag{1.2}$$

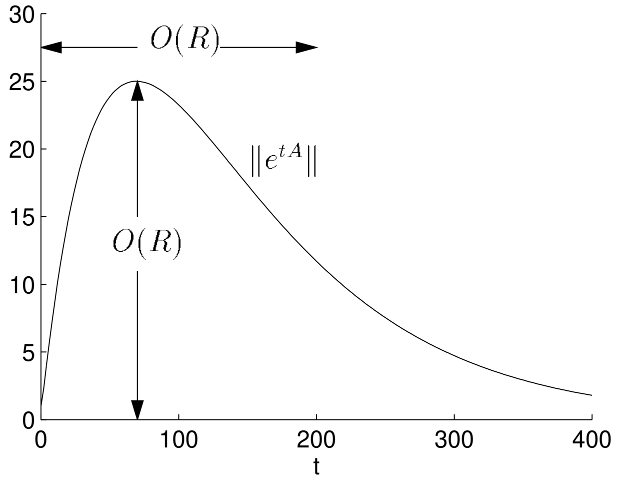

Figure 1.2: Transient linear growth for the model problem (1.2) with R = 100. Shown is $\|e^{tA}\|$, where A is the linearization (1.3) at the origin.

with $R > 0$, $\mathbf{x} = (x, y)^T$, and $\|\mathbf{x}\|^2 = x^2 + y^2$, was proposed as a model of the interaction of linear, non-modal effects and nonlinearities in the equations governing the evolution of disturbances to the laminar solution in plane shear flows such as plane Couette flow and plane Poiseuille flow.

Linearizing this system at the origin, which corresponds to the laminar solution, yields

$$\frac{d}{dt}\mathbf{x} = A\mathbf{x} = \begin{pmatrix} -R^{-1} & 1 \\ 0 & -2R^{-1} \end{pmatrix} \mathbf{x}. \tag{1.3}$$

The terms in (1.2) are chosen to resemble certain aspects of the Navier–Stokes equations for disturbances to the laminar solution. The linear term, involving the matrix A, amplifies energy transiently. The nonlinear term, involving the skew-symmetric matrix B, rotates energy in the x-y-plane but acts orthogonally to the

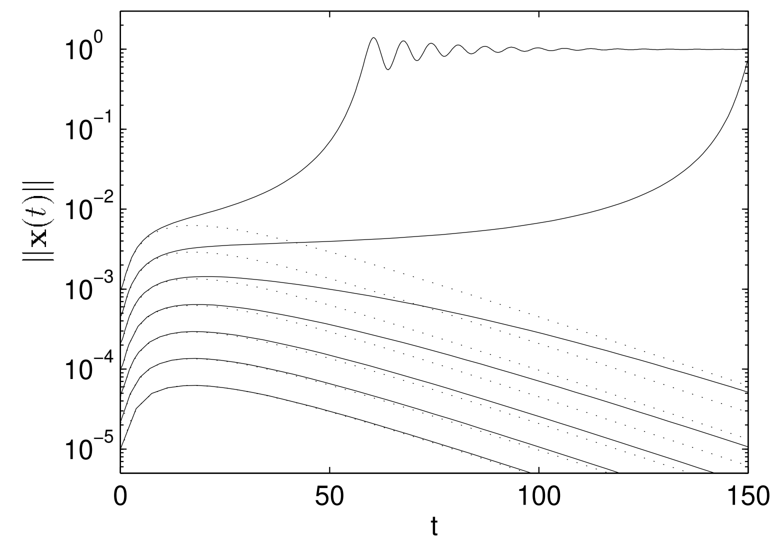

Figure 1.3: Nonlinear behavior of solutions to the model problem (1.2). Shown is the norm of solutions $\|\mathbf{x}(t)\|$ with $R = 25$ and initial conditions of the form ϵv, where v is the optimal input as described in the text. The threshold amplitude for "transition" is $\|\mathbf{x}(0)\| \approx 4.23 \times 10^{-4}$. The dotted lines show the effect of removing the nonlinear term from (1.2).

motion and does not contribute to the energy of solutions.

For any given initial condition $\mathbf{x}(0) = v$, the solution to the linearized problem (1.3) is given by $\mathbf{x}(t) = e^{tA}v$ and has amplitude $\|\mathbf{x}(t)\| = \|e^{tA}v\|$. The operator norm $\|e^{tA}\|$, as shown in Figure 1.2, is the envelope of all such amplitude curves with $\|v\| = 1$. For any given t, there exists a vector v with $\|v\| = 1$ such that $\|e^{tA}v\| = \|e^{tA}\|$. The optimal input vector v is called the principal right singular vector, and the corresponding normalized output $u = e^{tA}v/\|e^{tA}v\|$ is the principal left singular vector. As indicated in Figure 1.2, some solutions to the linearized problem (1.3) are amplified by a factor $O(R)$ over time $O(R)$, because of the non-normality of A, before decaying as predicted by the eigenvalues. In that figure $R =$

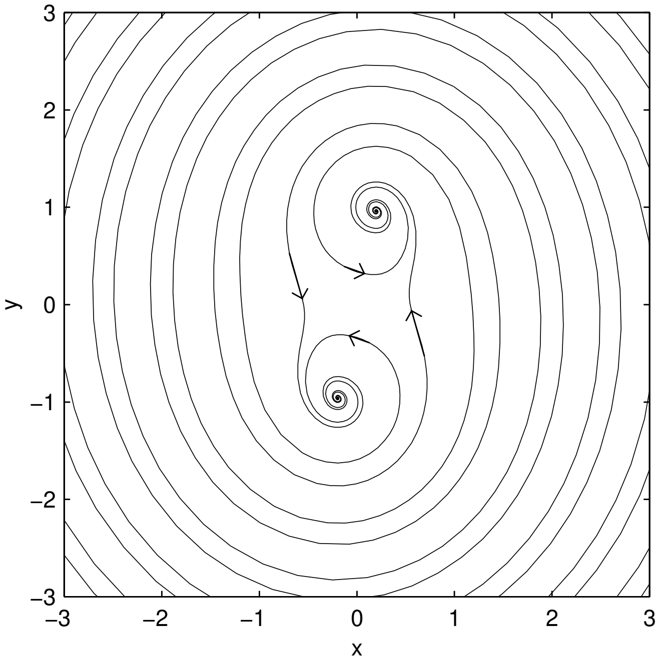

Figure 1.4: Global phase portrait for the system (1.2) with $R = 10$. Most trajectories tend to one of two sinks located at distance $O(1)$ from the origin. (The next three figures detail the further structure of the phase portrait near the origin.)

100, and the maximum growth, by a factor of 25.6, is achieved at $t_{\max} = 66.0$. The right singular vector which achieves the optimal growth at $t_{\max}$ is $v = (0.20, 0.98)^T$.

Remarkably, solutions of the full system (1.2) can experience much greater amplitude growth than those of the linearized problem. Figure 1.3 presents the norms $\|\mathbf{x}(t)\|$ for solutions to (1.2), with $R = 25$, starting from initial conditions $\mathbf{x}(0) = \epsilon v$, where $v = (0.0800, 0.9968)^T$ is the optimal input for achieving the most linear amplitude growth, that is, v is the right singular vector of $e^{t_{\max} A}$, with $t_{\max} = 17.2$. The dotted lines represent the norms of solutions to the linearized problem with the same initial conditions. For initial conditions with $\|\mathbf{x}(0)\| \leq 10^{-4}$, the evolution is

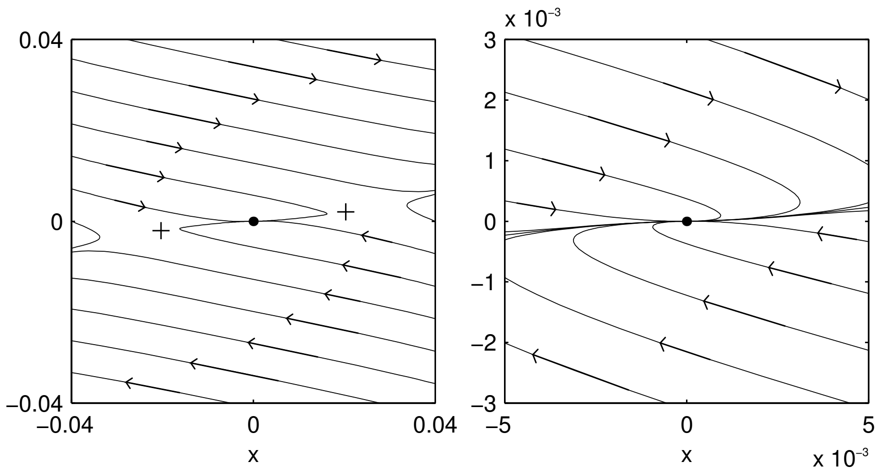

Figure 1.5: Phase portraits near the origin for the system (1.2) with $R = 10$. The left plot shows the dynamics in a neighborhood of the origin, where there are two saddle points denoted by $+$'s. The right plot shows the phase space very near the origin, where the linearized system (1.3) governs the dynamics.

essentially linear. For $\|\mathbf{x}(0)\| \gtrapprox 4.22 \times 10^{-4}$, the nonlinearity becomes important; the solutions do not decay but blow up to a critical point of size ≈ 1. However, even at amplitudes above the threshold, the evolution of solutions for small times is essentially linear, as indicated by the close correspondence between the dotted (linear) and solid (nonlinear) curves for small times.

Suppose $\mathbf{x}(0)$ is the vector of amplitude ϵ, a multiple of the principal right singular vector, that excites maximal growth in the linearized problem (1.3). After time $O(R)$, the solution has grown to size $O(\epsilon R)$ by the non-modal linear growth mechanism but has moved into a direction that no longer excites linear growth. Simultaneously, the nonlinear term has moved some of this energy back in the original direction, with amplitude $O(R) \times O((\epsilon R)^2) = O(\epsilon^2 R^3)$ because the nonlinearity is quadratic and acts over time $O(R)$. If the output of this nonlinear process is larger

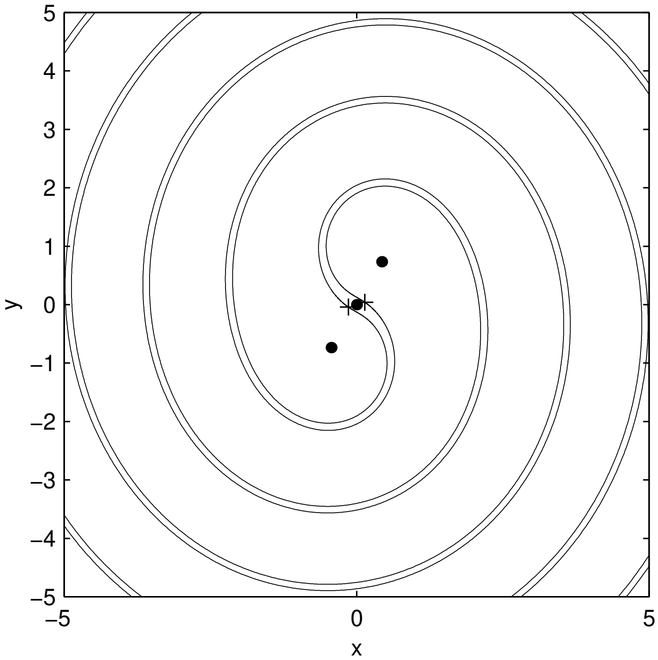

Figure 1.6: Stable manifolds of the saddle points for the system (1.2) with $R = 4$. The basin of attraction of the fixed point at the origin, analogous to the laminar state in a pipe or channel flow, is a narrow spiral whose width shrinks in proportion to R^{-3} as $R \to \infty$.

than the original input, that is, if $O(\epsilon^2 R^3) > \epsilon$, then there is enough energy in the original direction for the cycle to begin anew, resulting in sustained growth. Therefore, the interaction of linear, non-modal growth and nonlinearities yields a threshold amplitude $\epsilon = O(R^{-3})$.

To gain further insight into the interaction of non-normality and nonlinearity for this problem, we consider the phase space as depicted in Figures 1.4–1.5 for the system (1.2) with $R = 10$. Figure 1.4 shows the global phase space, where most of the action is due to the nonlinear terms, which rotate energy counter-clockwise. Most trajectories tend towards a pair of sinks at a distance $O(1)$ from the origin. In

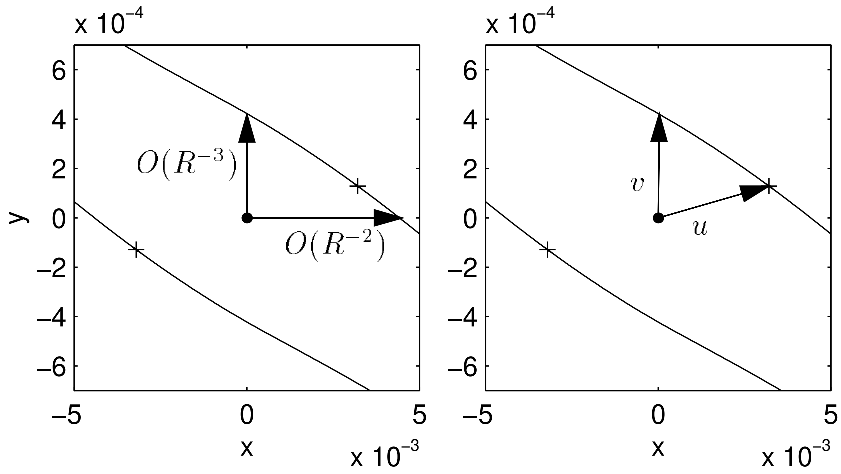

Figure 1.7: Stable manifolds of the saddle points of (1.2) near the origin, with $R = 25$. The left plot shows the region near the origin, including the symmetrically located saddles at $\approx \pm(2R^{-3}, 2R^{-2})$. These stable manifolds define the basin of attraction of the origin, which is extremely narrow, especially in the vertical direction, due to the interplay of non-normality and nonlinearity. The right plot is similar except that the arrows labeled v and u point in the directions of the right (optimal input) and left (output) principal singular vectors of $e^{t_{\max}A}$. The right singular vector v lies approximately in the direction in which the basin of attraction is narrowest, and the left singular vector lies approximately in the direction of the saddle point.

Figure 1.5 the left plot shows a magnified view of the phase space near the origin, including a pair of saddle points at $\approx \pm(2R^{-2}, 2R^{-3})^T$. The right plot is a highly magnified view of the phase space near the origin, where the behavior is essentially linear.

The stable manifolds of the pair of symmetrically located saddle points form the boundary of the basin of attraction of the origin. They are located at a distance $O(R^{-3})$ from the origin, showing that non-normality and nonlinearity combine to make the basin of attraction quite narrow. Figure 1.6 shows a large-scale portrait of the phase space for system (1.2), including the saddle points and their associated manifolds with $R = 4$. For R larger than ≈ 10, the two manifolds would be virtually indistinguishable to plotting accuracy. Figure 1.7 shows the saddle points and manifolds in a magnified view of the origin with $R = 25$ (the same value of R as in Figure 1.3).

1.3 Outline of the thesis

This thesis explores some of the physical and mathematical issues touched upon in the last two sections, with the aim of contributing to an understanding of subcritical transition to turbulence in shear flows. In Chapter 2 we consider systems of ordinary differential equations like (1.2) that can be written, at a stable fixed point, as a combination of a non-normal linear term and a quadratic nonlinearity. We use various measures of non-normality to give lower bounds on the size of the basin of attraction at the stable equilibrium. Generally speaking, increasing non-normality decreases the basin of attraction, often faster than inverse linearly.

Chapter 3 examines several low-dimensional systems of ordinary differential equations, generalizations of (1.2), that have been proposed as models of subcritical transition to turbulence. In particular, these models all lead to predictions $\alpha \leq -1$ of the threshold exponent for subcritical transition to turbulence, even though they were constructed for disparate reasons. As we will briefly discuss, some of these models also capture a remarkable amount of the physics of certain routes to turbulence.

Chapter 4 turns from model problems to the actual Navier–Stokes equations of fluid mechanics. Small streamwise vortices can generate linearly unstable streamwise streaks in the early stages of transition to turbulence in plane Couette flow and plane Poiseuille flow. The threshold amplitude of the critical vortices is much smaller in plane Poiseuille flow. We explain the different threshold amplitude scalings of the streamwise vortices and discover that shear has a dual nature in these flows. Shear is responsible for streak generation, but it also inhibits the streak instability.

Finally, in Chapter 5 we consider a more mathematical topic having to do with extreme cases of non-normality. Hille and Phillips [43] and Zabczyk [104] have constructed linear operators A that generate C_0-semigroups e^{tA} with the property that the asymptotic dynamics of e^{tA} are entirely unrelated to the spectrum of A. These operators A are extremely non-normal. In Chapter 5 we present numerically computed plots of the pseudospectra of these operators, which explain graphically the anomalous asymptotic behavior of e^{tA}.

Chapter 2

Non-normality meets nonlinearity: The shrinking basin of attraction

The stability of an equilibrium solution of a finite dimensional system of ordinary differential equations is traditionally investigated by considering a linearized system of the form

$$\frac{d}{dt}x = Ax$$

(we can assume the origin is the fixed point of interest). If the eigenvalues of the matrix A all have negative real parts, then the equilibrium is an asymptotically stable fixed point. However, this stability may apply only to trajectories beginning in a small neighborhood of the equilibrium solution. The limited region of validity of the eigenvalues is usually blamed on nonlinearity, and of course, this is true in the sense that if there were no nonlinearity, then the linear prediction would be globally valid.

As the model problem (1.2) of Section 1.2 illustrates, however, if A is non-normal — its eigenvectors are not orthogonal or equivalently A does not commute with its adjoint — then it may happen that certain initial conditions can grow *linearly* by potentially several orders of magnitude, even though the eigenvalues of A all lie the stable complex half-plane. A solution starting near the fixed point may grow large by a linear mechanism until it is swept away by nonlinearities.

This interaction of nonlinearity with linear, non-modal transient growth caused by non-normality can result in a much smaller basin of attraction for the stable fixed point than if A were normal. Thus, if A is highly non-normal, then one should be cautious about conclusions drawn from the eigenvalues. The eigenvalues of the linearized system reveal information about the behavior of solutions beginning sufficiently close to the equilibrium point as $t \to \infty$. If A is non-normal, then the behavior of solutions to the linearized system can be much different for finite times than as $t \to \infty$. This does not necessarily mean that the linearized system should be abandoned in attempting to draw conclusions about the basins of attraction of stable equilibria in the fully nonlinear system, rather, that one should take into account the effects of non-normality. This is the subject of this chapter. In a sequence of theorems we shall estimate the size of the basin of attraction of a stable equilibrium in a system combining non-normality with nonlinearity.

We begin by describing the mathematical setting in Section 2.1. In Sections 2.2–2.3, we introduce several different measures of non-normality and use them to derive lower bounds on the size of the basin of attraction of a stable fixed point. For each measure of non-normality, increasing the degree of non-normality can decrease the size of the basin of attraction, often faster than inverse linearly. In Section 2.4 we apply these techniques to the model problem from Section 1.2 and compare the results to the exact bounds achieved by a rescaling of the problem. Finally, in Section 2.5 we consider to what extent these techniques may be applied to infinite dimensional systems of ordinary differential equations such as the Navier–Stokes equations.

2.1 The mathematical setting

For the sake of simplicity, we consider finite dimensional systems with linear and quadratic terms. Without loss of generality, $x = 0$ can be taken as the fixed point of interest. Consider the system:

$$\frac{d}{dt}x = Ax + q(x), \quad x(0) = x_0, \tag{2.1}$$

where $A \in \mathbb{C}^{n\times n}$, $x, x_0 \in \mathbb{C}^n$, and q has the properties[1]

$$q(\alpha x) = \alpha^2 q(x), \quad \text{for all } \alpha \in \mathbb{R}, \text{ for all } x \in \mathbb{C}^n, \tag{2.2}$$

and,

$$\|q(x)\| \leq C\|x\|^2, \quad \text{for some } C \geq 0, \text{ for all } x \in \mathbb{C}^n. \tag{2.3}$$

If q satisfies (2.2), then condition (2.3) is equivalent to q being continuous. If q is quadratic, for instance, then (2.2) and (2.3) are trivially satisfied. Unless otherwise noted, $\|\cdot\|$ denotes the usual Euclidean norm on $\mathbb{C}^n$.

[1] We could easily generalize our results to more general nonlinearities by assuming that $q(x)$ is continuous and $q(\alpha x) = \alpha^\sigma q(x)$, for some $\sigma > 1$.

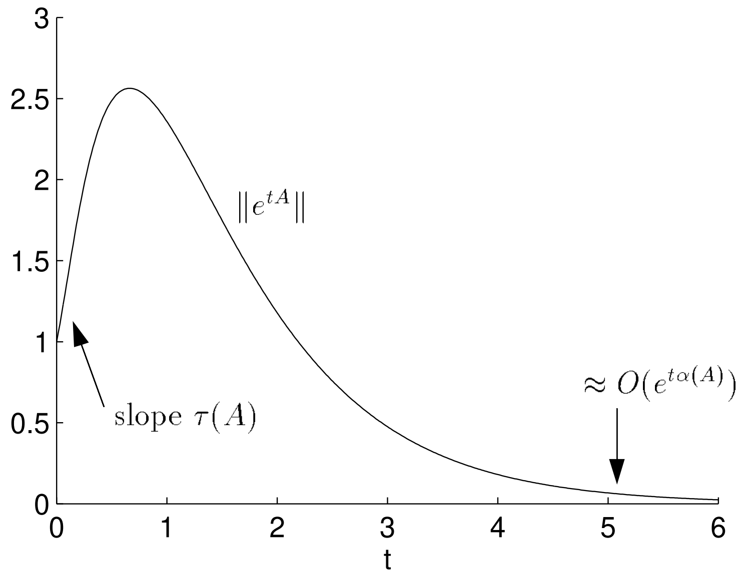

Figure 2.1: $\|e^{tA}\|$ for a typical non-normal matrix A. At $t = 0$ the behavior is determined by the numerical abscissa, $\tau(A)$, and as $t \to \infty$ it is determined by the spectral abscissa, $\alpha(A)$. If A were normal there would be no "hump" in the curve.

The linearized system governing the evolution of infinitesimal perturbations to the origin in (2.1) is

$$\frac{d}{dt}x = Ax. \tag{2.4}$$

For small enough initial conditions x_0, solutions to the full system (2.1) are well approximated by solutions to the linearized system:

$$x(t) = e^{tA}x_0.$$

If A is a non-normal matrix, the behavior of these solutions, $e^{tA}x_0$, may be very different at finite times than as $t \to \infty$. In particular, even if the spectrum of A is contained in the stable complex half-plane, solutions to the linearized problem may grow transiently by large factors. The potential for transient growth is reflected in the curve $\|e^{tA}\|$. For each t, there is an initial condition x_0, with $\|x_0\| = 1$, such that $\|e^{tA}x_0\| = \|e^{tA}\|$. Figure 2.1 shows a possible behavior of $\|e^{tA}\|$ for a non-normal matrix A with stable eigenvalues. For this example we have chosen

$$A = \begin{pmatrix} -1 & 10 \\ 0 & -2 \end{pmatrix}. \tag{2.5}$$

The behavior of solutions to the linearized problem for large times is determined by the spectrum of A. If the *spectral abscissa* of A is defined by

$$\alpha(A) = \max_{z \in \Lambda(A)} \operatorname{Re} z,$$

where $\Lambda(A)$ denotes the spectrum of A, then

$$\lim_{t \to \infty} \frac{\log \|e^{tA}\|}{t} = \alpha(A).$$

Thus, if $\alpha(A) < 0$, all solutions to the linearized problem asymptotically decay at a rate determined by the spectrum of A, and $x = 0$ is a stable fixed point of (2.1). In the sequel, we always assume $\alpha(A) < 0$. For the example depicted in Figure 2.1, $\alpha(A) = -1$.

Figure 2.1 shows that for a non-normal matrix A there can be solutions that grow quickly for small times. In fact, at $t = 0$, there are solutions that grow at a rate determined by the *numerical abscissa* of A

$$\tau(A) \equiv \sup_{x \in \mathbb{C}^n} \operatorname{Re} \frac{x^* A x}{x^* x} = \alpha\left(\frac{A + A^*}{2}\right) = \frac{d}{dt}\|e^{tA}\|\bigg|_{t=0}.$$

For non-normal A, we may have $\tau(A) \gg \alpha(A)$. For the example in Figure 2.1, $\tau(A) \approx 7.05$.

2.2 Bounds based on $\|e^{tA}\|$

As above, we assume $\alpha(A) < 0$. If A is normal, then it is not hard to show that

$$\|e^{tA}\| = e^{t\alpha(A)}.$$

However, if A is non-normal, then $\|e^{tA}\|$ may grow transiently before decaying as $t \to \infty$. In that case, for each λ in the range $0 \leq \lambda < -\alpha(A)$ there is a smallest constant $\gamma(\lambda)$ with $1 \leq \sup_{t\geq 0} \|e^{tA}\| \leq \gamma(\lambda) < \infty$, such that

$$\|e^{tA}\| \leq \gamma(\lambda)e^{-\lambda t}. \tag{2.6}$$

We do not define $\gamma(-\alpha(A))$, for in the case where the leading eigenvalues of A are defective we would have $\gamma(-\alpha(A)) = \infty$.

Here is a heuristic argument describing the behavior of some solutions to the full system (2.1). The approximate time scale on which solutions to the linearized problem decay is determined by λ, and $\gamma(\lambda)$ is a crude bound on the size of possible transient growth of solutions. An initial condition of size η may be amplified to size, at most, $\eta\gamma(\lambda)$ by linear transient growth caused by non-normality. The quadratic terms act on the amplified initial condition over a time period of order $1/\lambda$, producing an output of size approximately $C\eta^2\gamma(\lambda)^2/\lambda$. If this output is smaller than the initial input, that is, if $\eta > C\eta^2\gamma(\lambda)^2/\lambda$, then the process cannot repeat itself and growth is not sustained. This yields a lower bound on the size of the initial condition $\eta < \lambda/(C\gamma(\lambda)^2)$ below which all solutions decay.

The following theorem makes this idea precise. We use the notation

$$B_{\|\cdot\|}(y, \eta) = \{x \in \mathbb{C}^n : \|x - y\| < \eta\}$$

to denote the open ball about y of radius η in the indicated norm.

Theorem 2.2.1 *Let $\gamma(\lambda)$ be as in (2.6) for $0 \leq \lambda < -\alpha(A)$. Let $C > 0$ be as in (2.3). The basin of attraction of the origin in (2.1) contains the open ball $B_{\|\cdot\|}(0, \eta)$, where*

$$\eta = \frac{\lambda}{C\gamma(\lambda)^2}.$$

Proof: Let η be as above and let $\delta = \frac{\lambda}{C\gamma(\lambda)}$. Let $x(0) = x_0$ be any initial condition in $B_{\|\cdot\|}(0, \eta)$. Since $\|x(0)\| < \eta < \delta$ it follows that $\|x(s)\| < \delta$ for sufficiently small $s > 0$. Suppose, for contradiction, that for some $t > 0$ we have $\|x(s)\| < \delta$ for $0 \leq s < t$, and $\|x(t)\| = \delta$. By Duhamel's principle, we have

$$x(t) = e^{tA}x(0) + \int_0^t e^{(t-s)A} q(x(s)) ds. \tag{2.7}$$

Since $\|x(s)\| < \delta = \frac{\lambda}{C\gamma(\lambda)}$ we have by (2.3)

$$\|q(x(s))\| \leq C\|x(s)\|^2 < C\delta\|x(s)\| = \frac{\lambda}{\gamma(\lambda)}\|x(s)\|.$$

Thus there exists a number $\sigma,\ 0 < \sigma < \lambda$ such that

$$\|q(x(s))\| \leq \frac{\sigma}{\gamma(\lambda)}\|x(s)\|. \tag{2.8}$$

Now combining (2.7) and (2.8) yields

$$\|x(t)\| \leq \gamma(\lambda)e^{-\lambda t}\|x(0)\| + \gamma(\lambda)e^{-\lambda t}\frac{\sigma}{\gamma(\lambda)}\int_0^t e^{\lambda s}\|x(s)\| ds. \tag{2.9}$$

Let $u(t) = e^{\lambda t}x(t)$, so that (2.9) becomes

$$\|u(t)\| \leq \gamma(\lambda)\|u(0)\| + \sigma\int_0^t \|u(s)\| ds.$$

Applying Gronwall's inequality gives

$$\|u(t)\| \leq \gamma(\lambda)\|u(0)\|e^{\sigma t},$$

or, in terms of x,

$$\|x(t)\| \leq \gamma(\lambda)\|x(0)\|e^{-(\lambda-\sigma)t} < \gamma(\lambda)\eta e^{-(\lambda-\sigma)t} = \delta e^{-(\lambda-\sigma)t}. \tag{2.10}$$

This shows that $\|x(t)\| < \delta$, contradicting our assumption that $\|x(t)\| = \delta$ for some $t > 0$. Thus, we must have $\|x(s)\| < \delta$ for $s \geq 0$. It follows that σ in (2.8) may be chosen independent of t. So equation (2.10) holds for $t \geq 0$, showing that if $x(0) = x_0 \in B_{\|\cdot\|}(0, \eta)$, then $\|x(t)\| \to 0$ as $t \to \infty$ and x_0 is in the basin of attraction of the origin. □

In addition to demonstrating the potential for an increase in the non-normality of A to decrease the size of the basin of attraction, Theorem 2.2.1 shows the well-known fact that linear stability of a fixed point implies local nonlinear stability. The theorem is based on a standard proof of nonlinear stability, except that we have taken care to quantify the role of non-normality.

Theorem 2.2.1 contains a free parameter λ. We can optimize over λ to achieve the best possible bound attainable by the above method.

Corollary 2.2.1 *Let $\gamma(\lambda)$ be as in* (2.6) *for $0 \leq \lambda < -\alpha(A)$. Let $C > 0$ be as in* (2.3). *The basin of attraction of the origin in* (2.1) *contains the open ball $B_{\|\cdot\|}(0, \eta)$, where*

$$\eta = \sup_{0 \leq \lambda < -\alpha(A)} \frac{\lambda}{C\gamma(\lambda)^2}.$$

Proof: The supremum is attained since $\gamma(\lambda) \geq \sup_{t\geq 0} \|e^{tA}\|$. Furthermore, $\eta > 0$, since $0 \leq \lambda < -\alpha(A)$ implies $\gamma(\lambda) < \infty$. □

If A happens to be diagonalizable, that is, there exists a nonsingular matrix V and diagonal matrix D such that $V^{-1}AV = D$, then it is possible to give an upper bound on the constant $\gamma(\lambda)$ in (2.6). The columns of V are eigenvectors of A and the diagonal entries of D are the corresponding eigenvalues. Define the *condition number* of the eigenvector basis as

$$\kappa(V) = \|V\|\|V^{-1}\|.$$

It follows from

$$\|e^{tA}\| = \|e^{tVDV^{-1}}\| = \|Ve^{tD}V^{-1}\| \leq \kappa(V)\|e^{tD}\| = \kappa(V)e^{t\alpha(A)}$$

that $\gamma(\lambda) \leq \kappa(V)$. In general, however, $\gamma(\lambda)$ may be much smaller than $\kappa(V)$. For instance, for the example A in (2.5), we have a bound of the form (2.6)

$$\|e^{tA}\| \lessapprox 10.05e^{-t},$$

but the condition number of the eigenvector basis is $\kappa(V) \approx 20.05$.

Corollary 2.2.2 *Let $C > 0$ be as in* (2.3). *If there exists a matrix V such that $V^{-1}AV$ is diagonal, then the basin of attraction of the origin in* (2.1) *contains the open ball $B_{\|\cdot\|}(0, \eta)$, where*

$$\eta = \frac{-\alpha(A)}{C\kappa(V)^2}.$$

If A is normal, then there exists a unitary matrix V such that $V^{-1}AV$ is diagonal. For such a choice of V, $\kappa(V) = 1$, and the next corollary follows from the previous one.

Corollary 2.2.3 *Let $C > 0$ be as in* (2.3). *If A is normal, then the basin of attraction of the origin in* (2.1) *contains the open ball $B_{\|\cdot\|}(0, \eta)$, where*

$$\eta = \frac{-\alpha(A)}{C}.$$

This corollary shows that for normal matrices A, a lower bound on the size of the basin of attraction can be obtained by simply balancing the decaying effect of the spectrum against nonlinear growth. For non-normal matrices, the quantity $\gamma(\lambda)$ increases with the degree of non-normality, leading to a decrease in the size of the basin of attraction.

2.3 Bounds based on eigenvectors

In the last section we showed that the basin of attraction of the origin for the system (2.1) contains certain balls in the Euclidean norm. These balls are spherical and do not reflect the fact that the basin of attraction tends to be narrow in directions that experience the most transient growth and broad in directions that do not experience transient growth. In this section we introduce a different norm, based on the eigenvectors of A, in which the open balls are elliptical and do a better job of capturing the shape of the basin of attraction.

Suppose that A is a diagonalizable matrix, that is, there exists an invertible matrix V such that $V^{-1}AV$ is diagonal. The columns of V are the eigenvectors of A. We can use the matrix V to define a new norm

$$\|x\|_V = \|V^{-1}x\|, \; x \in \mathbb{C}^n,$$

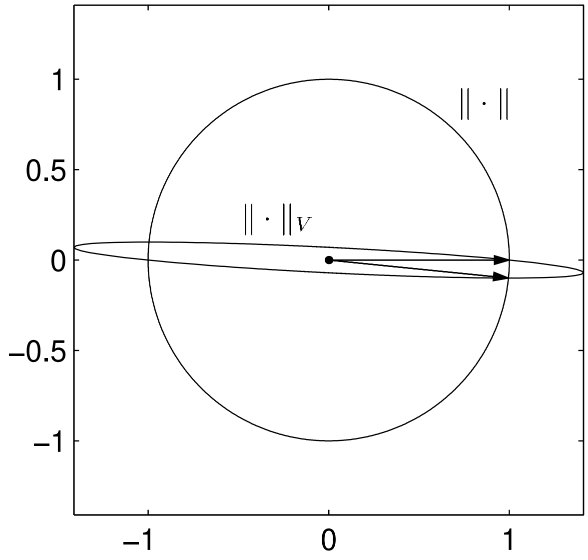

Figure 2.2: Comparison of the unit balls in the Euclidean norm, $\|\cdot\|$, and the eigenvector norm $\|\cdot\|_V$, for the example matrix A in (2.5). The columns of V are the eigenvectors of A (normalized to have Euclidean norm 1). The arrows point in the directions of the eigenvectors. The unit ball in the V-norm is narrowest in directions which experience the most transient linear growth.

where $\|\cdot\|$ is the Euclidean norm on $\mathbb{C}^n$. Figure 2.2 shows the unit balls in the Euclidean norm and the V-norm for the example matrix (2.5). The normalized eigenvectors are marked by arrows in the plot. An initial condition that lies approximately in the space spanned by an eigenvector will simply decay along that eigenspace. However, an initial condition that lies approximately orthogonal to the eigenvectors may grow transiently before ultimately decaying.

The eigenvectors of the example matrix A above are $v_1 = (1,0)^T$ and $v_2 = (10/\sqrt{101}, -1/\sqrt{101})^T \approx (0.9950, -0.0995)^T$. The initial condition $x_0 = (0,1)^T$

evolves linearly under the action of e^{tA} as

$$e^{tA}x_0 = 10e^{-t}v_1 + \sqrt{101}e^{-2t}v_2. \tag{2.11}$$

The eigenvectors are nearly parallel, so the expansion coefficients in the eigenvector basis are large since x_0 is approximately orthogonal to the eigenvectors. At $t = 0$ the terms in (2.11) approximately cancel, so the solution is of size 1, but for intermediate times the coefficient of v_2 decays faster than that of v_1 so that the cancellation property no longer holds and the solution can grow to a maximum amplitude of approximately 2.5. The eigenvector norm $\|\cdot\|_V$ captures this behavior. It tends to be broad in the directions spanned by the eigenvectors, which are not susceptible to transient growth, and narrow in the directions approximately orthogonal to the eigenvectors, which can grow transiently.

The following theorem gives a lower bound in this eigenvector norm on the size of the basin of attraction for (2.1).

Theorem 2.3.1 *Assume the matrix A in (2.1) is diagonalizable, with $V^{-1}AV = D = diag(\lambda_1, ..., \lambda_n)$ for some nonsingular matrix V. Then the basin of attraction of the origin in* (2.1) *contains the open ball $B_{\|\cdot\|_V}(0, \eta)$, where*

$$\eta = \frac{-\alpha(A)}{\sup_{\|x\|_V=1} \|q(x)\|_V}$$

Proof: Introduce new coordinates to diagonalize the linear part of (2.1), that is, let $y = V^{-1}x$. In the new y-coordinates, which are the coefficients of x in the eigenvector basis, (2.1) becomes

$$\frac{d}{dt}y = Dy + V^{-1}q(Vy). \tag{2.12}$$

Since $\alpha(D) = \alpha(A) < 0$, the origin of system (2.12) is a stable fixed point. Let

$$\begin{aligned} C &= \sup_{y \in \mathbb{C}^n} \frac{\|V^{-1} q(Vy)\|}{\|y\|^2} \\ &= \sup_{\|y\|=1} \|V^{-1} q(Vy)\| \\ &= \sup_{\|V^{-1}x\|=1} \|V^{-1} q(x)\| \\ &= \sup_{\|x\|_V=1} \|q(x)\|_V, \end{aligned} \tag{2.13}$$

where the second equivalence follows from (2.2). It follows that the nonlinear term in (2.12) satisfies the bound (2.3) for this choice of C. Now, since D is normal, Corollary 2.2.3 applies to the system (2.12) to show that the basin of attraction of the origin contains the ball (in the y-coordinate space) $B_{\|\cdot\|}(0, \eta)$, with

$$\eta = \frac{-\alpha(D)}{C} = \frac{-\alpha(A)}{\sup_{\|x\|_V=1} \|q(x)\|_V}. \tag{2.14}$$

The theorem follows by transforming the ball back to the original x-coordinates. □

The proof of Theorem 2.3.1 shows that it follows easily from Theorem 2.2.1 by using the eigenvector basis to introduce a change of coordinates in system (2.1) such that the linear part is diagonalized, applying Theorem 2.2.1 in the new coordinates, and transforming the result back to the original coordinates. The advantage to using the eigenvector norm is that is tends to reveal more than simply the size of the basin of attraction of the origin in (2.1); it also reveals the shape.

2.4 A model problem

To illustrate the use of the techniques developed in Sections 2.2–2.3 we apply them to the model problem (1.2) from [95]:

$$\dot{\mathbf{u}} = A\mathbf{u} + \|\mathbf{u}\| B\mathbf{u},$$

with

$$\mathbf{u} = \begin{pmatrix} u \\ v \end{pmatrix}, \qquad A = \begin{pmatrix} -R^{-1} & 1 \\ 0 & -2R^{-1} \end{pmatrix}, \qquad B = \begin{pmatrix} 0 & -1 \\ 1 & 0 \end{pmatrix} \tag{2.15}$$

to derive lower bounds on the size of the basin of attraction of the origin. We considered this system in Chapter 1 as an example of how non-normality and nonlinearity can combine to dramatically reduce the size of the basin of attraction of a linearly stable fixed point — in this case the origin, corresponding to the laminar solution in a linearly stable shear flow. In this thesis, we are interested in the dependence of the size of that basin of attraction on the parameter R, analogous to the Reynolds number (see equation (1.1)). Thus the following lower bounds are stated in terms of R.

First we apply the techniques based on $\|e^{tA}\|$ from Section 2.2 to (2.15). The nonlinear term satisfies the bound

$$\big\| \|\mathbf{u}\| B\mathbf{u} \big\| \leq \|\mathbf{u}\|^2,$$

so the constant C in (2.3) may be chosen as $C = 1$. Figure 1.2 indicates that $\|e^{tA}\|$ grows as large as $O(R)$ over a time period $O(R)$. In fact, it can be shown that $\|e^{tA}\|$

approximately satisfies the bound

$$\|e^{tA}\| \lessapprox Re^{-t/R} \tag{2.16}$$

(in the sense that $\sup_t \|e^{tA}\| e^{t/R} \sim R$ as $R \to \infty$). It follows from Theorem 2.2.1 that the basin of attraction of the origin in (2.15) contains the open ball $B_{\|\cdot\|}(0, \eta)$, where $\eta \approx R^{-3}$.

However, the bound (2.16) is not optimal in the sense that it does not yield the largest η possible from Theorem 2.2.1. It is possible to optimize over λ, as in Corollary 2.2.1, to achieve a better bound. We have numerically determined the optimal value $\lambda_{\text{opt}} \approx 0.4696R^{-1}$ (for sufficiently large R), with the corresponding value $\gamma(\lambda_{\text{opt}}) \approx 0.3725R$. Thus, by Corollary 2.2.1, the basin of attraction of the origin in (2.15) contains the open ball $B_{\|\cdot\|}(0, \eta)$, where η is given approximately by

$$\eta = \sup_{0 \le \lambda < -\alpha(A)} \frac{\lambda}{C\gamma(\lambda)^2} \approx \frac{0.4694R^{-1}}{(0.3725R)^2} = 3.3821R^{-3}.$$

The technique based on $\|e^{tA}\|$ incorporates non-normality to reveal the correct $O(R^{-3})$ scaling of the basin of attraction of the origin (see Section 1.2). The bound is not sharp; the basin of attraction of the origin actually contains the open ball $B_{\|\cdot\|}(0, \eta)$ with $\eta \approx 6.59R^{-3}$. Thus the optimal estimate from Corollary 2.2.1 is off by approximately a factor of 2.

These estimates are excellent given that no analysis of the particular dynamics of the system (2.15) was necessary. However, they only tell us that the basin of attraction contains a spherical ball of size $O(R^{-3})$. This does not reflect the fact that the basin of attraction is narrower in directions which experience transient growth and broader in directions which do not (such as in the directions of the eigenvectors of A); see Figure 1.7 in Chapter 1. Fortunately, the eigenvector norm $\|\cdot\|_V$, introduced in Section 2.3, tends to capture the shape, or at least the characteristic dimensions, of the basin of attraction.

The matrix V, whose columns are the normalized eigenvectors of A, is

$$V = \begin{pmatrix} 1 & R/\sqrt{R^2+1} \\ 0 & -1/\sqrt{R^2+1} \end{pmatrix},$$

with inverse

$$V^{-1} = \begin{pmatrix} 1 & R \\ 0 & -\sqrt{R^2+1} \end{pmatrix}.$$

Unit balls in this norm satisfy the inequality

$$u^2 + 2uvR + (2R^2+1)v^2 < 1$$

which defines an ellipse whose major and minor axes nearly coincide with the u and v axes, respectively, and whose lengths are approximately $2\sqrt{2}$ and $\sqrt{2}R^{-1}$, respectively. Thus, the unit ball in the V-norm is narrowest in approximately the direction of the v coordinate, which is the direction most susceptible to transient growth.

To apply Theorem 2.3.1 we need to estimate the quantity $\sup_{\|x\|_V=1}\|q(x)\|_V$, where $q(x)$ is the quadratic nonlinearity in (2.15) and $x = (u,v)^T$. It can be shown that $\sup_{\|x\|_V=1}\|q(x)\|_V \sim 2\sqrt{2}R$ as $R \to \infty$. So by Theorem 2.3.1, with $\alpha(A) = -R^{-1}$, the basin of attraction of the origin contains the open ball $B_{\|\cdot\|_V}(0,\eta)$, where η is given by

$$\eta = \frac{-\alpha(A)}{\sup_{\|x\|_V=1}\|q(x)\|_V} \approx \frac{-R^{-1}}{2\sqrt{2}R} = \frac{\sqrt{2}}{4}R^{-2} \approx 0.3536R^{-2}.$$

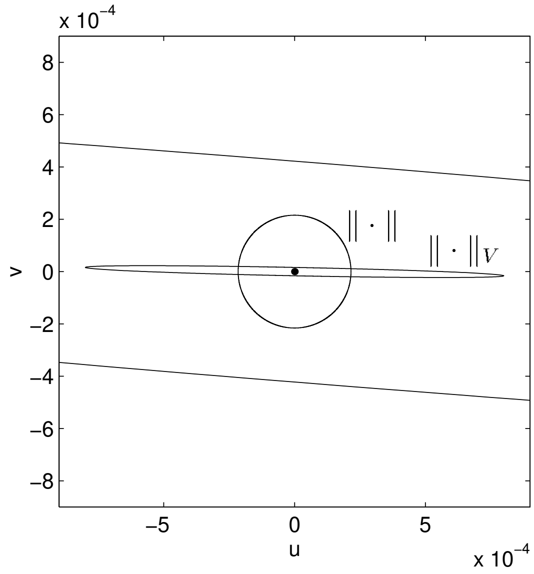

Figure 2.3: Comparison of the lower bounds in the Euclidean norm and the V-norm for the model problem (1.2) with $R = 25$. Shown are the balls $B_{\|\cdot\|}(0, 3.3821R^{-3})$ and $B_{\|\cdot\|_V}(0, 0.3536R^{-2})$ as determined in the text. Also shown is the boundary of the basin of attraction, formed by the stable manifolds of the saddle points near the origin (see Figures 1.6–1.7). The ball in the V-norm captures the characteristic dimensions of the basin of attraction.

The unit balls in the V-norm scale are ellipses which scale as $O(R^{-1})$ in the v direction and $O(1)$ in the u direction. So Theorem 2.3.1 shows that the basin of attraction of the origin of (1.2) contains an ellipse which scales as $O(R^{-3})$ in the v direction and $O(R^{-2})$ in the u direction. Thus, bounds in the V-norm achieved by the above technique tend to capture not only the size of the basin of attraction, but also the shape. Again, this bound is not sharp. The basin of attraction actually contains the ball $B_{\|\cdot\|_V}(0, \eta)$, where $\eta \approx 2.13R^{-2}$. So the bound achieved by the V-norm technique is off by about a factor of 6 for this example.

In Figure 2.3 we show the regions which must be in the basin of attraction of the origin as determined by the above lower bounds. The region bounded by the ball in the Euclidean norm appears larger, but the region bounded by the ball in the V-norm scales as R^{-3} in the vertical direction and R^{-2} in the horizontal direction thus effectively capturing the characteristic dimensions of the basin of attraction for the model problem (2.15) (see Figure 1.7 on page 13).

2.5 Infinite dimensions

While we have concentrated on finite dimensional systems, these results can easily be applied to some infinite dimensional systems. For example, Theorem 2.2.1 can be applied to any system (2.1), for which bounds (2.3) and (2.6) are available.

Similarly, Theorem 2.3.1 can be extended to infinite dimensional systems provided the nonlinear terms can be bounded as above and also provided that the linear operator A has a Riesz basis — a complete basis of eigenfunctions for which the operator corresponding to V is bounded and has a bounded inverse; see [28] for instance.

There are, of course, infinite dimensional systems to which the above results do not apply. For instance, we would like to apply Theorem 2.2.1 to the Navier–Stokes equations which govern the evolution of disturbances to the linearly stable laminar solution in plane Couette flow, but the quadratic nonlinear term in that case is $(\mathbf{u} \cdot \nabla)\mathbf{u}$, which contains spatial derivatives, making a bound of the form (2.3) impossible in the usual energy norm. It might be possible to surmount this difficulty through the use of a different norm like that used by G. Kreiss, *et al.* [55].

They showed that the basin of attraction of the laminar solution in plane Couette flow contains a ball which scales as $O(R^{-21/4})$ by using a technique based on the norm of the resolvent of the linear term and a Sobelev norm to bound the nonlinear terms.

Chapter 3

Low-dimensional models of subcritical transition to turbulence*

In Section 1.2 we saw one example of a low-dimensional model of subcritical transition to turbulence in linearly stable shear flows. We also saw how that model related to the concept of threshold exponents (see equation (1.1) on page 6). In this chapter, we examine several low-dimensional systems of ordinary differential equations which have been proposed, by different groups, to model certain aspects of subcritical transition to turbulence in shear flows and even the turbulent state itself. While many of these models were designed for disparate purposes, their mathematical structure is strikingly similar.

*This chapter is adapted from the paper of the same title written with L.N. Trefethen, to appear in *Physics of Fluids* [3].

Three of the models we consider were proposed by our group here at Cornell:

$$\begin{aligned} \text{TTRD} &= \text{Trefethen, Trefethen, Reddy and Driscoll, 1993 [95],} \\ \text{BDT} &= \text{Baggett, Driscoll and Trefethen, 1995 [2],} \\ \text{BT} &= \text{Baggett and Trefethen, unpublished, 1995.} \end{aligned}$$

Two more models are due to Waleffe at MIT. These models are outgrowths of earlier work with Hamilton and Kim at the Center for Turbulence Research at NASA Ames Research Center and Stanford University [37, 99]:

$$\begin{aligned} \text{W} &= \text{Waleffe, 1995 [97, 98],} \\ \text{W2} &= \text{Waleffe, unpublished, 1995.} \end{aligned}$$

A sixth comes from the University of Marburg in Germany, building upon earlier work in Marburg by Boberg and Brosa [7]:

$$\text{GG} = \text{Gebhardt and Grossmann, 1994 [27].}$$

A seventh was presented in a paper from the Royal Institute of Technology in Stockholm,

$$\text{KLH} = \text{G. Kreiss, Lundbladh and Henningson, 1994 [55].}$$

Finally, an eighth model was proposed in a manuscript from Göteborg, Sweden,

$$\text{JRB} = \text{Johnson, Rannacher and Boman, 1995 [46].}$$

For each model, the origin, corresponding to the laminar solution, is linearly stable, so that sufficiently small initial conditions asymptotically decay. The least stable modes decay exponentially with decay rate $O(R^{-1})$, where R is a parameter analogous to the Reynolds number, in analogy with linearly stable shear flows such as plane Couette and pipe Poiseuille flow. But, as with the linearized Navier–Stokes[1] equations governing the evolution of small perturbations to the laminar solution in the same flows, the linear part (at the origin) of each of these models amplifies certain structures by as much as $O(R)$ over a time period $O(R)$. In contrast to a normal linear amplification process, in the non-normal case the input and output structures are different (in plane shear flows, for example, they may be streamwise vortices and streaks, respectively), and the linear process alone cannot sustain the growth of the perturbation. The role of nonlinearities, then, is to recycle some of the outputs back into inputs, creating a feedback loop and allowing the solution to "bootstrap" to a sustained higher amplitude; see Figure 3.1.

Remarkably, the amplification caused by the interaction of non-normality and nonlinearity, that is, bootstrapping, can be much greater than that caused by the non-normal linear part alone. As shown in Chapter 2, this interaction may result in a basin of attraction of the origin which shrinks much faster than $O(R^{-1})$ as $R \to \infty$. The purpose of this chapter, in addition to demonstrating the similarity of this collection of models, which were proposed for widely varying reasons, is to present the rather surprising fact that six of these eight models have threshold exponent α less than -1. That is, the amplitude $\epsilon_{\min}$ of the smallest perturbation which causes transition to "turbulence" (for our purposes this means that the solution does not

[1]with the appropriate nondimensionalization; see [33] for instance.

asymptotically decay) scales approximately as

$$\epsilon_{\min} = O(R^{\alpha}) \tag{3.1}$$

for some $\alpha < -1$ as $R \to \infty$. Thus these models lend further support to the conjecture of Trefethen, et al., that (3.1) holds with $\alpha < -1$, where $\epsilon_{\min}$ measures the energy norm of the smallest perturbation to the laminar flow which may excite transition to turbulence in linearly stable shear flows such as plane Couette flow and pipe Poiseuille flow [95].

While the linear terms in the models are similar, the nonlinear terms come in two varieties — with or without "selection rules." In plane Couette flow, for example, the strongest transient amplification is achieved by a shear tilting mechanism acting on structures independent of the streamwise coordinate (see Chapter 4). If the initial condition is perfectly independent of the streamwise coordinate, with zero energy in the Fourier components corresponding to the streamwise variation, then this situation must persist for all time, and turbulence cannot be achieved. Algebraically, this can be seen by noting that the nonlinear interactions of the Navier–Stokes equations operate in triads, obeying selection rules of the form

$$(\alpha_1, \beta_1) + (\alpha_2, \beta_2) \to (\alpha_1 + \alpha_2, \beta_1 + \beta_2),$$

where α and β denote Fourier parameters in the streamwise and spanwise directions, respectively. In particular, a single mode (α, β) does not affect itself nonlinearly.

A useful description of selection rules comes from Gebhardt and Grossmann [27], who write: "In highly symmetric geometries, where the eigenmodes are, e.g., plane waves, the eigenspaces can be classified by the conserved components of their wave vectors. Eigenspaces with different wave vectors are orthogonal of course. Thus the non-normality of the linearized Navier-Stokes dynamics can act only *within* each subspace. Since the Navier–Stokes nonlinearity $(\mathbf{u} \cdot \nabla)\mathbf{u}$ does not couple directly, eigenmodes within the same subspace due to momentum conservation, non-normality and second-order nonlinear interaction do not combine."

In Section 3.1 we consider models that do not incorporate selection rules into the nonlinear terms. In Section 3.2, we consider the models which incorporate selection rules. We discuss two different heuristic arguments which explain how bootstrapping works in these models in Section 3.3. Finally in Section 3.4 we summarize our results.

3.1 Models without selection rules

The first three models we consider are similar in that they have no selection rules. All three of these models feature non-modal linear amplification combined with nonlinear, energy conserving mixing. These three models and the first model of Section 3.2, the BT model, reflect the view of their authors that the transition process is "essentially linear" in the sense that its qualitative features are not sensitive to the details of the nonlinear interactions. Trefethen, *et al.* [95], and Boberg and Brosa before them [7], proposed that the role of nonlinearity in transition is to serve as a mixing mechanism, enabling outputs from the linear, non-modal amplification process to be recycled back to inputs, as suggested in Figure 3.1. According to this view, even if the Navier–Stokes equations happened to have quite different

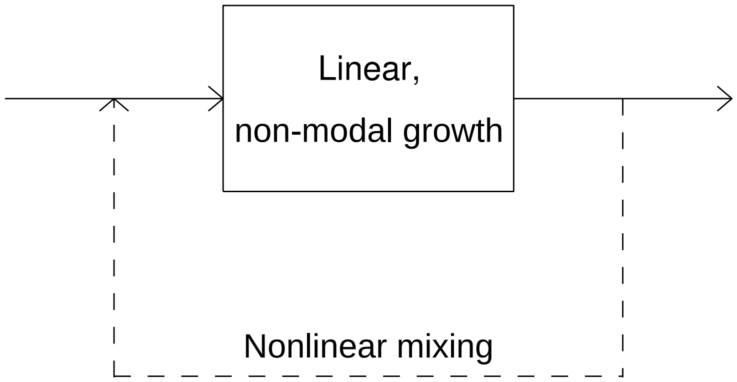

Figure 3.1: Schematic view of the transition process viewed as non-modal linear amplification combined with nonlinear mixing (figure taken from [2]).

nonlinear terms than the actual ones, there would probably still be a recognizable phenomenon of subcritical transition to turbulence.

3.1.1 The TTRD model

The TTRD model was proposed to illustrate how non-modal linear amplification can interact with nonlinear mixing to produce a threshold exponent $\alpha < -1$. We have already met this model in Chapters 1–2; however, it is presented here in a slightly different way.

Each of the models in this chapter can be written as a sum of linear and quadratic terms (the GG model includes a third term which we describe below) in the form

$$\dot{\mathbf{u}} = A\mathbf{u} + B(\mathbf{u}, \mathbf{u}), \tag{$*$}$$

where $\mathbf{u}$ is a real or complex n-dimensional vector, A is an $n \times n$ matrix, and $B(\mathbf{u}, \mathbf{u})$ is a vector of quadratic nonlinear terms. In every case, the matrix A is non-normal, and solutions to the linearized problem $\dot{\mathbf{u}} = A\mathbf{u}$ may be amplified by a factor $O(R)$ over a time period $O(R)$.

Written in our standard form $(*)$ the TTRD model has terms

$$\mathbf{u} = \begin{pmatrix} u \\ v \end{pmatrix} \in \mathbb{R}^2, \qquad A = \begin{pmatrix} -R^{-1} & 1 \\ & -2R^{-1} \end{pmatrix}, \qquad B(\mathbf{u},\mathbf{u}) = \|\mathbf{u}\| \begin{pmatrix} & -1 \\ 1 & \end{pmatrix} \mathbf{u}. \tag{TTRD}$$

The linear term A represents a linear, non-modal transient amplifying process of amplitude $O(R)$ over a time scale $O(R)$. The term $B(\mathbf{u},\mathbf{u})$ mixes the two variables but does not directly affect the energy, since the matrix involved is skew-symmetric. The variables are allowed to affect themselves nonlinearly. Thus, (TTRD) does not incorporate selection rules.

Figure 3.2 gives an indication of the behavior of (TTRD) for $R = 100$. In this chapter we shall present a number of figures of this kind, always following the same format. Eleven curves are shown, corresponding to $\|\mathbf{u}(t)\|$ as a function of t for eleven different initial conditions $\mathbf{u}(0)$. The initial conditions have norms $\|\mathbf{u}(0)\| = 10^{-7}, 10^{-6.5}, 10^{-6}, ..., 10^{-2}$. In Figure 3.2, as in our other analogous figures, the lower curves have approximately the same shape, differing only in vertical displacement. This is because in these cases, the amplitudes are sufficiently small that the nonlinear terms have negligible effect. What remains is just the linear, non-modal behavior: amplification by about 1.5 orders of magnitude followed by slow decay to the origin analogous to the laminar flow. The upper curves, however, are strongly affected by nonlinearity. At the beginning, they follow the shape of the linear evolution, but in the cases with $\|\mathbf{u}(0)\| > 10^{-5.5}$, they are attracted as $t \to \infty$ to a state of magnitude

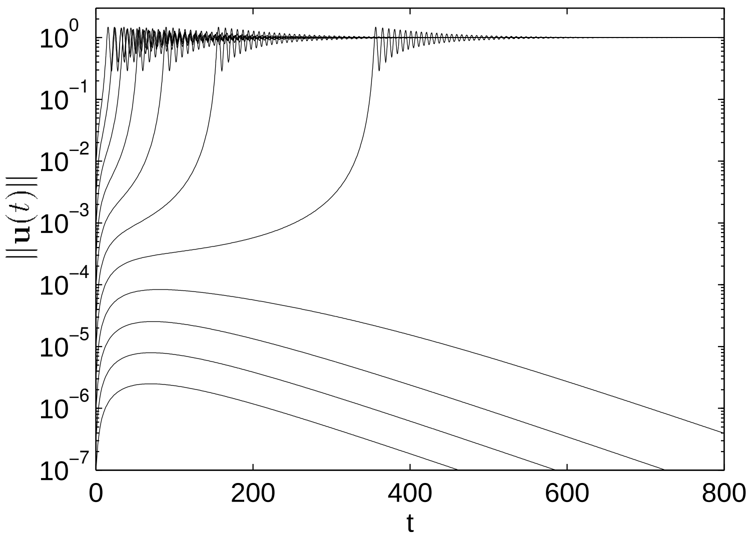

Figure 3.2: Evolution curves for the model (TTRD) (threshold exponent $\alpha = -3$) with $R = 100$. The curves show the vector norm $\|\mathbf{u}(t)\|$ for optimal initial conditions of amplitudes $\|\mathbf{u}(0)\| = 10^{-7}, 10^{-6.5}, 10^{-6}, \ldots, 10^{-2}$.

$O(1)$, analogous to turbulent flow.

What is important in Figure 3.2 is that although the linear amplification is by less than two orders of magnitude and the nonlinear terms conserve energy, the total amplification in the nonlinear system is by close to six orders of magnitude. This is what we referred to above as bootstrapping. Specifically, for the model (TTRD) with $R = 100$, the threshold amplitude for transition is approximately 7.63×10^{-6}, and this threshold decreases with exponent $\alpha = -3$ as $R \to \infty$. We shall not present the evidence for this and other statements about threshold exponents in this chapter, though Theorem 2.2.1 from Chapter 2 may be applied to all of the models in this chapter to give a lower bound on the threshold exponent of $\alpha = -3$ in every case. We assure the reader that in every case, numerical experiments show that the R^α dependence is clean and unambiguous. In fact, it can be shown, by a careful rescaling of the variables in each model, that the R^α dependence is asymptotically exact as $R \to \infty$.

We have described the amplitude of the initial vector $\mathbf{u}(0)$ but not its direction. For Figure 3.2 and the other analogous plots of this chapter, $\mathbf{u}(0)$ is always determined by the following recipe:

$$\mathbf{u}(0) = C(\mathbf{u}_{\mathrm{opt}} + 0.1\mathbf{u}_{\mathrm{rand}}). \tag{3.2}$$

Here, $\mathbf{u}_{\mathrm{opt}}$ denotes the unit vector such that $e^{tA}\mathbf{u}_{\mathrm{opt}}$ achieves the most transient growth (obtained via the singular value decomposition of e^{tA}; see Section 1.2 for details). The vector $\mathbf{u}_{\mathrm{rand}}$ is a unit vector whose entries are sampled independently from the standard normal distribution, then rescaled such that $\|\mathbf{u}_{\mathrm{rand}}\| = 1$. Thus $\mathbf{u}(0)$ consists of a vector designed to achieve optimal linear growth plus a noise vector of relative size 10% (by amplitude) or 1% (by energy). Such noise is necessary in some of the low-dimensional models — as in the Navier–Stokes equations themselves — to break symmetries associated with structures independent of the streamwise or spanwise coordinate. The initial amplitude of the noise has little effect on the overall behavior.

Though we present only one figure for each model described in this chapter, several runs have in fact been made in each case, with distinct vectors $\mathbf{u}_{\mathrm{rand}}$, to ensure that the behavior in the plot presented is typical.

In summary: for the first model under consideration, (TTRD), a bootstrapping phenomenon occurs and the threshold exponent is $\alpha = -3$.

3.1.2 The BDT model

The view taken in (TTRD) is that more or less random nonlinearities should cause the system to bootstrap, but if the matrix in the nonlinear term is chosen at random, though still skew-symmetric, then transition is observed with probability only 0.5. The other half of the time, the nonlinear mixing rotates energy in the phase plane in the wrong direction, shutting off the loop of Figure 3.1. One might think that this shut-off effect calls into question the idea that arbitrary nonlinear mixing is likely to generate a phenomenon of subcritical transition. In fact, it is an artifact of the triviality of two-dimensional dynamics. To elucidate this point, a three-variable analogue of (TTRD) was proposed in [2]:

$$\begin{pmatrix} \dot{u} \\ \dot{v} \\ \dot{w} \end{pmatrix} = \begin{pmatrix} -2R^{-1} & \beta(R) & \\ & -2R^{-1} & \beta(R) \\ & & -2R^{-1} \end{pmatrix} \begin{pmatrix} u \\ v \\ w \end{pmatrix} + \left\| \begin{pmatrix} u \\ v \\ w \end{pmatrix} \right\| \begin{pmatrix} & a & b \\ -a & & c \\ -b & -c & \end{pmatrix} \begin{pmatrix} u \\ v \\ w \end{pmatrix}. \tag{3.3}$$

As in (TTRD), the linear term here produces transient, non-modal amplification of amplitude $O(R)$ and time scale $O(R)$; the value $\beta(R) = 3.86\sqrt{(R+1)/R^2}$ was chosen in [2] so that the "O" constants are approximately 1. The entries a, b, c were chosen randomly, but scaled so that the skew-symmetric matrix in the energy conserving nonlinear term has norm 1 ($a^2+b^2+c^2=1$). Note that the variables are allowed to affect themselves nonlinearly, so that (3.3) does not incorporate selection rules.

As expected, the arbitrary choices of nonlinear coefficients in (3.3) lead to a variety of different $O(1)$ "turbulent" states including finite fixed points, the point at infinity, limit cycles, or chaos. However, the early stages of transition are in-

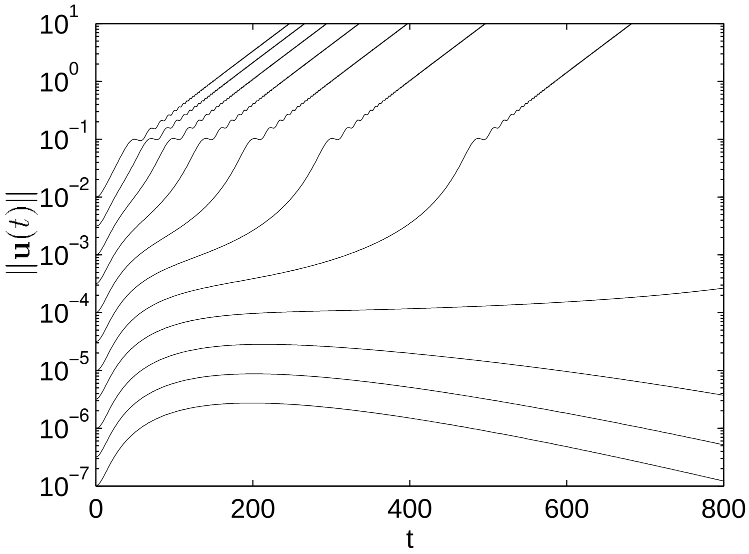

Figure 3.3: Evolution curves for model (BDT) (threshold exponent $\alpha = -3$) with $R = 100$.

dependent of the final state, and the random choice of nonlinear coefficients yields transition with probability close to 1, not 0.5, for sufficiently high R, with threshold exponent again $\alpha = -3$.

We consider a somewhat simplified version of (3.3). Written in our standard form $(*)$ it has terms

$$\mathbf{u} = \begin{pmatrix} u \\ v \\ w \end{pmatrix} \in \mathbb{R}^3, \qquad A = \begin{pmatrix} -R^{-1} & R^{1/2} & 0 \\ 0 & -R^{-1} & R^{1/2} \\ 0 & 0 & -R^{-1} \end{pmatrix}, \tag{BDT}$$

$$B(\mathbf{u}, \mathbf{u}) = \|\mathbf{u}\| \begin{pmatrix} 0 & -1 & -1 \\ 1 & 0 & -1 \\ 1 & 1 & 0 \end{pmatrix} \mathbf{u}.$$

This system captures the essence of (3.3), though of course, since the constants a, b, c have been set to -1, it exhibits only a single behavior as $t \to \infty$ for any

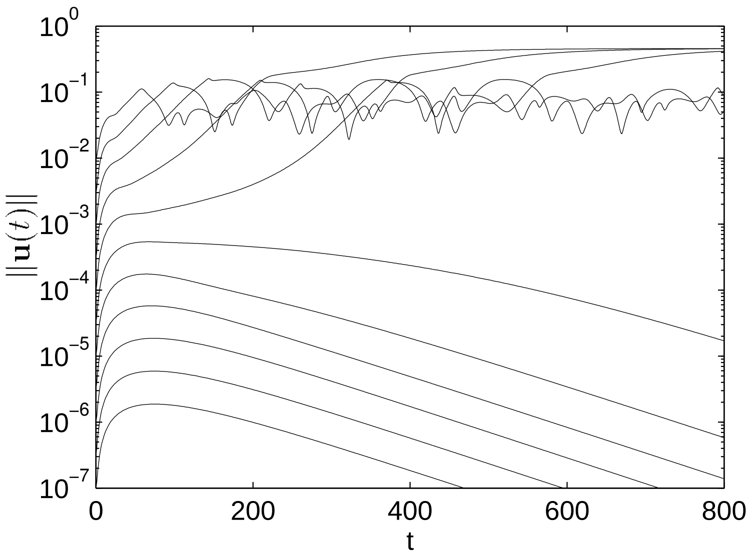

Figure 3.4: Evolution curves for model (GG) (threshold exponent $\alpha = -3$) with $R = 100$.

fixed choice of initial data. Figure 3.3 shows the evolution of (BDT) in the usual format. Again we have a bootstrapping phenomenon, and the threshold exponent is $\alpha = -3$.

3.1.3 The GG model

Now we cross the Atlantic to the fluid mechanics group of Siegfried Grossmann at the University of Marburg in Germany.

The papers [11, 33, 78, 95] were a closely related series of works appearing in 1991–1993 on the subject of linear, non-normal effects in hydrodynamic stability. When these papers were written, their authors were unaware of a remarkable publication by Boberg and Brosa, former students of Grossmann, in which they proposed many of the same ideas four years earlier [7]. In retrospect, it now appears that the schema of Figure 3.1 was first described in the Boberg–Brosa paper. The Marburg group, like the Cornell group, have taken the view that more or less arbitrary nonlinear mixing will be sufficient to induce transition in flows with non-normal linear amplification. Boberg and Brosa write bluntly, "The nonlinearity is a random mixer."

While some low-dimensional models are discussed in [7], for example of dimensions 10 and 20, no single model is settled upon and no Reynolds number dependence is included. More recently, however, motivated by the model (TTRD), Gebhardt and Grossmann have published a paper in which they propose a model containing two complex variables [27]. This work is close to that of [2]; the two were independent and approximately simultaneous. To facilitate comparisons, we have rescaled Gebhardt and Grossmann's variables t and u by factors R and R^{-1}, respectively, and then replaced R by $R/20$. Their equations now take a form similar to our standard form

$$\dot{\mathbf{u}} = A\mathbf{u} + B(\mathbf{u},\mathbf{u}) + C(\|\mathbf{u}\|)\mathbf{u},$$

with terms

$$\mathbf{u} = \begin{pmatrix} u_1 \\ u_2 \end{pmatrix} \in \mathbb{C}^2, \qquad A = \begin{pmatrix} -.9R^{-1} + .8i\gamma & .7 \\ 0 & -1.9R^{-1} + 1.1i\gamma \end{pmatrix}, \tag{GG}$$

$$\begin{aligned} B_1(\mathbf{u},\mathbf{u}) &= b_1u_1u_2 + ib_2u_1u_2^* + b_3u_1^*u_2 + ib_4u_1^*u_2^* - b_7^*u_2^2 - (b_5^* + ib_6)u_2u_2^* - ib_8u_2^{*2}, \\ B_2(\mathbf{u},\mathbf{u}) &= b_5u_1u_2 + ib_6u_1^*u_2 + b_7u_1u_2^* + ib_8u_1^*u_2^* - b_3^*u_1^2 - (b_1^* + ib_2)u_1u_1^* - ib_8u_1^{*2}, \end{aligned}$$

$$C(\|\mathbf{u}\|) = \frac{-\|\mathbf{u}\|}{2/R + \|\mathbf{u}\|} \begin{pmatrix} 0 & .7 \\ 0 & 0 \end{pmatrix}.$$

In these equations, the A term represents linear, non-modal amplification, the B term is quadratic and energy conserving for any choice of b_j (while this is not obvious as written, it is easy to verify that $\frac{1}{2}\frac{d}{dt}\|\mathbf{u}\|^2 = \mathrm{Re}\{\mathbf{u}^* A\mathbf{u} + \mathbf{u}C(\|\mathbf{u}\|)\mathbf{u}\}$, showing that the nonlinear terms do not contribute to changes in energy), the C term is a mean flow adjustment which reflects the fact that as the disturbance grows it extracts energy from the mean flow and reduces the potential for further perturbation growth, and γ is a zero or non-zero parameter used to model the effect of convection by the background shear flow. The variables u_1, u_2 represent the amplitude and phase of some flow pattern such as eigenmodes of a fluid flow in the absence of some background shear flow.

Because these equations contain complex rather than real variables, they look different from the others we are considering. However, as long as $\gamma = 0$, the linear part produces non-normal, transient growth of size $O(R)$ over a time period $O(R)$, in agreement with the other models. If $\gamma = 1$, corresponding to flow patterns which feel the effect of the background shear flow, such as modes with streamwise dependence in a plane channel flow, the non-normality saturates as $R \to \infty$ so that the non-modal amplification is $O(1)$. Thus we consider only $\gamma = 0$. In the actual Navier–Stokes equations the non-normality does not saturate as $R \to \infty$, but the non-modal amplification is less for structures which feel the effects of the background shear flow; see [95] for instance.

The nonlinearity $B(\mathbf{u}, \mathbf{u})$ in (GG) can be viewed as essentially random. In the paper [27] Gebhardt and Grossmann make the arbitrary choice $b_1 = 0.2$, $b_2 = 0.4i$, $b_3 = 0.6$, $b_4 = 0.8i$, $b_5 = 1.0$, $b_6 = 1.2i$, $b_7 = 1.4$, $b_8 = 1.6i$. Though there is no discussion of the exponent α in [27], there is some consideration of threshold amplitudes near their Figures 6 and 8. For a model of this kind with no selection rules one would expect the exponent to be $\alpha = -3$. This expectation is confirmed by experiments; see Figure 3.4.

Curiously, the lack of selection rules in the TTRD, BDT, and GG models roughly corresponds to the fact these models possess a non-physical property: they undergo "transition" even when the initial vector is uncontaminated by noise. In these models, an initial vector $\mathbf{u}(0)$ determined solely on the basis of linear algebra considerations is enough to excite transition. We have confirmed this by experiments (not shown) that reveal that if the noise component of (3.2) is removed, the curves of Figures 3.2–3.4 change very little.

3.2 Models with selection rules

The models in the previous section deliberately included essentially arbitrary quadratic nonlinearities, that is, they did not incorporate selection rules. In this section we consider models that incorporate selection rules. The first model in this section, the BT model, includes selection rules in the sense described above by Gebhardt and Grossmann — nonlinearity acts strictly between the subspaces in which nonnormality occurs, that is, the variables do not affect themselves nonlinearly. While the other models include variables which do affect themselves nonlinearly, they still include selection rules in the sense that the authors modeled selection rules through the choice of nonlinear terms which are intended to be suggestive of certain physical process without necessarily capturing them accurately.

3.2.1 The BT model

In unpublished work early in 1995, we modified the TTRD and BDT models to incorporate not only selection rules, but also products of variables instead of non-physical products of norms. To accomplish this, while maintaining essentially arbitrary nonlinear mixing, we replaced the single pair of variables of (TTRD) by three pairs of variables. The resulting six-variable model can be written in our standard form $(*)$ with terms

$$\mathbf{u} = \begin{pmatrix} u_1 \\ u_2 \\ u_3 \\ u_4 \\ u_5 \\ u_6 \end{pmatrix} \in \mathbb{R}^6, \qquad A = \begin{pmatrix} -R^{-1} & 1 & & & & \\ & -R^{-1} & & & & \\ & & -R^{-1} & & & \\ & & & -R^{-1} & & \\ & & & & -R^{-1} & \\ & & & & & -R^{-1} \end{pmatrix},$$

$$B(\mathbf{u},\mathbf{u}) = \begin{pmatrix} & u_5B_5 + u_6B_6 & u_3B_3 + u_4B_4 \\ -u_5B_5 - u_6B_6 & & u_1B_1 + u_2B_2 \\ -u_3B_3 - u_4B_4 & -u_1B_1 - u_2B_2 & \end{pmatrix} \mathbf{u}, \tag{BT}$$

where $B_1, \ldots, B_6$ are arbitrarily chosen 2×2 real matrices with $\|B_j\| = 1$. Note that the energy conserving nonlinearity acts strictly between the subspaces in which non-normal, transient linear growth occurs, that is, the model (BT) incorporates selection rules.

Figure 3.5 shows evolution curves for (BT). As expected, the bootstrapping effect is weakened. However, it is still present: we have $\alpha = -2$, not $\alpha = -1$. This is readily explained; see Section 3.3. Again there is little qualitative dependence on the nonlinear coefficients: one gets transition with probability close to 1 as in model

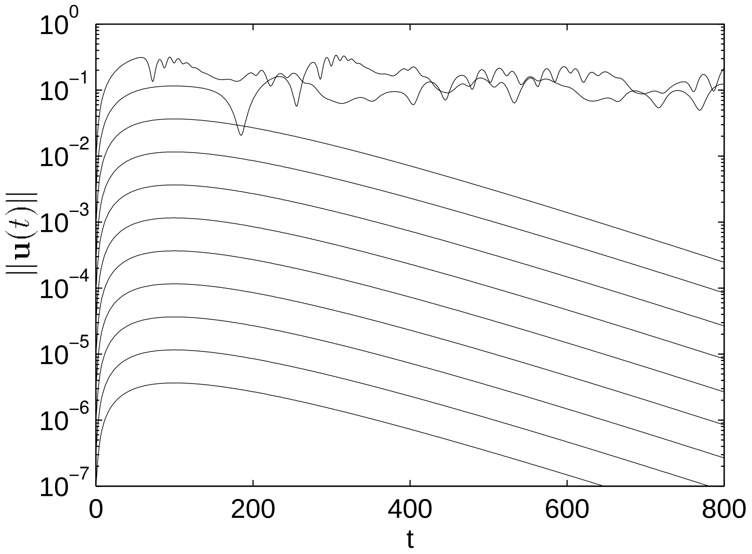

Figure 3.5: Evolution curves for model (BT) (threshold exponent $\alpha = -2$) with $R = 100$. These curves are based upon one particular (random) choice of the matrices B_j in (BT).

(BDT). Thus, even with selection rules, the combination of a non-modal linear amplifier with an essentially arbitrary nonlinear mixer produces a bootstrapping phenomenon. As expected, however, this is our first model for which transition fails to occur if the noise term of (3.2) is removed.

We have now presented plots of $\|\mathbf{u}(t)\|$ vs. t for four low-dimensional models (Figures 3.2–3.5). Do these figures look more or less alike, at least for amplitudes $\|\mathbf{u}\| \ll 1$? That, of course, is precisely the point. Each of the above models has been criticized on the grounds that it is non-physical in some way. While these criticisms were motivated by valid observations about fluid flows, none of them bear on the qualitative behavior of these systems for low disturbance amplitudes or the phenomenon of subcritical transition with $\alpha < -1$.

3.2.2 The W model

All four of the models we have considered thus far view the nonlinearities as a random mixer. We now turn to a model that was conceived in an entirely different manner. This is the model proposed by Waleffe in [97, 98]. It arose from studies of turbulence and regeneration of streaks in the boundary layer of wall-bounded turbulent shear flows. In Waleffe's thinking, the essence of his model is distinctly nonlinear.

Waleffe's work in this area began around 1990 in collaboration with Kim and Hamilton at the Center for Turbulence Research. The questions that led to it were some of those that have been important in studies of turbulence, such as, what determines the spacing of streaks in turbulent boundary layers? As in the recent studies of hydrodynamic stability, it was recognized from the start that the mechanism of streak generation was linear [59]. But the emphasis in this work was on the search for a nonlinear mechanism that might produce a "self-sustaining process" whereby streaks could form, decay, and form again.

In [37] and [99], Waleffe and his colleagues proposed the self-sustaining process diagrammed in Figure 3.6. In the upper-left portion of the loop in that figure, streamwise vorticity generates streamwise streaks by linear advection. The streaks then break down according to an instability that can be viewed as linear and modal, essentially the Kelvin–Helmholtz instability; we discuss this in detail in Chapter 4. Finally, nonlinear interactions occur that recreate streamwise vorticity, and the process continues.

The cycle of Figure 3.6 is not modeled as a system of ordinary differential equa-

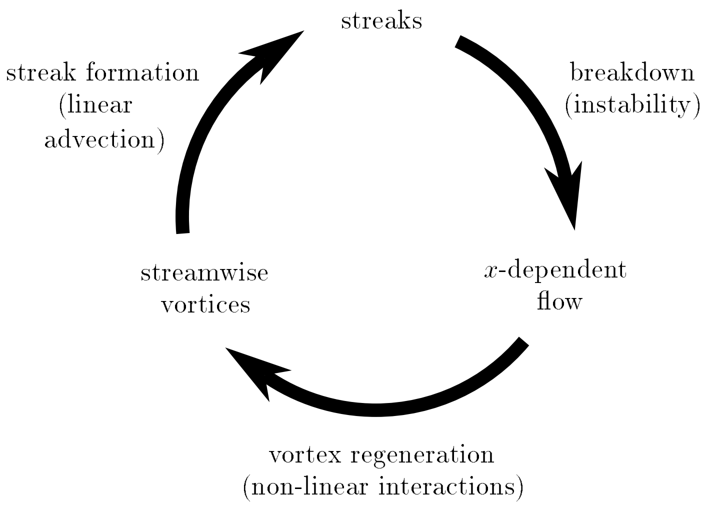

Figure 3.6: Schematic view of a self-sustaining mechanism of turbulence in shear flows at high Reynolds number developed at the Center for Turbulence Research (taken from [37]). The upper-left arrow corresponds to the "linear, non-modal growth" of Figure 3.1 and the other two arrows constitute a proposal of a dominant mechanism of "nonlinear mixing."

tions in [37] and [99]. In reaction to [95], however, Waleffe wrote the paper [97], in which he formulated his views in this way. Upon publication of [2], he wrote a second paper [98] in which the model was generalized to include Reynolds number dependence. This model, containing four real variables, takes the form

$$\begin{aligned}
\dot{u} &= -\lambda R^{-1} u + mv - \gamma w^2 \\
\dot{v} &= -\mu R^{-1} v + \delta w^2 \\
\dot{w} &= -\nu R^{-1} w + \gamma uw - \delta vw \\
\dot{m} &= -\sigma R^{-1} m + \sigma R^{-1} - uv,
\end{aligned} \tag{3.4}$$

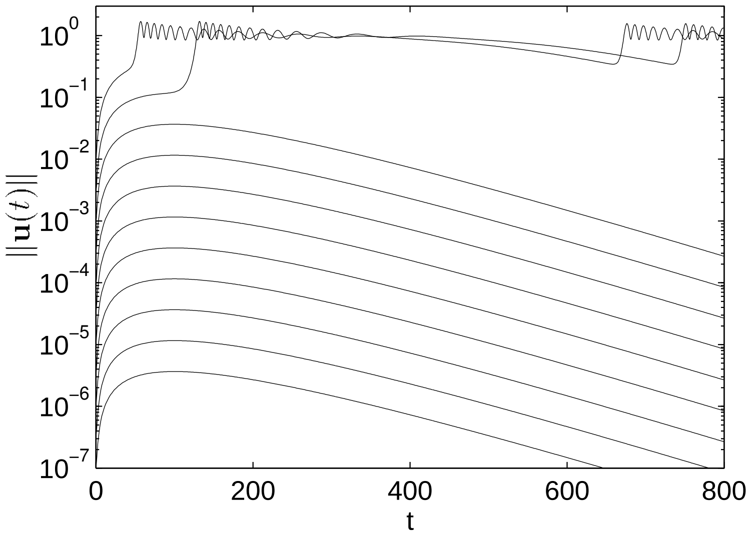

Figure 3.7: Evolution curves for model (W) (threshold exponent $\alpha = -2$) with $R = 100$.

where $\lambda, \gamma, \mu, \delta, \nu, \sigma$ are positive constants of order 1. Unlike the models we have examined so far, the variables in (3.4) are given physical interpretations from the start. Roughly, they represent amplitudes of a streamwise streak (u), a streamwise vortex (v), a streamwise undulation of the streak that renders it unstable (w), and the mean shear amplitude (m). For a laminar flow, the values are $u = v = w = 0$ and $m = 1$.

As written above, Waleffe's equations do not exhibit separation into a linear, non-modal, amplifying term with quadratic nonlinearities. However, this is an artifact of a choice of variables in which the laminar flow corresponds to $m \neq 0$. To regularize this situation, let us define $n = 1 - m$, so that n corresponds to the modification of the mean shear. The equations can now be written in our standard form $(*)$ with terms

$$\mathbf{u} = \begin{pmatrix} u \\ v \\ w \\ n \end{pmatrix} \in \mathbb{R}^4, \qquad A = \begin{pmatrix} -\lambda R^{-1} & 1 & & \\ & -\mu R^{-1} & & \\ & & -\nu R^{-1} & \\ & & & -\sigma R^{-1} \end{pmatrix},$$

$$B(\mathbf{u},\mathbf{u}) = \begin{pmatrix} & & -\gamma w & -v \\ & & \delta w & \\ \gamma w & -\delta w & & \\ v & & & \end{pmatrix}. \tag{W}$$

At first glance, it may appear that the quadratic nonlinearity in (W) does not incorporate selection rules, since the variable w is allowed to affect itself nonlinearly. However, this is a consequence of the way Waleffe has modeled the streak instability through the variable w. In the Navier–Stokes equations the streak instability manifests itself through the nonlinear interaction of the streamwise streaks with many oblique modes (modes with streamwise dependence). Thus the model (W) models selection rules.

Waleffe does not discuss the threshold exponent exhibited by this model, though he notes [98] that there is a branch of unstable solutions along which the variable v scales as $O(R^{-2})$. These unstable solutions are related to the threshold exponent for this model, which we have verified is $\alpha = -2$. The evolution curves are shown in Figure 3.7 for the arbitrary choice $\lambda = \gamma = \mu = \delta = \nu = 1$.

For the study of turbulence, since the perturbations of the laminar state involved are of order 1, an important feature of Waleffe's model is the energy balance reflected in the variable n; perturbations grow by extracting energy from the mean flow. For the study of threshold exponents $\alpha < -1$ for transition, however, it is the behavior of low-amplitude perturbations that dominates. The energy balance is of little consequence so long as $\alpha < -1$, and n can be replaced by zero without changing the threshold exponent $\alpha = -2$.

3.2.3 The KLH model

Numerous contributions have been made to questions of transition over the years by a group of researchers whom we loosely associate with the Royal Institute of Technology in Stockholm. Among the central figures are Dan Henningson, who was a colleague of Waleffe's at MIT for a time, and Peter Schmid, his student at MIT.

In 1992, Henningson and Schmid proposed a three variable model of certain features of transition to turbulence, though without Reynolds number dependence [40]. This model involved three eigenmodes, and the linear term was accordingly diagonal; this was before the group became fully involved in the non-normal developments of [7, 11, 33, 78, 95]. Rather than giving further details, let us turn to a later model proposed by G. Kreiss, Lundbladh, and Henningson. This model appears in a paper explicitly devoted to the question of threshold exponents [55]. Its origin is rather different from the models we have discussed, however, for besides being motivated by the Navier–Stokes equations themselves, it is also designed to illustrate certain points regarding the mathematical techniques used in that paper to analytically derive lower bounds on the threshold exponent for plane Couette flow. The KLH model can be written in the our standard form $(*)$ with terms

$$\mathbf{u} = \begin{pmatrix} u \\ v \\ w \end{pmatrix} \in \mathbb{R}^3, \qquad A = \begin{pmatrix} -R^{-1} & 1 & \\ & -R^{-1} & \\ & & -1 \end{pmatrix}, \qquad B(\mathbf{u},\mathbf{u}) = \begin{pmatrix} \\ w^2 \\ uw \end{pmatrix}. \qquad \text{(KLH)}$$

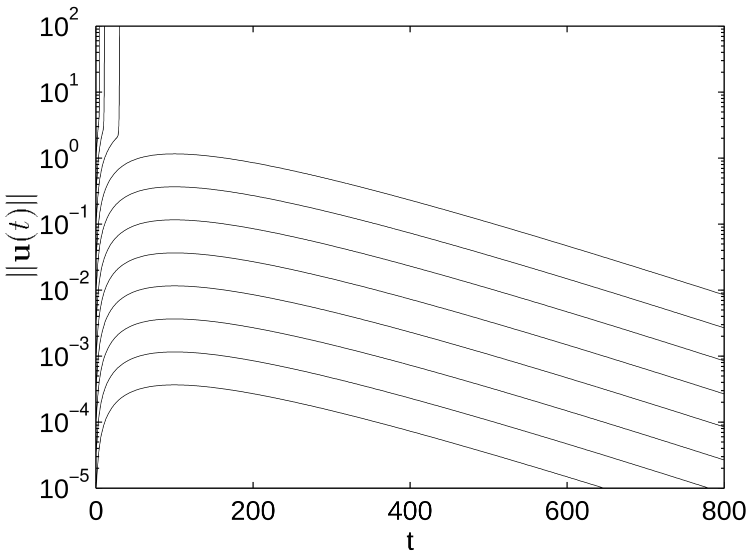

Figure 3.8: Evolution curves for model (KLH) (threshold exponent $\alpha = -1$) with $R = 100$. This is the first of two figures in which bootstrapping does not occur. Note that the vertical scale has been shifted by two orders of magnitude; the initial amplitudes have been correspondingly shifted to $\|\mathbf{u}(0)\| = 10^{-5}, \ldots, 10^{0}$.

Here u represents a streamwise streak, v a streamwise vortex, and w a non-streamwise mode of some kind. The nonlinear term is intended to be suggestive of certain physical processes without capturing them accurately, and energy conservation is intentionally not included in the model to emphasize that energy conservation is not necessarily important in the transition process. Like the other models we have considered, (KLH) contains a non-normal matrix as its linear term. The threshold exponent for transition turns out to be $\alpha = -1$, the first time we have encountered a value that is not < -1. The evolution curves are shown in Figure 3.8.

The reason for the exponent $\alpha = -1$ is easily spotted. The $(3, 3)$ entry of the linear term of (KLH) is -1, not $-R^{-1}$. This term represents convective decay with a decay rate independent of R. In this case, the authors chose -1 because of their observation that the streamwise streak had to reach an amplitude $O(1)$ before a secondary instability could take place in plane Couette flow. However, as we shall observe in Chapter 4, in other flow geometries the amplitude of the streamwise streak necessary for a secondary instability can decrease with the Reynolds number as $R^{-\sigma}$ — a situation for which the KLH model can be easily modified. In that case, we have a model of the form $(*)$ with terms

$$\mathbf{u} = \begin{pmatrix} u \\ v \\ w \end{pmatrix} \in \mathbb{R}^3, \quad A = \begin{pmatrix} -R^{-1} & 1 & \\ & -R^{-1} & \\ & & -R^{-\sigma} \end{pmatrix}, \quad B(\mathbf{u},\mathbf{u}) = \begin{pmatrix} \\ w^2 \\ uw \end{pmatrix}, \qquad (3.5)$$

for some σ presumably in the range $0 < \sigma \leq 1$. As we shall explain in Section 3.3, the threshold exponent becomes $\alpha = -1 - \sigma$. The evolution curves are qualitatively similar to those in Figure 3.8, and we do not show them here.

3.2.4 The JRB model

Not far away in Sweden, another group has been active at the Chalmers Institute for Technology in Göteborg. The manuscript [46], by Claes Johnson and Mats Boman of Chalmers together with Rolf Rannacher of the University of Heidelberg, proposes a three variable ODE model. The motivation for this model is tied to computational fluid mechanics: these researchers are concerned with error control in numerical simulations, a challenging problem since small perturbations may have large and long-lasting effects.

Like Waleffe's equations (3.4), the equations of [46] are not written in our standard linear-plus-quadratic form. However, by replacing the authors' variable $u_1 - 1$

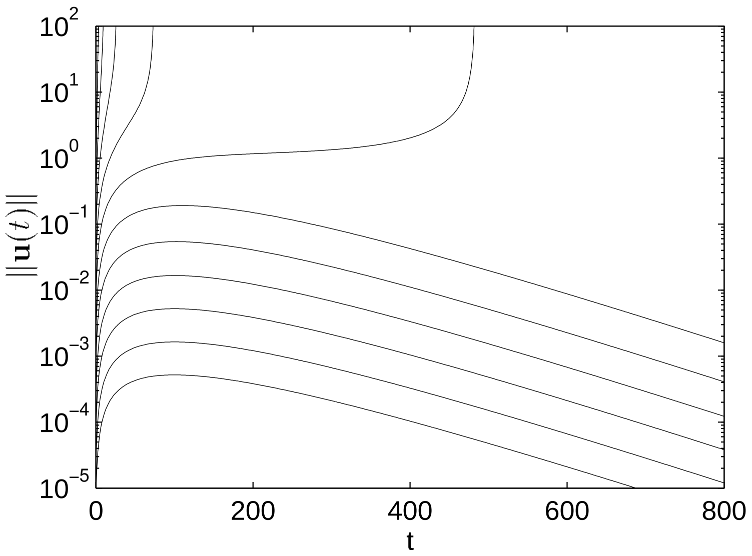

Figure 3.9: Evolution curves for model (JRB) (threshold exponent $\alpha = -1$) with $R = 100$. This is the second of two figures in which bootstrapping does not occur. The vertical scale and the initial amplitudes have again been shifted by two orders of magnitude.

by u, we can remedy this. To facilitate comparisons we also rename other variables of [46] as follows: $R = \nu^{-1}$, $v = u_2$, $w = u_3$, $a = \gamma_{12}$, $b = \gamma_{13}$, $c = \gamma_{31}$. The equations can now be written in our standard form $(*)$ with terms

$$\mathbf{u} = \begin{pmatrix} u \\ v \\ w \end{pmatrix} \in \mathbb{R}^3, \qquad A = \begin{pmatrix} -R^{-1} & a & b \\ & -R^{-1} & \\ & & -R^{-1} \end{pmatrix}, \tag{JRB}$$

$$B(\mathbf{u}, \mathbf{u}) = \begin{pmatrix} auv + buw \\ \\ cR^{-1}uw \end{pmatrix},$$

where a, b, c are nonnegative constants. Note that the variable v in this system evolves linearly, unaffected by the other variables. Unlike the other models considered here with $O(1)$ nonlinear coefficients, this model contains the quadratic coupling term $cR^{-1}uw$. For this reason, the threshold exponent turns out to be $\alpha = -1$. Figure 3.9 shows the energy histories for the model (JRB) where we have made the arbitrary choice of nonlinear coefficients $a = b = c = 1$.

3.2.5 The W2 model

In [99], Waleffe and his colleagues proposed a sequence of interactions through which oblique velocity modes could generate streamwise streaks in a turbulent shear flow. Further nonlinear interactions between the streaks and oblique modes could feed back on the original oblique velocity modes to form a self-sustaining cycle similar to the one depicted in Figure 3.6. The goal of [99] was to isolate a process responsible for the generation and sustenance of streamwise streaks, and the sequence of interactions was described to demonstrate the time scale over which this process might occur.

However, in discussions with us in 1995, Waleffe proposed that the same sequence of interactions could lead to a model of transition to turbulence which both incorporated selection rules and had a threshold exponent $\alpha < -2$. His model, containing five real variables, takes the form

$$\begin{aligned}
\dot{u} &= -R^{-1}u + mv - wx, \\
\dot{v} &= -R^{-1}v + w^2 + x^2, \\
\dot{w} &= -R^{-1}w + mx - vw, \\
\dot{x} &= -R^{-1}x + uw - vx, \\
\dot{m} &= -R^{-1} + R^{-1} - uv - wx.
\end{aligned} \tag{3.6}$$

As in Waleffe's other model (3.4), the variables u, v, m represent, roughly,

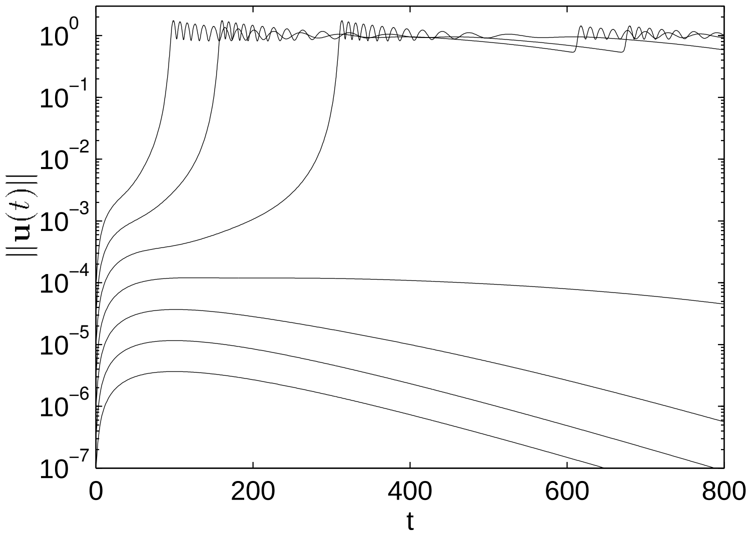

Figure 3.10: Evolution curves for model (W2) (threshold exponent -3) with $R = 100$. Note that only seven curves are shown with initial amplitudes $\|\mathbf{u}(0)\| = 10^{-7}, 10^{-6.5}, \ldots, 10^{-4}$.

the amplitudes of a streamwise streak, a streamwise vortex, and the mean shear, respectively. This model differs from (3.4) in its representation of the the oblique structures whose nonlinear interactions can generate streamwise streaks. In (3.6) the variable w represents the amplitude of a pair of oblique streaks and x the amplitude of a pair of oblique vortices.

As in (3.4), the laminar flow in (3.6) corresponds to $m \neq 0$. By introducing the new variable $n = 1-m$, so that n again corresponds to the modification of the mean shear, the equations can be written as the sum of a linear, non-modal amplifying term and quadratic nonlinearities. Written in our standard form $(*)$ the model has terms

$$\mathbf{u} = \begin{pmatrix} u \\ v \\ w \\ x \\ n \end{pmatrix} \in \mathbb{R}^5, \qquad A = \begin{pmatrix} -R^{-1} & 1 & & & \\ & -R^{-1} & & & \\ & & -R^{-1} & 1 & \\ & & & -R^{-1} & \\ & & & & -R^{-1} \end{pmatrix}$$

$$B(\mathbf{u},\mathbf{u}) = \begin{pmatrix} & & & -w & -v \\ & & w & x & \\ & -w & & & -x \\ w & -x & & & \\ v & & x & & \end{pmatrix} \mathbf{u}. \tag{W2}$$

Note that (W2) contains two distinct linear, non-modal amplifiers — one for u and v, the other for w and x — which represent the transient linear growth of streamwise and oblique streaks, respectively. The nonlinear terms represent particular physical processes, the most important of which, from the point of view of bootstrapping, is the nonlinear interaction of the oblique streaks which feeds the streamwise vortices. This appears as the w^2 in the equation for v.

Because of the way the nonlinear terms link together the two non-modal linear amplifiers, through selection rules, this model bootstraps and exhibits a threshold exponent $\alpha = -3$. This was originally stated by Waleffe and we have verified it here. The evolution curves are shown in Figure 3.10. The initial conditions in Figure 3.10 are of the form (3.2) where $\mathbf{u}_{\text{opt}}$ is chosen as the vector which leads to the most linear transient growth for the w and x variables. (It is possible to choose $\mathbf{u}_{\text{opt}}$ so that u is transiently amplified and this also bootstraps, again with $\alpha = -3$.)

3.3 Why these figures all look alike: two views of streak instability

We come now to the mathematical heart of this chapter. Why do all the curves we have presented look so similar, at least as long as the amplitudes remain $\ll 1$? The Cornell and Marburg groups speak of "nonlinear mixing," and Waleffe and the Swedish groups speak of "streak instabilities" and other physical notions, but these are different ways of looking at the same phenomenon. In a system exhibiting linear, non-modal, transient growth, more or less arbitrary nonlinearities may produce a "streak instability;" one does not have to put it in the model specifically.

We now present heuristic arguments that explain the threshold exponents we have observed. Each of these models contains a linear, non-modal amplifier of gain $O(R)$ and time scale $O(R)$. Consider the following caricature. The output of the amplifier (the relatively high-amplitude quantity in the early stages of the transition process) is a variable $\phi(t)$. All other quantities of interest, including the input to the amplifier, are represented by another variable $\psi(t)$ (potentially of much lower amplitude in the early stages of transition). Both ϕ and ψ start with amplitude ϵ. The variable $\phi(t)$ grows to size ϵR by linear, non-modal effects and lingers at that level for a time $O(R)$. The variable ψ grows by quadratic interactions

$$\dot{\psi} \approx \phi\psi, \qquad \psi(0) \approx \epsilon, \tag{3.7}$$

hence for a period of duration $O(R)$,

$$\dot{\psi} \approx \epsilon R\psi, \qquad \psi(0) \approx \epsilon, \tag{3.8}$$

with solution

$$\psi(t) \approx \epsilon e^{\epsilon R t}, \qquad\qquad 0 \le t \le O(R). \tag{3.9}$$

All together, we predict exponential growth at a rate ϵR up to an amplitude of order $\epsilon e^{\epsilon R^2}$. Unless ϵR^2 is bounded, this corresponds to growth by an arbitrary factor, so that ψ may achieve amplitude $O(1)$, after which anything may happen. In other words, the threshold exponent for "transition" in (3.7)–(3.9) is $\alpha = -2$.

Models (BT) and (W) fit the pattern just described. In the model (W) the variable u plays the role of ϕ and in the model (BT) this role is played by u_1. In each case, the remaining variables play the role of ψ. In the model (W), for example, the term uw represents the quadratic interaction $\phi\psi$ of (3.7), feeding energy back from the output of the linear amplifier (u) into the rest of the system (v and w). Easy modifications of this argument explain why the models (KLH), (3.5), and (JRB), have threshold exponents $\alpha = -1$, $\alpha = -1 - \sigma$, and $\alpha = -1$, respectively.

In (3.7) there is no quadratic term ϕ^2. The absence of this term is the representation within (3.7)–(3.9) of the crucial "selection rule" of the kind discussed earlier. Physically, we may think of the fact that a purely streamwise streak, no matter how large in amplitude, cannot by itself feed energy into modes that are not independent of the streamwise coordinate. By contrast, if we have a system with no such selection rule, we can caricature it by changing $\phi\psi$ to ϕ^2 in (3.7). Equations (3.7)–(3.9) become

$$\dot{\psi} \approx \phi^2, \qquad\qquad \psi(0) \approx \epsilon, \tag{3.10}$$

$$\dot{\psi} \approx (\epsilon R)^2, \qquad\qquad \psi(0) \approx \epsilon, \tag{3.11}$$

$$\psi(t) \approx (\epsilon R)^2 t, \qquad\qquad 0 \le t \le O(R), \tag{3.12}$$

leading to $\psi(t) = O(\epsilon^2 R^3)$ at $t = O(R)$. Now, if $\epsilon^2 R^3$ is of order ϵ or greater, then ψ may be larger at $t = O(R)$ than it was at $t = 0$. Another round of amplification may begin, leading to self-sustaining growth up to amplitude $O(1)$. In other words, the threshold exponent for "transition" in (3.10)–(3.12) is determined by the condition $\epsilon = \epsilon^2 R^3$, giving $\alpha = -3$ [95]. Models (GG) and (W2) fit this pattern. In the case of (W2), ϕ corresponds to u and w, and ψ corresponds to v, x, and n. Models (TTRD) and (BDT) also fit this pattern, though the quadratic nature of the nonlinearity is obscured by the use of the norm $\|\mathbf{u}\|$.

The two-variable caricature (3.7)–(3.9) has more physics in it than one might expect. In this pair of equations, the presence of an approximately steady high-amplitude signal $\phi(t)$ makes it possible for a second signal $\psi(t)$ to grow exponentially over many orders of magnitude. This is nothing more than an abstract description of a linear secondary instability. As we will discuss further in Chapter 4, in the case of the breakdown of a streamwise streak, ϕ corresponds to the amplitude of the streak and ψ to, among other quantities, the amplitude of a deviation from perfect streamwise independence. The exponential growth of such deviations, just as in (3.9), appears strikingly in certain Navier–Stokes simulations of transition to turbulence from initial perturbations consisting of streamwise vortices plus noise; see Figure 4.1 in Chapter 4 (page 71). Note that (3.8)–(3.9) predict that the growth rate of the instability should be proportional to the amplitude of the streak. This is indeed true in some cases, as demonstrated in [79] and in the next chapter.

Table 3.1: Summary of the models and some of their properties.

	model	threshold exponent α	energy conserving nonlinearity?	authors determined α?
without selection rules	TTRD	-3	yes	yes
	BDT	-3	yes	yes
	GG	-3	yes	no
with selection rules	BT	-2	yes	yes
	W	-2	yes	no
	KLH	-1	no	yes
	JRB	-1	no	no
	W2	-3	yes	yes

3.4 Summary

The compressed discussions of this chapter cannot begin to do justice to the wide range of physical ideas put forward by the more than a dozen authors whose works we have compared. Mathematically, however, the low-dimensional models proposed by these authors have much in common. All are small systems of ordinary differential equations that combine a non-normal linear term with a quadratic nonlinearity. In each case the zero solution is mathematically stable, but small perturbations can be amplified by factors $O(R)$ over a time period $O(R)$. We summarize some properties of these models in Table 3.1. In most cases the nonlinearities are such that a "bootstrapping" phenomenon may occur, causing the threshold exponent for "transition" to be strictly less than -1.

For actual fluid flows, the evidence concerning threshold exponents is sparse. What does seem clear, based on Navier–Stokes simulations, is that α is strictly less than -1 for plane Couette flow ($\alpha \leq -5/4$?) and plane Poiseuille flow ($\alpha \leq -7/4$?) [63]. (In the case of plane Poiseuille flow this refers to transition by routes unrelated to the linear instability of Tollmien–Schlichting waves for $R > 5772$. For pipe Poiseuille flow, there are as yet no computations concerning threshold exponents.) In principle, the actual exponents might be much less than these estimates, but numerical experiments by Baggett (see Chapter 4), Henningson, Lundbladh, Reddy, and Schmid have revealed no evidence of this so far. In view of this experimental situation and the fact that the Navier–Stokes equations contain selection rules of the kind that we have discussed, a reasonable guess is that for actual flows in pipes and channels, the true values of α lie in the range $-2 \leq \alpha < -1$.

Chapter 4

Why plane Poiseuille flow is less stable than plane Couette flow: The dual nature of shear*

4.1 Streamwise vortices and streaks in transition to turbulence

Streamwise vortices, elongated regions of streamwise vorticity, and streamwise streaks, regions of relatively high- and low-speed fluid elongated in the streamwise direction, are dominant structures in the near-wall region of turbulent shear flows [37, 49, 51, 54]. These structures also play an important role in transition

*See also Appendix A, where we present details about the numerical methods and computational resources used for the investigations of this chapter.

to turbulence in shear flows [36, 50]. Klingmann [52] observed experimentally that localized disturbances in plane Poiseuille flow developed into "elongated streaky structures with strong spanwise shear," i.e., streamwise streaks, before decaying or developing into turbulent spots, depending on the amplitude of the initial disturbances. Streamwise vortices occur in shear layers [6, 44, 57, 85] and in Görtler flow (boundary layer flow over a curved wall) [8, 73, 91]. Dauchot and Daviaud [18] studied transition from streamwise vortices by inducing them in a slightly modified plane Couette flow. In later work with Bottin [10] they concluded that streamwise vortices are both sufficient and necessary for subcritical transition in plane Couette flow. Butler and Farrell [11] established that streamwise vortices are the initial conditions leading to the greatest linear transient growth in plane Couette flow and plane Poiseuille flow (more on this in Section 4.2).

In this chapter, we are primarily interested in subcritical transition to turbulence in plane Couette flow (hereafter PCF) and plane Poiseuille flow (PPF). In both of these flows, small streamwise vortices lie at the beginning of a path which can lead to turbulence [36, 50, 55, 63]:

$$\begin{array}{c}\text{streamwise}\\\text{vortices}\end{array} \rightarrow \begin{array}{c}\text{streamwise}\\\text{streaks}\end{array} \rightarrow \begin{array}{c}\text{wavy}\\\text{streaks}\end{array} \rightarrow \text{turbulence.} \qquad (*)$$

In the first stage of $(*)$, small streamwise vortices generate streamwise streaks via the shear tilting mechanism; see Figure 4.5. We review this stage in Section 4.2. As the streamwise streaks develop, the spanwise profile of the streamwise velocity develops inflection points; see Figure 4.8. Under the right conditions, as we explain in this chapter, these inflection points can cause the streamwise streaks to be linearly unstable, that is, the initial streamwise vortices can generate a secondary instability. This happens when the initial streamwise vortices are sufficiently large. The instability, of Kelvin–Helmholtz type, leads to the exponential growth of certain oblique waves in the second stage of ($*$); see Figure 4.1. As the oblique waves grow, they produce spanwise oscillations in the streamwise streaks which we call wavy streaks; see Figure 4.3. In Section 4.3 we describe the streak instability, that is, the secondary instability of the streamwise vortices.

Throughout this chapter, all lengths are scaled by the channel half-height (h), velocities by the difference between the wall and centerline velocities (V_d), and time by (h/V_d). The Reynolds number is $R = hV_d/\nu$, where ν is the kinematic viscosity.

At subcritical Reynolds numbers, finite amplitude perturbations to the laminar solution are required to initiate transition to turbulence. In the past three years, much work has been done to understand the relationship between the Reynolds number and the size of the smallest disturbances that can initiate transition. Motivated by the conjecture on threshold exponents of Trefethen, *et al.* [95] (see our discussion in Chapter 1, page 6), G. Kreiss, Lundbladh, and Henningson [55] determined, via direct numerical simulations, that the amplitude (based on the energy norm) of the smallest streamwise vortices that can initiate transition in PCF scales as $\approx R^{-1}$, for $R \in [500, 4000]$. Similarly, Lundbladh, Henningson, and Reddy [63] showed, again using direct numerical simulations, that the threshold amplitude of the initial streamwise vortices to cause transition in PPF scales as $\approx R^{-7/4}$ for $R \in [1500, 5000]$.

More recently, Reddy, Schmid, and Baggett [79] applied a linear stability analysis

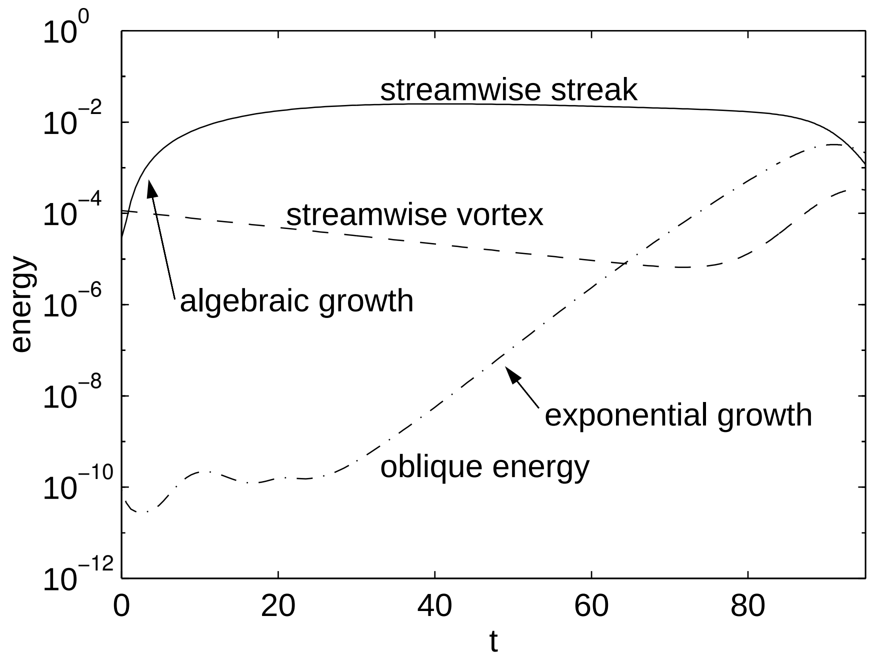

Figure 4.1: Energies in selected wave components for a Navier–Stokes simulation in plane Couette flow (PCF) with ($R = 500$). Secondarily unstable streamwise vortices (with spanwise wavenumber $\beta_0 = 2$ and amplitude $\epsilon = 0.027$) are added at $t = 0$ along with noise of total energy approximately 10^{-8}. The curve labeled *streamwise streak* is the energy in the streamwise velocity of the fundamental $(0, 2)$ mode; the curve labeled *streamwise vortex* is the energy in the vertical velocity component of the same mode. The curve labeled *oblique energy* is the energy in all components of the $(1, 1)$ mode.

to the streamwise streaks and determined that the threshold amplitude of secondarily unstable streamwise vortices (those that generate linearly unstable streaks) scales as $\approx R^{-1}$ and $\approx R^{-1.6}$ in PCF and PPF, respectively. In PPF, all of the above scaling results were determined at subcritical Reynolds numbers $R < 5772$. It would be possible to extend these results to higher Reynolds numbers in PPF by comparing the time scales for transition along the path described by $(*)$ and for

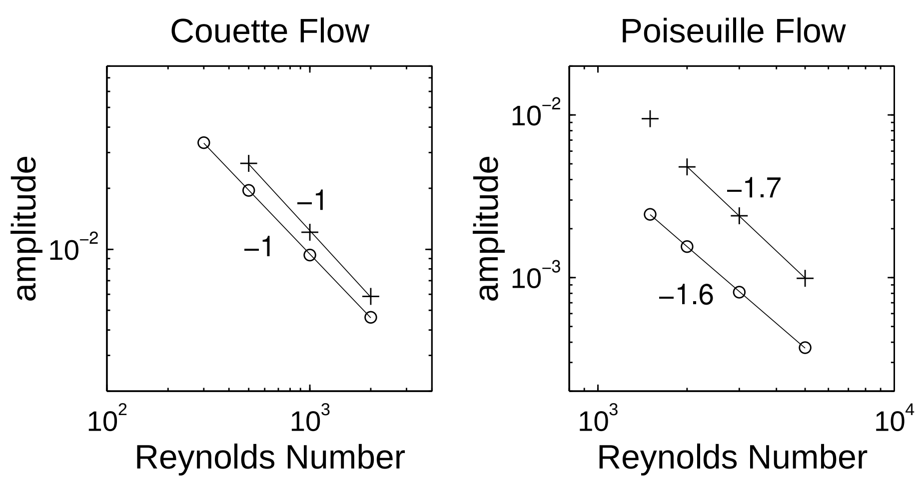

Figure 4.2: Neutral stability curves for the linear instability of streamwise streaks. All data is from [79] and the spanwise wavenumber of initial streamwise vortices is fixed at $\beta_0 = 2$. The circles are the values of the threshold amplitude of streamwise vortices for generating linearly unstable streaks as computed by a linear stability analysis (we describe this in Section 4.5). The crosses are threshold values for transition to turbulence from optimal streamwise vortices based on full Navier–Stokes simulations. The lines are least-squares fits of the data (note that one point is excluded in Poiseuille flow). The numbers near each line are their approximate slopes.

transition initiated by linearly unstable Tollmien–Schlichting waves, but we have not done so here.

The plots in Figure 4.2 summarize the threshold amplitude scalings computed in [79]. PPF is less stable than PCF in the sense that smaller streamwise vortices can both generate linearly unstable streaks and cause transition. At the smallest Reynolds numbers for which turbulence occurs (≈ 300 to 350 in PCF, and ≈ 1000 in PPF), the amplitude of the critical streamwise vortices is approximately an order of magnitude lower in PPF. Moreover, the threshold amplitude of the critical vortices decreases much faster with increasing Reynolds number.

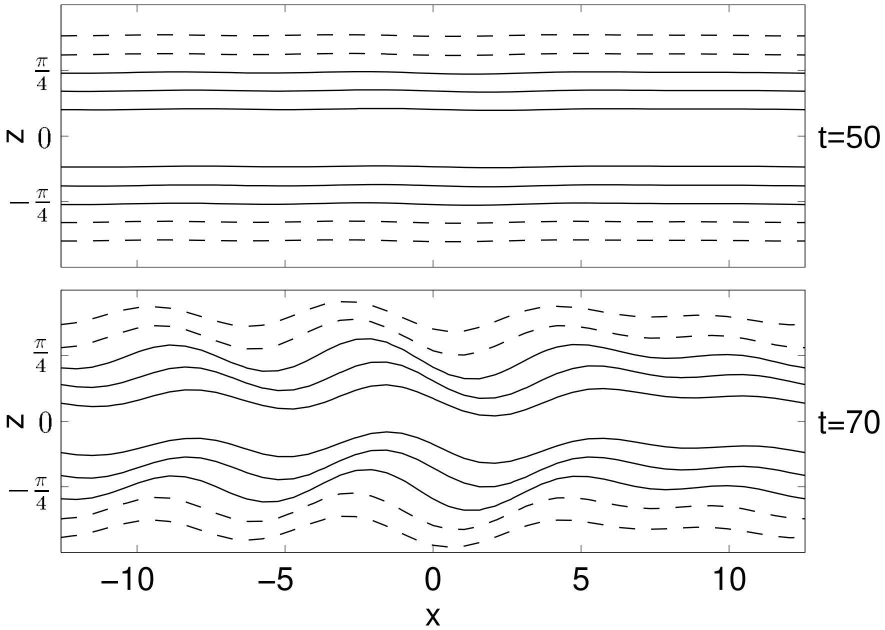

Figure 4.3: Streamwise streaks evolve into wavy streaks in plane Couette flow (PCF) (same initial data as in Figure 4.1). Pictured are lines of constant streamwise velocity $u = -.4, -.2, 0, .2, .4$, in the plane $y = 0$, midway between the channel walls. Dashed lines indicate fluid moving to the left ($u < 0$), and solid lines fluid moving to the right ($u \geq 0$).

Why do smaller streamwise vortices cause transition to turbulence in PPF than in PCF? Why do the threshold amplitudes scale differently? These questions are the organizing theme for this chapter.

We will show that the different scalings arise from the nature of the streak instability in the second stage of ($*$). At the end of the first stage the velocity field is dominated by the streamwise streaks (for sufficiently large Reynolds numbers). The streamwise streaks consist primarily of spanwise varying streamwise velocity, that is, they are primarily vertical vorticity. The spanwise profile of the streamwise velocity contains inflection points which can cause the "roll up" of vertical vorticity into vertical vortices — essentially a Kelvin–Helmholtz instability — if, roughly speaking, the streaks vary more quickly in the spanwise direction than in the direction normal to the walls at the inflection points. Figure 4.4 shows the formation of vertical vortices in PCF for the same initial data as in Figure 4.1.

The contest between spanwise and vertical shear to establish the stability or instability of streaks points to a basic difference between PCF and PPF which lies at the heart of this chapter. In PCF the laminar solution is a uniform shear flow, so that the streamwise streaks have to grow rather large to generate enough spanwise variation to overcome the influence of the vertical shear, that is, the uniform shear inhibits the formation of vertical vortices. On the other hand, in PPF, the parabolic laminar solution exhibits a region of little shear near the channel center in which considerably smaller streaks can be unstable.

Thus the main point of this chapter is that the different threshold amplitude scalings of streamwise vortices in PCF and PPF are determined by the shear present in the laminar flow. Shear plays a dual role in the path to turbulence described by $(*)$ — it enables the generation of large streamwise streaks from small streamwise vortices, but it also inhibits the linear instability of the streaks.

The streamwise streaks represent an important crossroads in this route to turbulence. The streaks grow by extracting their energy from the underlying laminar flow (modifying it in the process) and, if they are sufficiently large, they transfer some of their energy to certain exponentially growing oblique waves. If the exponential growth is sustained (the streaks maintain a large enough amplitude over a long enough time period), then turbulence quickly follows at sufficiently large Reynolds

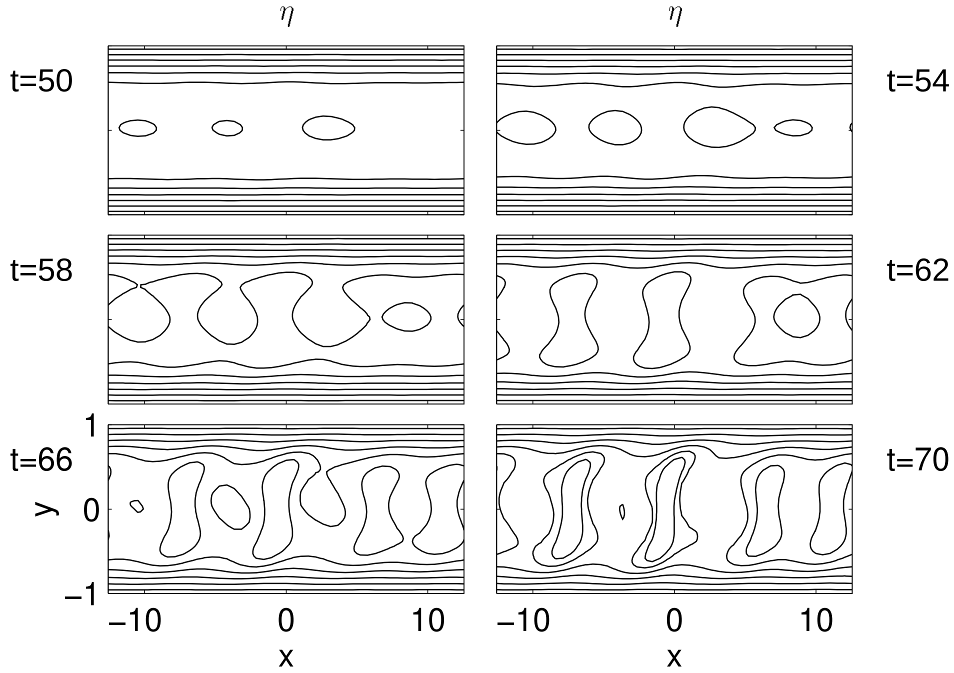

Figure 4.4: Formation of vertical vortices in PCF. Pictured are lines of constant vertical vorticity $\eta = -0.9, -0.74, \dots, -0.1$ in the x-y-plane at the inflection point $z = \pi/4$ (see Figures 4.3 and 4.10). Note that the vertical vortices start to form in the channel center, where the shear has been reduced (more on this in Section 4.7), and as they grow they begin to feel the effects of the shear near the walls.

numbers. We have not explored the details of this final stage of $(*)$.

There is evidence that the process described by $(*)$ is also important for fully developed turbulence in PCF, PPF, and related shear flows. Hamilton, Kim, and Waleffe [37] described a regeneration cycle for sustaining near-wall turbulence, consisting of three phases: "formation of streaks by streamwise vortices, breakdown of the streamwise streaks, and regeneration of the streamwise vortices." Waleffe further explored this cycle in the context of plane Couette flow in [97] (Figure 3.6 from [97] in Chapter 3 is a schematic diagram of this cycle).

We have three primary motivations for this chapter. One is to further the understanding of the physical processes at work in the second phase of the path to turbulence described by $(*)$. Another is to further the quest for the disturbances of smallest amplitude, and their corresponding threshold exponents (see Chapter 1), which can cause transition to turbulence. A third motivation is to show that the non-normality of the linear operator governing the evolution of small perturbations to the laminar flow can lead to important nonlinear effects — that non-normality triggers nonlinearities.

In Section 4.2 we review the physics and mathematics of the first stage of $(*)$, in which small streamwise vortices can generate large streamwise streaks in shear flows. We discuss the linear instability of the streamwise streaks, that is, the secondary instability of the initial streamwise vortices, in Section 4.3. In Section 4.4 we use Navier–Stokes simulations to examine the dependence of the streak instability growth rate on the initial streamwise vortex amplitude. The threshold amplitude of the streamwise vortices for generating linearly unstable streaks is a lower bound on the threshold amplitude of the streamwise vortices necessary to cause transition. In Section 4.5 we review the linear stability analysis of the streaks developed by Reddy, Schmid and Baggett in [79]. In that paper, the linear stability analysis was used to compute threshold scalings of the initial vortices. In this thesis, we compute threshold scalings via direct numerical simulations (some simulations were also included in [79] to check the accuracy of the linear stability analysis). The results are in excellent agreement. We describe some of the differences in the two analyses in Section 4.5. In Section 4.6 we explain the threshold scaling in PPF. We introduce a model of the streamwise streaks in PCF in Section 4.7. The model elucidates the physics of the streak instability and allows us to explain the threshold scaling in PCF. Finally, in Section 4.8 we summarize our results.

4.2 Streak generation

Throughout, (x, y, z) and (u, v, w) refer to the streamwise, vertical or wall-normal, and spanwise positions and velocities, respectively. A small streamwise vortex in a shear region rotates some of the fluid into the spanwise direction, where it appears as a large perturbation in the streamwise velocity, that is, as a streamwise streak; see Figure 4.5. This linear mechanism, known as shear tilting, results in linear growth of the streamwise streaks until the growth is shut off by viscous effects[1]. Landahl [56] named this mechanism "lift up" after the "lifting up" of fluid elements by the vertical velocity perturbation. It is also known as vortex tilting. We do not describe the mechanism in detail here, but we note that shear is crucial for the generation of streamwise streaks from streamwise vortices, and moreover, that this is a generic linear mechanism capable of producing large perturbation growth in any parallel shear region; see [23, 56] for detailed discussions of this essentially inviscid mechanism. Mathematically, the transient growth of streamwise streaks, and more generally *any* growth of perturbations in PCF and PPF, can be attributed to the non-normality of the linearized operator which governs the evolution of small perturbations to the laminar flow; see [39].

[1]For example, the growth might be something like *streak amplitude* $\approx O(\epsilon\, t e^{-t/R})$, where ϵ is the amplitude of the initial streamwise vortex.

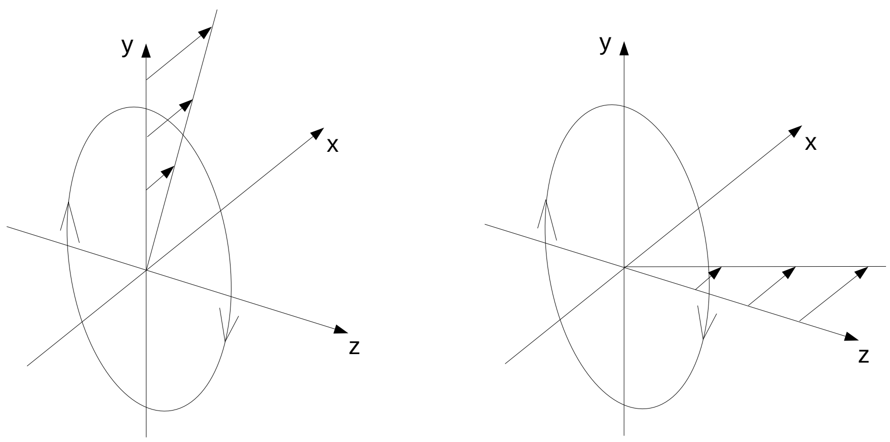

Figure 4.5: The shear tilting mechanism. Streamwise vortices tilt the shear into the spanwise direction, creating streamwise streaks. Reprinted with permission from [97].

The initial streamwise vortices in our study have the form

$$(u_0, v_0, w_0) = C(\hat{u_0}(y)\cos\beta_0 z, \hat{v_0}(y)\cos\beta_0 z, \hat{w_0}(y)\sin\beta_0 z)\,, \qquad (4.1)$$

where β_0 is the fundamental spanwise wavenumber, $C > 0$ is a constant, and $\hat{u_0}(y)$, $\hat{v_0}(y)$, $\hat{w_0}(y)$ are real. The functions $\hat{u_0}(y)$, $\hat{v_0}(y)$, and $\hat{w_0}(y)$ are computed so that (4.1) corresponds to the optimal streamwise vortices of Butler and Farrell [11], which produce the greatest transient linear growth. In the linearized equations for PCF and PPF, optimal streamwise vortices of amplitude ϵ (based on the energy norm) generate streamwise streaks of amplitude $O(\epsilon R)$ over a time period $O(R)$. This is also true in the fully nonlinear equations if $\epsilon R \ll 1$. However, for larger streamwise vortices, the nonlinear development of the resulting streamwise streaks flattens the mean flow, via a Reynolds stress produced by the nonlinear interaction of the streamwise streaks and vortices, in such a way that the non-normality

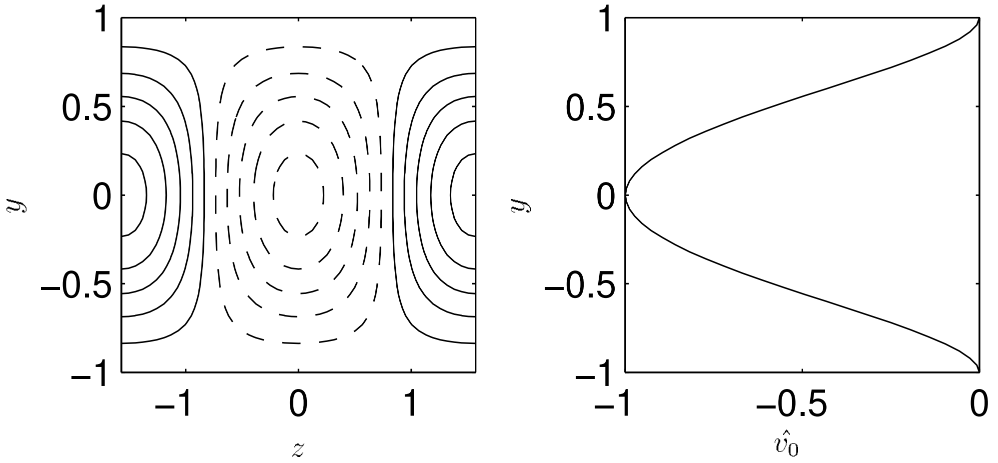

Figure 4.6: The vertical velocity component of the optimal streamwise vortices in plane Couette flow. The left plot shows level surfaces of the vertical velocity v_0 in the y-z-plane, with dashed lines indicating fluid moving down ($v_0 < 0$) and solid lines indicating fluid moving up ($v_0 > 0$). The right plot shows the y-dependence $\hat{v}_0(y)$ of the vertical velocity component of the optimal streamwise vortices.

and hence the potential for transient growth are reduced, and the amplitude of the streaks saturates at size $O(1)$.

The optimal streamwise vortices in PCF are pictured in Figure 4.6. In PPF, the symmetry of the laminar flow may be exploited to consider separately optimal initial conditions with even and odd vertical velocity. Butler and Farrell [11] demonstrated that streamwise vortices with even vertical symmetry ($\hat{v}_0(y)$ is an even function of y, $\hat{u}_0(y)$ and $\hat{w}_0(y)$ are odd) produce the greatest linear, transient growth. However Lundbladh, Henningson and Reddy [63] used direct numerical simulations to show that the threshold amplitudes for transition from initial streamwise vortices with odd symmetry are smaller[2]. Thus, in PPF, we confine our attention to optimal odd

[2]Recent work by Diedrichs [21] indicates that certain key nonlinear interactions between the streaks and the oblique waves may vanish because of symmetry for

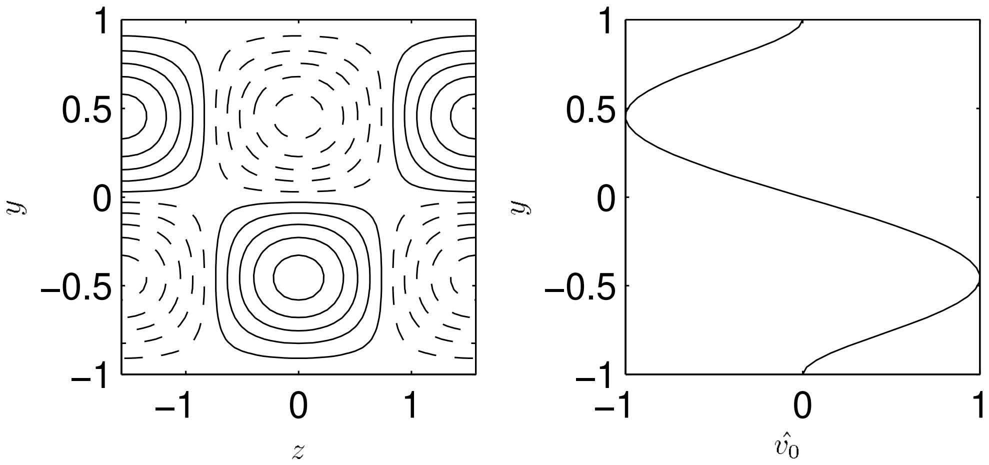

Figure 4.7: The vertical velocity component of the optimal odd streamwise vortices in plane Poiseuille flow. The left plot shows level surfaces of the vertical velocity v_0 in the y-z-plane with dashed lines indicating fluid moving down ($v_0 < 0$) and solid lines indicating fluid moving up ($v_0 > 0$). The right plot shows the y-dependence $\hat{v_0}(y)$ of the vertical velocity component of the optimal streamwise vortices.

streamwise vortices as shown in Figure 4.7. The optimal streamwise vortices also have small nonzero spanwise varying spanwise and streamwise velocity components, but the critical component is the vertical velocity, which redistributes the streamwise momentum and creates streamwise streaks. For a full discussion of optimals, see [11].

The nonlinear evolution of the streamwise vortices results in a streamwise independent velocity field with streamwise component of the form

$$U(y, z, t) = \sum_{k=0}^{\infty} U_k(y, t) \cos(k\beta_0 z), \tag{4.2}$$

where the U_k are real. We have switched to the notation $U_k(y, t)$ for emphasis because we will be linearizing about this state later. Figure 4.8 shows the streamwise streaks generated in PCF from optimal streamwise vortices with spanwise wavenum-

even streamwise vortices in PPF.

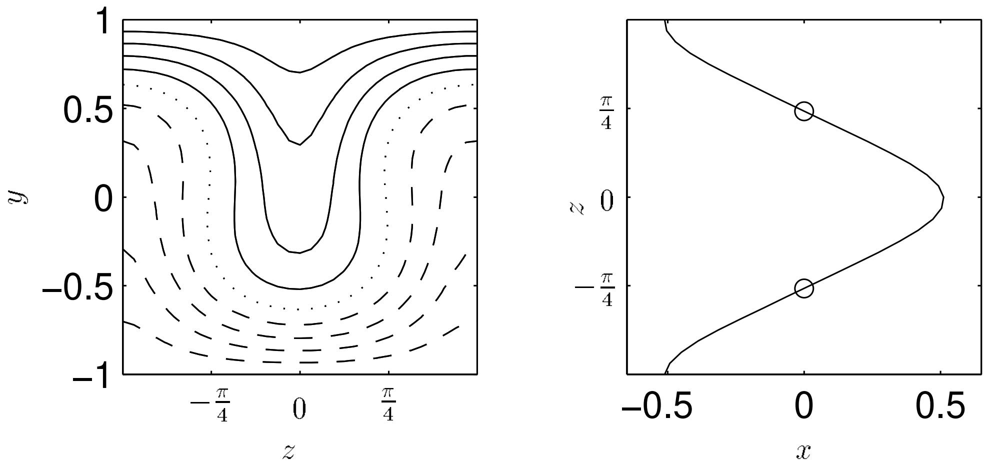

Figure 4.8: Streamwise streaks in PCF from a full nonlinear simulation with the same initial data as in Figure 4.1 at $t = 50$. The left figure shows contours of the streamwise velocity in PCF in the y-z-plane. The lines are spaced at $-.8, -.6, ..., .8$, with solid lines indicating fluid with $U > 0$, dashed lines fluid with $U < 0$, and the dotted line at $U = 0$. The right plot shows the streamwise velocity profile at the channel center, $U(0, z, 50)$; circles mark the inflection points.

ber $\beta_0 = 2$.

4.3 Streak breakdown*

Sufficiently large streamwise streaks may be linearly unstable to disturbances which break the streamwise independent symmetry of the streaks. The instability is usually attributed to the inflectional spanwise profile of the streamwise velocity generated by the growth of the streamwise streaks. Reddy, Schmid, and Baggett [79] applied a linear stability analysis to the streamwise streaks in PCF and PPF and confirmed the inflectional nature of the instability. Waleffe [97], in his study of a

*Parts of this section are adapted from [79].

self-sustaining mechanism of turbulence in PCF, also states that the streak instability "is wakelike, resulting from the spanwise inflections" in the streamwise velocity profile. Yang [102] found experimentally that even a single streamwise vortex induced spanwise inflection points in the streamwise velocity profiles in water table flow, but that transition occurred only when the initial vortex was sufficiently large. Klingmann [52] observed experimentally in PPF that a sufficiently large localized disturbance produced streamwise streaks which developed a "wavelike spanwise motion" before the disturbance developed into a turbulent spot.

The spanwise inflectional instability of streaks has also been studied in a number of other flow geometries. In boundary layer flow over a curved wall the vortices are called Görtler vortices; see [88] for a review. In this geometry there are two types of unstable modes. In most cases, the most unstable is a *sinuous* mode, similar to that in Figure 4.3. In addition there is a *varicose* mode, which is symmetric in the spanwise direction. Streak breakdown was studied experimentally by Swearingen and Blackwelder [91]. They associated breakdown with "strongly" inflectional streamwise velocity profiles. The breakdown was studied via an inviscid linear analysis by Hall and Horseman [35]. Yu and Liu [103] showed that the sinuous and varicose modes are correlated with inflection points in the spanwise and streamwise directions, respectively. Bottaro and Klingmann [8] applied a linear stability analysis to the viscous case and confirmed the results of Yu and Liu. In addition, they concluded that the breakdown was primarily inviscid in nature. Li and Malik [61] performed an inviscid linear stability analysis and found that for some parameter combinations the varicose mode is the most unstable.

In Dean flow, curved channel flow driven by a pressure gradient, Dean vortices develop if the Reynolds number is sufficiently large. By linear analysis and direct simulations, Finlay, J. Keller, and Ferziger [24] found two types of instability. A spanwise inflectional instability occurs for Reynolds numbers R above twice the critical value R_c for the primary instability. There is also a second instability, called undulating, that occurs if $R > 1.3R_c$. By considering one-dimensional streak profiles of the form $U(y)$ and $U(z)$, Le Cunff and Bottaro [58] concluded that the undulating instability is centrifugal in nature (so it should play no role in PPF, which is the no-curvature, narrow-gap limit of Dean flow; see [15]). Matsson and Alfredsson [65] observed the spanwise inflectional instability experimentally.

Streak breakdown also occurs in boundary layer flows over a flat plate. Fischer and Dallman [25] investigated the primary and secondary instability of a three-dimensional boundary layer using a laminar Falker–Skan–Cook profile and a spanwise varying finite-amplitude state obtained from measurements. They found good agreement between a secondary instability analysis and experimental results. Bakchinov, *et al.* [4] observed streak breakdown experimentally by directly putting streamwise vortices in the flow. Matsubara and Alfredsson [66] observed instability, as in Figure 4.3, just before breakdown of streaks into turbulent spots.

Zikanov [105] considered the evolution of streamwise vortices in pipe Poiseuille flow. He found that streamwise vortices generated spanwise inflectional streamwise streaks which were linearly unstable for sufficiently large initial vortices.

The wavy streaks are also related to finite amplitude solutions recently discovered in PCF. These solutions, called Wavy Vortex flows, are streamwise streaks with streamwise oscillations as in Figure 4.3. Nagata [68] and Conley and Keller [16] obtain these solutions by considering the narrow-gap limit of Taylor–Couette flow, which is flow between rotating cylinders. Clever and Busse [14] have also identified these solutions by considering PCF between heated plates in the limit of vanishing temperature gradient. Conley [15] and Clever and Busse [13] use similar approaches to study streamwise streaks in PPF.

The classical instability of inflectional type is the Kelvin–Helmholtz vortex sheet instability, in which the inviscid base flow is two-dimensional and unbounded and the vortex sheet is due to a velocity discontinuity. To develop an understanding of the streak instability we consider the the two-dimensional stability, in an unbounded fluid, of the inviscid base flow

$$\bar{U} + S\cos\beta_0 z \tag{4.3}$$

with $\bar{U}$ and S real, to perturbations in the x-z-plane, as considered by Waleffe in [97]. Here $\bar{U}$ is the speed of the constant mean flow and S is the streak amplitude. It is assumed that $v = 0$ and that the perturbations are independent of y. The instability results from the inflection points in the spanwise profile and is fundamental, that is, it has the same spanwise period as the base flow.

Since the base flow has zero phase speed, the disturbances may be divided into sinuous and varicose modes. The varicose modes are found to be stable. The sinuous vertical vorticity with streamwise wavenumber α_0 has the form

$$\eta(x,z,t) = \mathrm{Re}\left[e^{i(\alpha_0 x - \sigma t)}\big(\eta_0 + \sum_{k=1}^{\infty} \eta_k \cos(k\beta_0 z)\big)\right]. \tag{4.4}$$

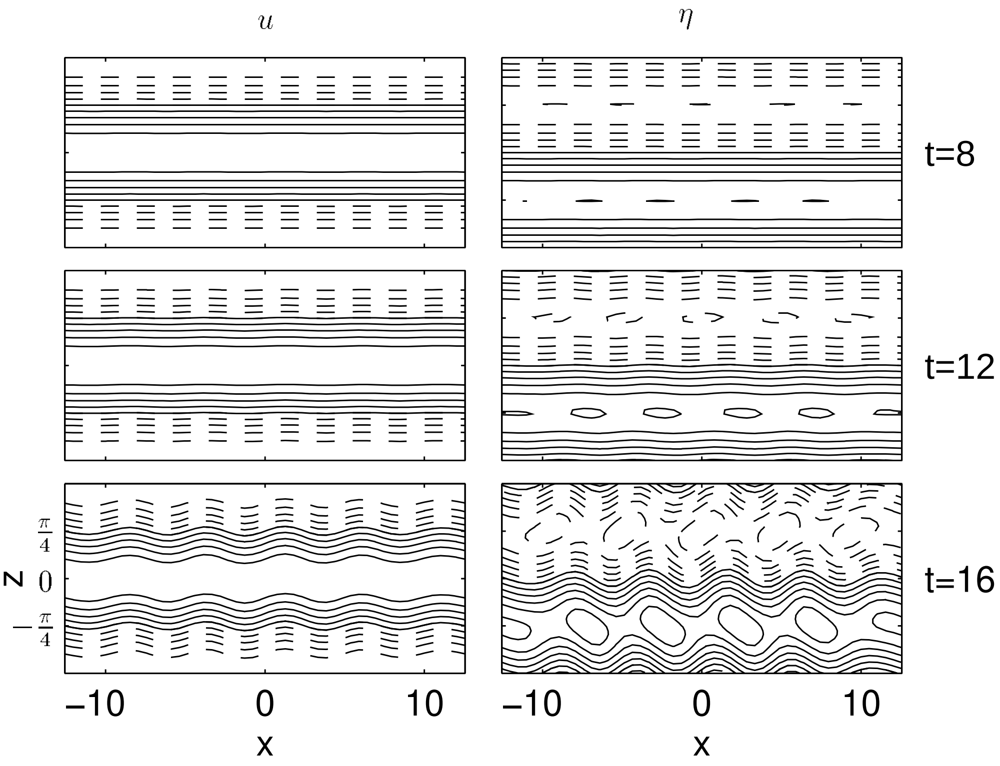

Figure 4.9: Streak "roll up" for the inviscid model problem. The left column shows the evolution of the streamwise velocity u for the inviscid 2D instability associated with (4.3). The initial data is described in the text. The right column shows the evolution of the vertical vorticity η. Note the formation of vertical vortices at the inflection points located at $z = \pm\frac{\pi}{4}$. Shown is the periodic box $8\pi \times \pi$.

The spanwise velocity w is represented as a similar cosine series and the streamwise velocity as a sine series. Waleffe uses a two term truncation to show that the leading eigenvalue, and hence the growth rate, is given approximately by

$$\sigma = \alpha_0 \bar{U} + i\frac{|\alpha_0 S|}{\sqrt{2}} \left(\frac{\beta_0^2 - \alpha_0^2}{\beta_0^2 + \alpha_0^2}\right)^{1/2}. \tag{4.5}$$

The actual leading eigenvalue is qualitatively similar and may be given as a continued fraction [67, 96]. In the approximation (4.5), disturbances with streamwise

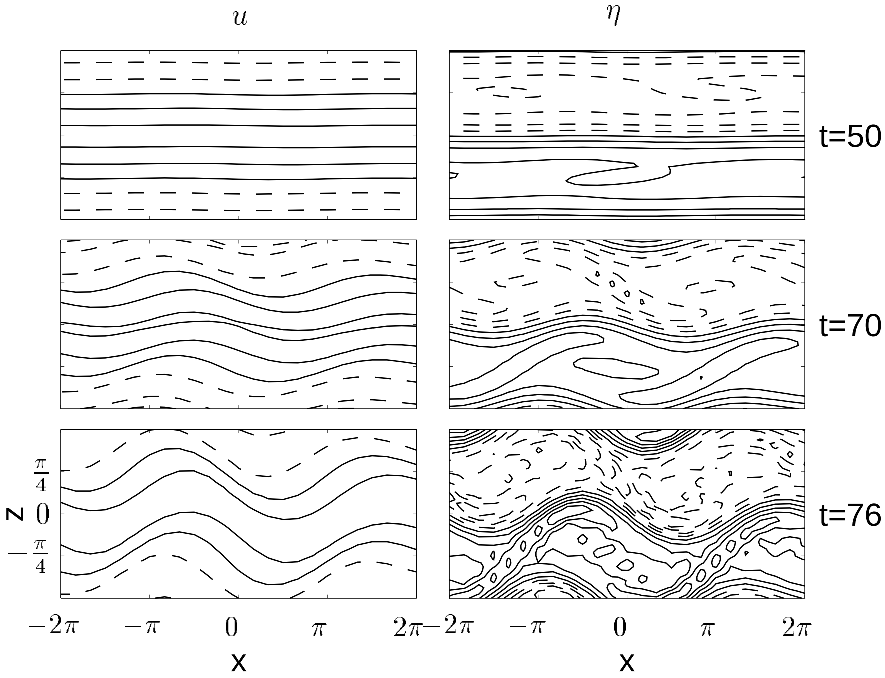

Figure 4.10: "Roll up" of vertical vortices in PCF. The left column shows the evolution of the streamwise velocity u in the x-z-plane at the channel center in PCF, with the same initial data as in Figure 4.1. The right column shows the evolution of the vertical vorticity η. The primary action of the instability is the formation of vertical vortices at the inflection points, $z = \pm\pi/4$, in the streamwise velocity profile.

wave number α_0 less than the fundamental wavenumber β_0 grow exponentially, and those with streamwise wavenumber larger than the β_0 are neutrally stable. The mean flow speed parameter $\bar{U}$ does not change the growth rate of this instability, but we have included it to show how the mean flow can advect the growing disturbance downstream with phase speed $\alpha_0\bar{U}$. We will refer to this again in Section 4.5 when we discuss the phase speeds of the analogous instability in PCF and PPF.

In an actual shear flow, the streamwise streaks are dominated by their streamwise velocity component. The streamwise velocity varies primarily in the spanwise direction, so the streamwise streaks may be thought of as vertical vorticity with little or no streamwise component ($\eta = u_z - w_x \approx u_z$). The action of the streak instability is to make the streamwise streaks wavy. Roughly speaking, this happens through the "roll up" of the vertical vorticity into vertical vortices. To illustrate this instability, we take $\beta_0 = 2$, $\bar{U} = 0$, and $S = 1$ in the inviscid model (4.3) and add noise of amplitude approximately 10^{-5} to the streamwise dependent modes with $\alpha_0 = .25, .5, ..., 1.75$ in a periodic box of dimensions $8\pi \times \pi$. Figure 4.9 shows the evolution of the streamwise velocity u and the vertical vorticity η, where we have used a two mode truncation for each component. Note the vertical vortices forming at the spanwise inflection points of the streamwise velocity, $z = \pm\frac{\pi}{4}$.

Flow visualizations show that the streak instabilities in PCF and PPF are similar to the inviscid instability considered above. Figure 4.10 shows the evolution of the streamwise velocity and the normal vorticity from a full Navier–Stokes simulation of PCF in a periodic box of dimensions $8\pi \times 2 \times \pi$ at $R = 500$ with fundamental spanwise wavenumber $\beta_0 = 2$ (see also Figure 4.4). The initial streamwise vortices are chosen large enough to create linearly unstable streaks, and noise is added to the streamwise dependent modes to break symmetries (the initial data is the same as in Figure 4.1). The wavy streaks are not advected in the streamwise direction in PCF, corresponding to $\bar{U} = 0$ in the inviscid model (4.3).

4.4 Direct numerical simulations of the streak instability

Linearly unstable streamwise streaks, that is, secondarily unstable streamwise vortices, are a necessary condition for reaching turbulence along the path described by (∗). Thus we would like to determine the threshold amplitude of the initial streamwise vortices for generating linearly unstable streamwise streaks. In this section we investigate the dependence of the streak instability growth rate on the initial vortex amplitude via direct numerical simulations of the Navier–Stokes equations. In the next section we continue this investigation using the linear stability analysis of the streamwise streaks developed in [79]. The two analyses are in excellent agreement.

The kinetic energy density of a perturbation (u, v, w) to the laminar flow at time t is given by

$$E(u, v, w, t) = \frac{1}{2V} \int_{\text{period}} (u^2 + v^2 + w^2) d\mathbf{x}, \tag{4.6}$$

where the integration volume is one periodic box with volume V. All simulations are done in a periodic box of dimensions $8\pi \times 2 \times \pi$ with 32, 49, and 32 points in the x, y, and z directions (dealiased by the 3/2 rule). The amplitude of a disturbance is defined as $2\sqrt{E}$. The optimal streamwise vortex defined in (4.1) is normalized so that (u_0, v_0, w_0) has amplitude ϵ. We fix the spanwise wavenumber at $\beta_0 = 2$ since this is near the spanwise wavenumber for maximum transient linear growth in both PCF and PPF [11, 95]. We do not vary β_0 in our study. The dependence of the growth rates on β_0 was studied briefly in [79].

We use the following procedure to investigate the dependence of the streak instability growth rates on the initial vortex amplitudes.

- **Step 1:** Add optimal streamwise vortices of the form (4.1) with amplitude ϵ to the laminar flow at $t = 0$.

- **Step 2:** Integrate the resulting velocity field until time $t_{\max}$, which is the time at which the fundamental streak component $U_1(y,t)\cos\beta_0 z$ has maximum amplitude.

- **Step 3:** A perturbation of the form

$$u_{\text{pert}} = \text{Re}\{e^{i\alpha_0 x} \sum_{k=-15}^{15} e^{ik\beta_0 z} F_k(y)\}, \tag{4.7}$$

  where the $F_k(y)$ are Stokes modes, is added to the streamwise streak velocity field. The amplitude of the perturbation is less than 1% of the streak amplitude. The resulting velocity field is

$$(u(y,z,t_{\max}), v(y,z,t_{\max}), w(y,z,t_{\max})) + u_{\text{pert}}(x,y,z,t).$$

- **Step 4:** Simulate a linear stability analysis by integrating the resulting velocity field while keeping the streamwise independent portion of the field fixed. That is, the Fourier modes with streamwise wavenumber $\alpha = 0$ are frozen at their values in Step 3. We integrate until the amplitude of the $(\alpha_0, k\beta_0)$ modes (the oblique modes with streamwise wavenumber α_0) varies exponentially like $Ce^{\lambda t}$. (The modes for $k = 0, 1, \ldots$ all have the same growth rate. We measure the amplitude of the (α_0, β_0) mode.) We take the growth rate of the streak instability to be λ.

The integrations are performed using the Chebyshev/Fourier Navier–Stokes simulation code of Lundbladh, Henningson, and Johansson [62]. The velocity field in Steps 1-2 is independent of the streamwise coordinate, and thus it is strictly two-dimensional. In Step 3 we add noise to the components of the velocity field with streamwise wavenumber α_0 to investigate the exponential growth of oblique waves. In a full channel flow simulation, transition to turbulence cannot occur from a strictly two-dimensional velocity field like the one in Steps 1–2. The velocity field would simply decay slowly due to viscous effects. So one can consider the noise added in Step 3 as necessary to break the symmetry associated with a streamwise independent velocity field. In Step 4 we artificially freeze the streamwise independent portion of the velocity field, that is, the streamwise streaks are frozen at the time when the fundamental streak component U_1 would attain its maximum amplitude if the velocity field were strictly two-dimensional. Since the streamwise independent parts of the velocity field are not allowed to evolve in Step 4, this technique is nearly equivalent to linearizing about the velocity field at time $t_{\max}$. It is not completely equivalent to a linear stability analysis because the streamwise dependent modes ($\alpha_0 \neq 0$) are still allowed to evolve nonlinearly to generate higher harmonics (for example, modes with streamwise wavenumber $2\alpha_0$), but these interactions are quadratic in the disturbance amplitude and should be negligible over the range of amplitudes we consider. In the cases when there is no streak ($\epsilon = 0$), noise of amplitude approximately 10^{-6} is added to the α_0 modes at $t = 0$ and the resulting velocity field integrated until the amplitude of the noise in the (α_0, β_0) mode decays exponentially.

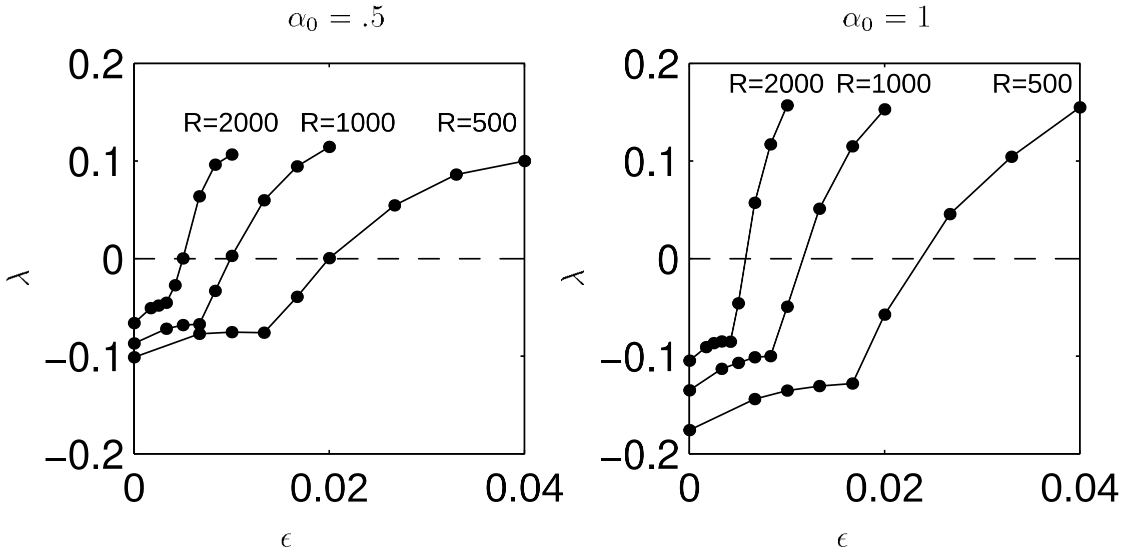

Figure 4.11: Growth rate λ of the streak instability versus initial vortex amplitude ϵ for PCF based on full Navier–Stokes simulations. The left plot is for $\alpha_0 = .5$ and the right plot for $\alpha_0 = 1$. The threshold amplitude for streak instability scales as $\approx C_c(\alpha_0)R^{-1}$.

Figure 4.11 shows the growth rate λ of the streak instability as a function of the initial vortex amplitude ϵ in PCF for $R = 500, 1000$, and 2000. The left plot is for $\alpha_0 = .5$ and the right plot is for $\alpha_0 = 1$. In both cases the amplitude for neutral stability of the oblique modes scales approximately as $C_c(\alpha_0)R^{-1}$. An interesting feature of the growth rate curves is the discontinuity in the slope which occurs at subcritical amplitudes. Relatedly, the $\epsilon = 0$ intercepts in these growth rate curves scale approximately as $R^{-.31}$ and $R^{-.37}$ for $\alpha_0 = .5$ and $\alpha_0 = 1$, respectively. We note, that as the wavy streaks develop from this instability, the wave crests do not move in the streamwise direction; see Figure 4.10. That is, the exponentially growing waves are standing waves with zero phase speed. We discuss the phase

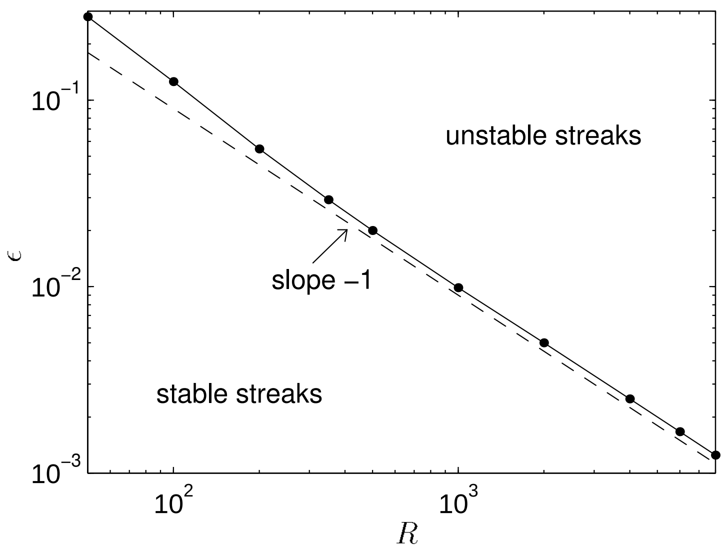

Figure 4.12: Neutral stability curve for streamwise streaks in PCF with $\alpha_0 = 0.5$ and initial streamwise vortices of amplitude ϵ. The streaks are frozen at time $t_{\max}$. They can be unstable for R at least as low as 50.

speeds and the characteristics of these growth rate curves, particularly the slope discontinuity, in Section 4.7.

We have done simulations for $R \in [50, 8000]$ to verify the threshold amplitude scaling. Figure 4.12 shows the neutral stability curve of the streamwise streaks with $\alpha_0 = .5$ and initial streamwise vortices of amplitude ϵ with the streaks frozen at time $t_{\max}$. The figure shows that the threshold amplitude scales as R^{-1} for large R. We will explain this scaling in Section 4.7. However, this scaling does not hold for small R, indicating that the actual threshold amplitude probably contains other factors. Streamwise vortices in PCF generate linearly unstable streaks for R well below the lowest Reynolds numbers at which turbulence is first observed ($R \approx 280$; see our discussion on page 3 of this thesis) confirming that linearly unstable streaks

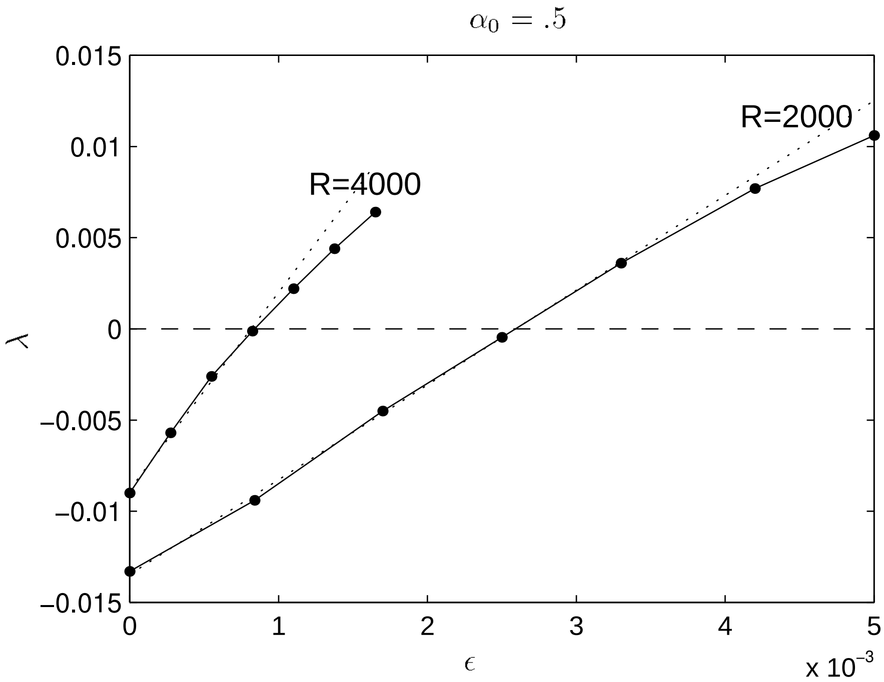

Figure 4.13: Growth rate λ of the streak instability versus initial vortex amplitude ϵ for PPF with $\alpha_0 = .5$ based on full Navier–Stokes simulations. The threshold amplitude for instability scales as $\approx C_p(\alpha_0)R^{-1.6}$. The dotted lines are the linear least squares fit to the first four data points on each curve. The growth rate increases approximately linearly with increasing vortex amplitudes for amplitudes below the threshold.

are a necessary but not sufficient condition for transition to occur as in $(*)$.

We should note that we have not optimized over time in computing these neutral stability results. We "linearize" about the streamwise streaks at time $t_{\max}$ as defined above. However, the threshold amplitudes for neutral stability might be slightly lower at other times. Since streamwise vortices of amplitude $O(R^{-1})$ generate streamwise streaks of amplitude $O(1)$, the development of the streak components U_k in (4.2) is affected by strongly nonlinear processes. Thus, there is no straightforward way to compute the smallest threshold amplitude for a streamwise

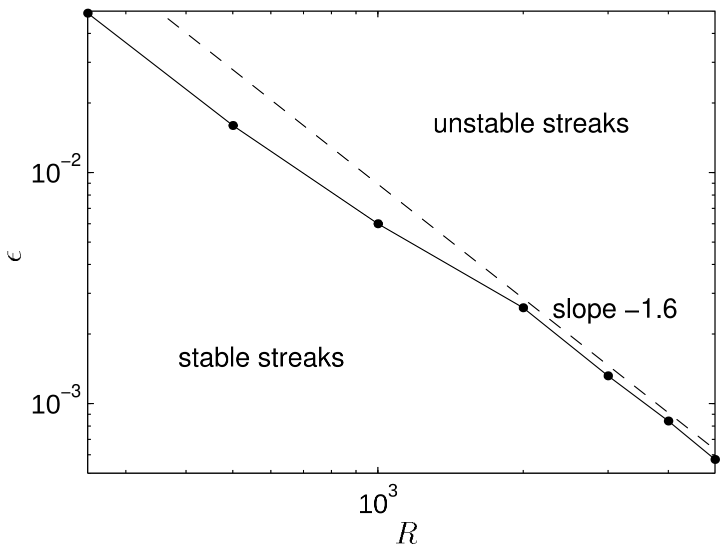

Figure 4.14: Neutral stability curve for streamwise streaks in PPF with $\alpha_0 = 0.5$ and initial odd streamwise vortices of amplitude ϵ. The streaks are frozen at time $t_{\max}$. They can be unstable for R at least as low as 250.

vortex except to optimize over time, but we have not undertaken this computationally intensive task. Strictly speaking, one should also optimize over α_0 and β_0 to find the lowest possible threshold amplitudes. However, in this chapter, our goal is not to compute minimum threshold amplitudes, but to explain their different scalings. Reddy, Schmid, and Baggett [79] optimized over time and over the streamwise wavenumber α_0 in their computations of the the threshold scalings via a linear stability analysis which we review in the next section (they also briefly discuss the dependence of the growth rates on the spanwise wavenumber β_0).

Figure 4.13 shows the results for PPF at $R = 2000$ and 4000 with $\alpha_0 = .5$. The threshold amplitude for neutral stability of the oblique modes scales approximately as $C_p(\alpha_0)R^{-1.6}$. In contrast to PCF, the growth rate increases approximately linearly with increasing initial vortex amplitude, at least for small amplitudes below the threshold. The $\epsilon = 0$ intercepts scale approximately as $R^{-.56}$. In contrast to PCF, the wavy streaks are advected downstream as they grow. We discuss their phase speeds and the growth rate curves in Section 4.6.

Figure 4.14 shows the neutral stability curve for the streak instability with $\alpha_0 = .5$ and $R \in [250, 5000]$. For $R \gtrapprox 2000$ the threshold amplitude scales as approximately $C_p(\alpha_0)R^{-1.6}$. Again, the streaks are linearly unstable well below the lowest Reynolds numbers at which turbulence is observed. We will discuss these threshold scalings in Section 4.6.

4.5 Linear stability analysis of the streak instability*

In this section we compare the neutral stability results of the last section to those of Reddy, Schmid, and Baggett [79], who employ a linear stability analysis to determine the growth rates of the streak instability. In particular, they determine that the threshold amplitudes of the initial streamwise vortices for generating linearly unstable streaks (optimized over time and streamwise wavenumber α_0) scale approximately as $C_1 R^{-1}$ and $C_2 R^{-1.6}$ in PCF and PPF, respectively. Waleffe [97] also studied streak breakdown in PCF using a similar linear stability analysis. In both [79] and [97], the Navier–Stokes equations are linearized about the basic flow $\mathbf{U} = (U(y,z,t), 0, 0)$, where $U(y,z,t)$ is given by (4.2) and is obtained from a direct

*Parts of this section are adapted from [79].

numerical simulation. (Note that the small spanwise and vertical components of the streamwise streaks have been discarded, in contrast to the technique we applied in the previous section.) The linear equations governing the evolution of a small perturbation (u, v, w) to $\mathbf{U}$ are

$$\begin{aligned} u_x + v_y + w_z &= 0, \\ u_t + Uu_x + U_y v + U_z w &= -p_x + \frac{1}{R}\Delta u, \\ v_t + Uv_x &= -p_y + \frac{1}{R}\Delta v, \\ w_t + Uw_x &= -p_z + \frac{1}{R}\Delta w, \end{aligned} \tag{4.8}$$

where $p = p(x, y, z, t)$ is the perturbation of the pressure. Equations (4.8) may be reduced to two equations in terms of the perturbation normal velocity v and normal vorticity $\eta = u_z - w_x$. The manipulations are similar to those used to derive the Squire and Orr-Sommerfeld equations[3]:

$$\begin{aligned} \eta_t + U\eta_x - U_z v_y + U_{yz} v + U_y v_z + U_{zz} w &= \frac{1}{R}\Delta\eta, \\ \Delta v_t + U\Delta v_x + U_{zz} v_x + 2U_z v_{xz} - U_{yy} v_x - 2U_z w_{xy} - 2U_{yz} w_x &= \frac{1}{R}\Delta\Delta v, \end{aligned} \tag{4.9}$$

with boundary conditions $v(y = \pm 1) = v_y(y = \pm 1) = \eta(y = \pm 1) = 0$. The spanwise velocity w can be eliminated by using the identity $w_{xx} + w_{zz} = -\eta_x - v_{yz}$. The perturbation normal velocity and normal vorticity are assumed to have the form

$$\begin{aligned} v(x, y, z, t) &= \mathrm{Re}\{e^{i(\alpha_0 x - \sigma t)} \sum_{k=-m}^{m} v_k(y) e^{ik\beta_0 z}\}, \\ \eta(x, y, z, t) &= \mathrm{Re}\{e^{i(\alpha_0 x - \sigma t)} \sum_{k=-m}^{m} \eta_k(y) e^{ik\beta_0 z}\}. \end{aligned} \tag{4.10}$$

[3] In fact, the equations (4.9) are the Squire and Orr-Sommerfeld equations if U is the laminar solution.

The functions U_k in the streak expansion (4.2) have zero phase in all of our simulations. Thus the perturbation expansion may be divided into sinuous (v and η are odd and even functions of z, respectively) and varicose modes as in the inviscid, two-dimensional example in Section 4.2. An eigenvalue problem for the eigenvalue $\sigma = \sigma_r + i\sigma_i$ and the eigenfunctions $v_k(y)$ and $\eta_k(y)$ is obtained by substituting (4.10) into (4.9) and collecting terms with like powers of $e^{i\beta_0 z}$. The number of terms m is increased until the successive approximations to σ differ by less than 0.5%. For further details see [79].

Figure 4.15 shows the growth rate σ_i versus the initial vortex amplitude ϵ in PCF for $R = 500$ and $\alpha_0 = 1$, as computed by the linear stability analysis. The streak profile is $U(y, z, t_{\max})$, where $t_{\max}$ is as in the previous section. For amplitudes below the slope discontinuity the phase speed is $\sigma_r \approx 0.7\alpha_0$ and above the discontinuity it is $\sigma_r = 0$. We have found that $\sigma_r = 0$ for all of the linearly unstable streaks we have examined in PCF.

Unlike the method used in the previous section, the linear stability analysis allows us to modify or omit selected streak components $U_k(y)$ to study how the individual components of the streak affect the streak instability. The plot in Figure 4.15 shows that there is little change in the growth rates if $U_k = 0$ for $k \geq 2$. This suggests that only the modified mean flow $U_0(y, t)$ and the fundamental streak component $U_1(y, t) \cos \beta_0 z$ are important in determining the character of the instability, at least for this choice of parameters. Reddy has pointed out (private communication) that more streak components are required to obtain accurate growth rates for higher values of α_0. However, as we will see in the next section, U_0 and U_1 suffice

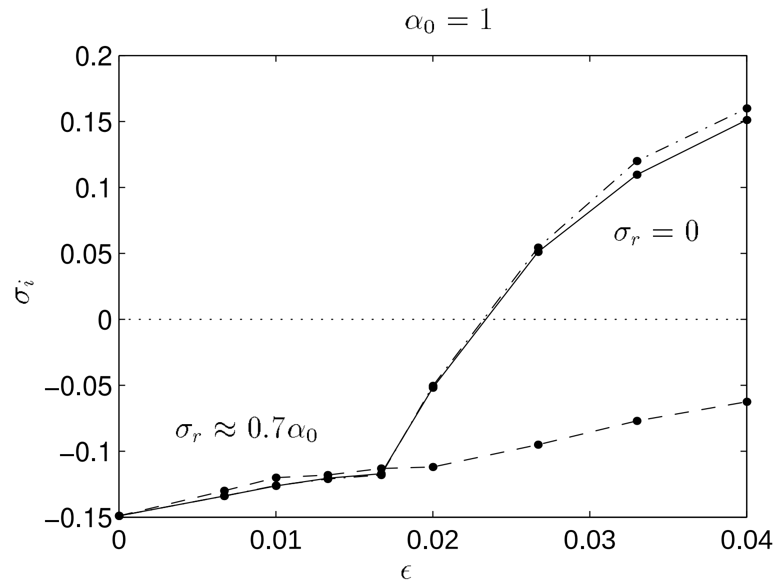

Figure 4.15: Streak instability growth rate σ_i versus initial vortex amplitude ϵ in PCF with $R = 500$ and $\alpha_0 = 1$ as computed by linear stability analysis. The solid line shows the converged growth rate including $U_0, \ldots, U_7$ in the streak expansion. The dash-dot line shows the growth rate with only U_0 and U_1 included indicating that these are the important components of the streak. The dashed line shows the growth rate with the laminar mean profile artificially restored, that is, $U_0 = y$, and $U_1, \ldots, U_7$ are as computed by the simulation, indicating that the laminar shear stabilizes the streaks. Below the slope discontinuity the phase speed is $\sigma_r \approx 0.7\alpha_0$, while it is zero above it.

to explain the R^{-1} scaling of the initial streamwise vortices.

Also shown in Figure 4.15 are the growth rates obtained when the mean flow is artificially reset to the laminar profile, that is, $U_0(y,t) = y$. In this case, the streamwise streaks are stable over the range of initial vortex amplitudes considered. This suggests that the laminar uniform shear profile must be modified before the streaks can be linearly unstable. In other words, the shear has a stabilizing influence on the streaks. In Section 4.7 we introduce a model problem to elucidate the role

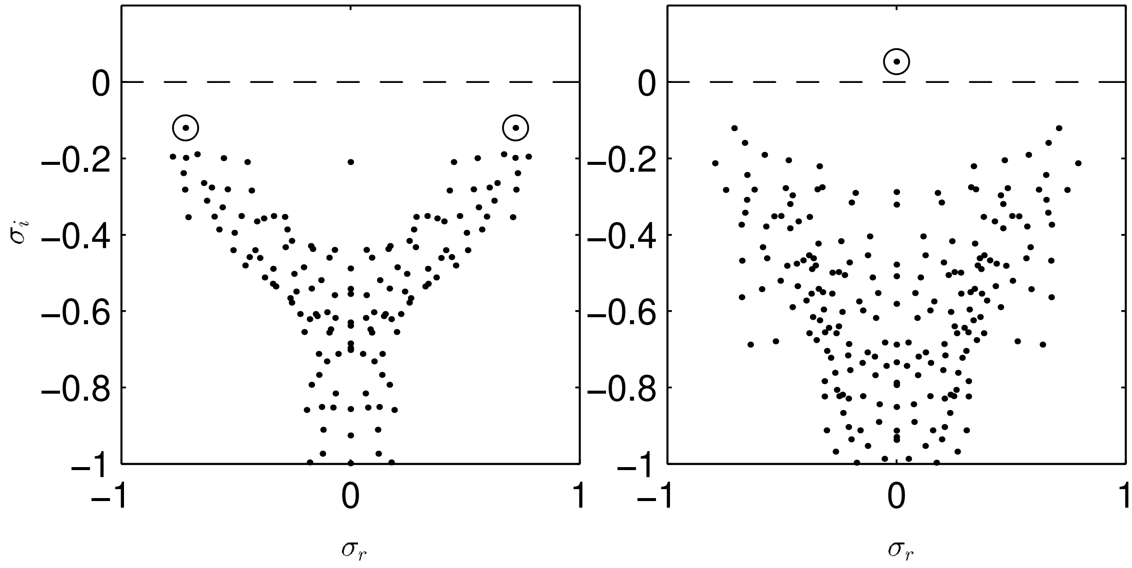

Figure 4.16: Spectra of the streak instability operator in PCF with $R = 500$ and $\alpha_0 = 1$. The left plot corresponds to streaks generated from an optimal vortices of amplitude $\epsilon = 0.013$ (the fourth smallest amplitude on the solid curve in Figure 4.15) at time $t_{\max} \approx 57$. The right plot corresponds to streaks generated from vortices of amplitude $\epsilon = 0.027$ (the seventh smallest amplitude) at time $t_{\max} \approx 49$. There are circles around the least stable eigenvalues. For small initial vortex amplitudes "wall" modes are the least stable, but for larger initial amplitudes, a single mode with zero phase speed becomes unstable.

of the vertical shear in the streak instability in PCF.

The plots in figure 4.16 show the spectra of the linear operator which governs the evolution of small perturbations to the streaks (implicitly defined by (4.9)) in PCF with $R = 500$ and $\alpha_0 = 1$. The left plot corresponds to a stable streak ($\epsilon = 0.0133$) and the right plot to an unstable streak ($\epsilon = 0.0267$). For small initial vortex amplitudes, the least stable modes have phase speeds which increase towards α_0 as R increases. This, and the fact that their dissipation rates scale approximately as $R^{-1/3}$, indicate that these modes are related to the least stable

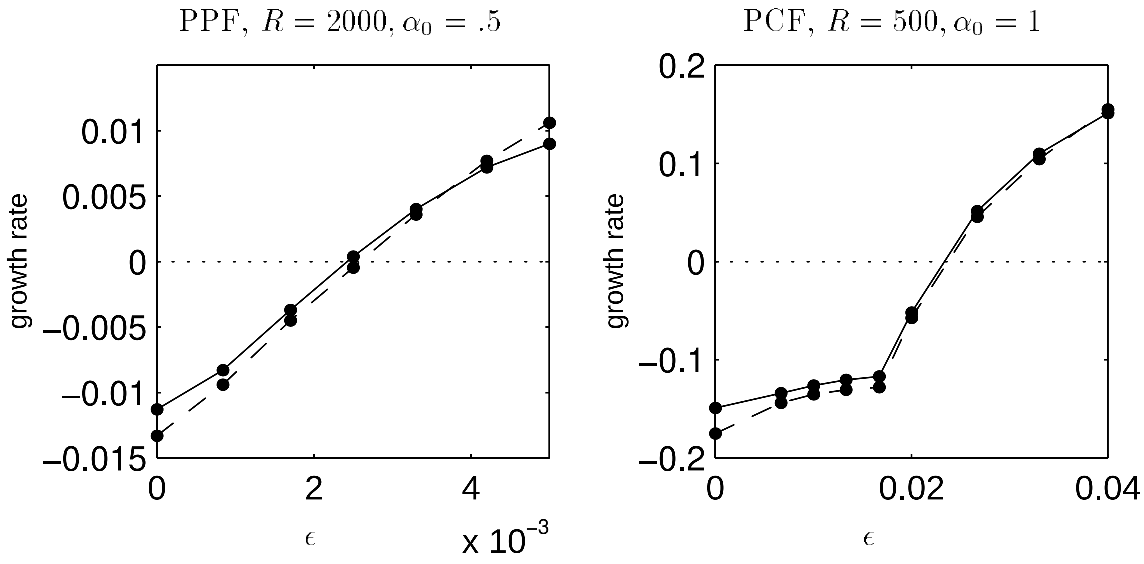

Figure 4.17: Comparison of streak instability growth rates as computed by direct numerical simulation (dashed lines) and linear stability analysis (solid). The left plot is for PPF with $R = 2000$ and $\alpha_0 = .5$ and the right plot for PCF with $R = 500$ and $\alpha_0 = 1$.

modes of the Orr-Sommerfeld/Squire (hereafter OSS) operator governing the evolution of perturbations to the laminar flow in PCF. The least stable OSS modes have dissipation rates which scale as $R^{-1/3}$ and phase speeds which approach α_0 for large R and $\alpha_0 \neq 0$. They are known as "wall" modes because they tend to be localized near the walls and are advected in the direction of the moving wall. See [22] for further details on the OSS modes.

The left plot in Figure 4.18 shows the $\eta_0(y)$ component of the vertical vorticity of the eigenfunction corresponding to the unstable eigenvalue in Figure 4.16. The plot also shows the modified mean flow component of the streak $U_0(y, t_{\max})$, which is somewhat flattened near the channel center. This plot gives an indication that

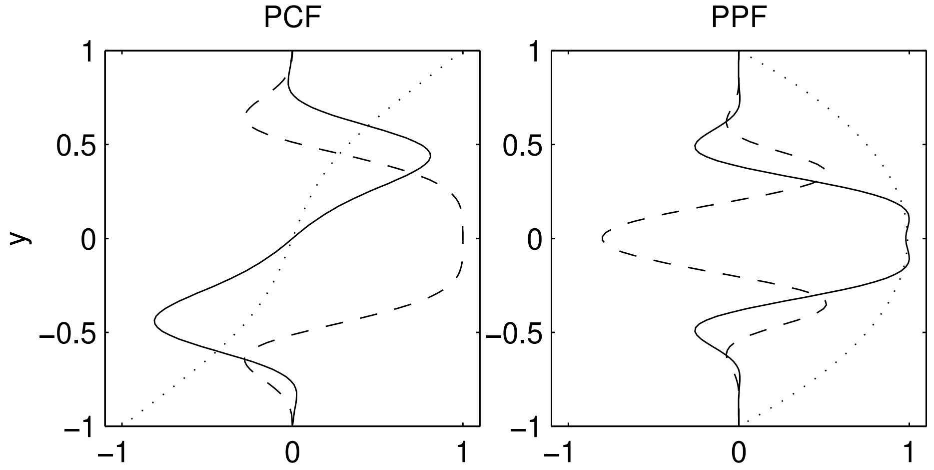

Figure 4.18: The $\eta_0(y)$ component of the unstable streak instability mode. The left plot is for PCF, corresponding to the unstable eigenvalue in Figure 4.16. The right plot is for PPF, corresponding to the unstable eigenvalue in Figure 4.19. The solid curves and dashed curves are the real and imaginary parts of $\eta_0(y)$, respectively. Also shown are the mean flow components of the streak $U_0(y, t_{\max})$ (dotted). Note that the largest parts of $\eta_0(y)$ occur approximately localized in the regions of least vertical shear.

most of the action of the streak instability is near the center of the channel where, the shear has been reduced. We will see that this is indeed the case in Section 4.7.

The solid line in the left plot of Figure 4.17 shows the growth rate σ_i versus ϵ as computed by the linear stability analysis for PPF with $R = 2000$ and $\alpha_0 = 0.5$. The phase speed is $\sigma_r \approx 0.475$ near the threshold amplitudes. The growth rates are computed in the linear stability analysis using the streak components $U_1, \ldots, U_7$ at time $t_{\max}$ from a full numerical simulation. However, the curve does not change visibly if only the U_0 and U_1 components are included or if U_0 is replaced by the laminar profile $U_0(y) = 1 - y^2$. Thus, as in PCF, only the streak components U_0 and U_1 are important in determining the character of the instability (at least for

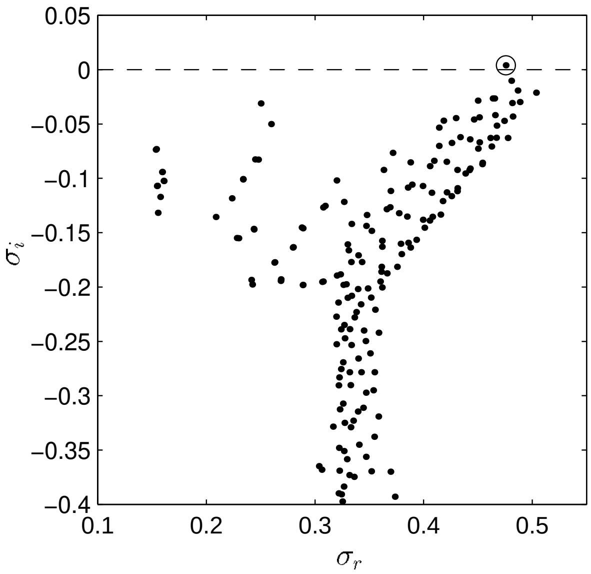

Figure 4.19: Spectrum of the streak instability operator in PPF with $R = 2000$ and $\alpha_0 = 0.5$. The streak is generated from streamwise vortices of amplitude $\epsilon = 0.0033$ (the fifth largest amplitude in the left plot of Figure 4.17) at time $t_{\max} \approx 133$. The unstable eigenvalue is circled and the corresponding mode has phase speed $\approx 0.95\alpha_0 = 0.475$.

this combination of parameters). However, in contrast to the situation with PCF, the modification of the laminar flow has little effect on the growth rates in PPF.

Figure 4.19 shows a plot of the spectrum of the streak instability operator in PPF with $R = 2000$ and $\alpha_0 = .5$ for a slightly unstable streak ($\epsilon = 0.0033$). The $\eta_0(y)$ component of the eigenfunction corresponding to the unstable eigenvalue is shown in the right plot of Figure 4.18. The components of the eigenfunction all tend to be localized near the channel center indicating that most of the action of the streak instability, at least near the threshold amplitudes, is near the center of the channel in the region of least vertical shear. For small initial vortex amplitudes, even slightly above the threshold values, the least stable or unstable modes of the streak instability operator have phase speeds approaching α_0. Moreover, these modes are localized in the center of the channel. This suggests that these modes are related to the so called "center modes" of the OSS operator for PPF which belong to the "P-family." See [22] for further details on the OSS operator and its different families of eigenmodes in PPF.

Figure 4.17 compares the growth rates as computed by the linear stability analysis to those computed by numerical simulations. In general, the agreement is excellent. The source of the slight differences is that the small spanwise and vertical velocity components of the streamwise streaks are omitted in the linear stability analysis, while these components are included in the Navier–Stokes simulations of the previous section.

In the next two sections we further discuss the streak instability and give explanations for the different threshold amplitude scalings we have observed in PPF and PCF.

4.6 The threshold scaling in plane Poiseuille flow

Figure 4.13 indicates that the growth rates depend approximately linearly on the initial vortex amplitudes in PPF, at least for amplitudes below the threshold. For a fixed streamwise wavenumber α_0, over the relevant range of vortex amplitudes, the growth rate is given approximately by

$$\lambda \approx \sigma_i \approx -D(R) + C\epsilon R, \tag{4.11}$$

where ϵ is the vortex amplitude, C is a positive constant, and $D(R)$ corresponds to viscous dissipation (that is, the rate at which noise decays in the modes with streamwise wavenumber α_0 in the presence of the laminar PPF flow). The $C\epsilon R$ term represents the amplitude of the streaks. As mentioned in the previous section, the intercepts of the the growth rate curves with the $\epsilon = 0$ axis in Figure 4.13 (as computed by numerical simulations) scale approximately as $-C'R^{-.56}$ ($\alpha_0 = 0.5$ in that figure). Thus for $\alpha_0 = 0.5$ we have a value of $D(R) \approx C'R^{-.56}$. So by the approximation (4.11), the threshold amplitude for initial streamwise vortices which generate a streak instability (with $\alpha_0 = 0.5$) scales approximately as $R^{-1.56}$ (ignoring the constants) in reasonably good agreement with our observed neutral stability scaling of approximately $C_p(\alpha_0)R^{-1.6}$.

The decay rates at $\epsilon = 0$ should be determined by the equations governing the evolution of infinitesimal disturbances to the laminar flow. We have computed these dissipation rates numerically from the OSS operator for PPF (using a Chebyshev spectral discretization). For Reynolds numbers $R \in [1000, 6000]$ the growth rate for the least stable sinuous mode, with $\alpha_0 = 0.5$, satisfies $D(R) \approx C''R^{-.55}$, where C'' is a constant. By the approximation (4.11), we would expect a threshold amplitude scaling with R-dependence $R^{-1.55}$, again in reasonably good agreement with our observed scaling.

Thus, in PPF, the streamwise streaks become linearly unstable when they are large enough to overcome the effects of viscous dissipation. Importantly, no nonlinear modification of the laminar profile $(1-y^2)$ is required because the profile already has a region of negligible shear near the channel center in which vertical vortices can form (the mean flow component $U_0(y)$ of a slightly unstable streak is virtually indistinguishable from the laminar profile; see the right plot in Figure 4.18). This is not to say that the vertical shear plays no role in the threshold amplitude scalings. The parabolic laminar profile, with its curving shear at the channel center, is what makes the viscous dissipation rates $D(R)$ affecting the streak instability scale approximately as $R^{-.55}$ (over the range of R we considered) instead of R^{-1}, which is the expected scaling in the absence of any background flow. However, the laminar profile is perfectly suitable for the streak instability.

The phase speeds of the streak instability modes for initial vortex amplitudes near the threshold are approximately determined by the centerline speed of the laminar flow. Perhaps this is not surprising, given that the streak instability occurs in regions near the channel center and the vertical vortices, or wavy streaks, are transported downstream with the mean flow in that region. As in the inviscid model (4.3) (with $\bar{U} \approx 1$), the exponentially growing oblique waves are advected downstream with phase speed approximately α_0.

As we will see in the next section, the situation in PCF is much different.

4.7 The threshold scaling in plane Couette flow

Because of the discontinuity in the slopes of the growth rate versus initial vortex amplitude curves, there is no clear relationship, not even approximate, between the growth rate and the initial vortex amplitude in PCF. As we mentioned above, the least stable modes in laminar PCF have dissipation rates which scale as $R^{-1/3}$ for large R and nonzero α_0. However these modes are localized near the walls and have little to do with the streak instability, which happens in the channel interior.

An important clue to understanding the streak instability in PCF is indicated in Figure 4.15. If the mean flow component of the streaks $U_0(y)$ is replaced by the laminar PCF solution $U_0(y) = y$, then the streaks are stabilized. As we mentioned in Section 4.5, this indicates that the shear has a stabilizing influence on the streaks and that the modification of the mean flow, that is, the reduction of the shear at the channel center, is essential for the streak instability.

The streak components U_0 and U_1 dominate the character of the streak instability (at least over the range of parameters we have explored). We observed that streamwise vortices of amplitude $O(R^{-1})$ are necessary to generate linearly unstable streaks and even to cause transition to turbulence as described by $(*)$. Streamwise vortices of amplitude $O(R^{-1})$ generate streamwise streaks of amplitude $O(1)$ via the shear-tilting mechanism described in Section 4.2. At $O(1)$ amplitudes, the components of the streak U_k are affected by strongly nonlinear processes. Even for the fixed initial streamwise vortex profile we consider, the shapes of U_0 and U_1 cannot be easily determined except by a full numerical simulation.

In this section we develop a two-parameter model of the streamwise streaks in PCF. This model allows us to study the relationship between the streak instability and the vertical shear. We also use it to explain the $O(R^{-1})$ threshold amplitude scaling of the initial vortices. To develop this model, we model the streak profile $U_1(y)$ and the modified mean flow profile $U_m(y) = U_0(y) - y$ from an actual simulation. Once the model profiles are fixed, their amplitudes may be varied independently so that we may independently study the effects of flattening the mean flow profile (reducing the shear) or increasing the spanwise variation of the flow at the inflection points.

We assume the velocity field has the form:

$$\begin{aligned}
U(x,y,z,t) &= y + U_m(y,t) + U_1(y,t)\cos(\beta_0 z) \\
&= U_0(y,t) + U_1(y,t)\cos(\beta_0 z), \\
V(x,y,z,t) &= V_1(y,t)\cos(\beta_0 z), \\
W(x,y,z,t) &= W_0(y,t) + W_1(y,t)\sin(\beta_0 z), \\
P(x,y,z,t) &= P_L(x) + P_0(y,t) + P_1(y,t)\cos(\beta_0 z).
\end{aligned} \tag{4.12}$$

The above expressions are truncated versions of the expansions used in the direct numerical simulations in Section 4.4, and all quantities are real. P_L corresponds to the laminar pressure. By continuity, $V_0 = 0$ and $W_1 = -(1/\beta_0)\partial V_1/\partial y$. Substituting (4.12) into the Navier–Stokes equations and writing the result as a truncated Fourier series yields the following equation for U_m :

$$\begin{aligned}
\frac{\partial U_m}{\partial t} &= -\frac{1}{2}V_1\frac{\partial U_1}{\partial y} + \frac{\beta_0}{2}W_1U_1 + \frac{1}{R}\frac{\partial^2 U_m}{\partial y^2} \\
&= -\frac{1}{2}V_1\frac{\partial U_1}{\partial y} - \frac{1}{2}\frac{\partial V_1}{\partial y}U_1 + \frac{1}{R}\frac{\partial^2 U_m}{\partial y^2} \\
&= -\frac{1}{2}\frac{\partial}{\partial y}(U_1V_1) + \frac{1}{R}\frac{\partial^2 U_m}{\partial y^2}.
\end{aligned} \tag{4.13}$$

Thus the primary force acting to modify the mean flow is the Reynolds stress, which arises from the nonlinear interaction of the fundamental U_1 component of the streamwise streaks and the vertical velocity component V_1 of the streamwise vortices.

We proceed by making assumptions about the shapes of the fundamental streak component U_1 and the optimal streamwise vortex profile V_1. We suppose that $U_1(y,t) \sim (1-y^2)$ and that $V_1(y,t) \sim (1-y^2)^2$. In this case, (4.13) shows that $U_m \sim -y(1-y^2)^2$ (we have omitted the small viscous term). Figure 4.20 compares the model profiles to the profiles from a direct numerical simulation in PCF with $R = 500$ and $\beta_0 = 2$. The figure does not show V_1, but the agreement with the model profile is even better than the ones pictured. In the figure, the amplitude of the model profile U_m is chosen so that $dU_m/dy(0,t)$ agrees with the simulation, and the profile U_1 is normalized such that $U_1(0,t)$ agrees with the simulation. We assume that the shapes of U_0 and U_1 are constant and that only their amplitudes change. Thus we consider the following model for the streamwise velocity component of the streamwise streaks in PCF:

$$\begin{aligned} U(y,z,t) &= U_0(y,t) + U_1(y,t)\cos\beta_0 z \\ &= y + U_m(y,t) + U_1(y,t)\cos\beta_0 z \\ &= y + (A-1)y(1-y^2)^2 + B(1-y^2)\cos\beta_0 z \\ &= Ay + (A-1)(-2y^3+y^5) + B(1-y^2)\cos\beta_0 z. \end{aligned} \tag{4.14}$$

The real parameter A governs the amount of shearing by the mean flow in the sense that $dU_0/dy(0) = A$. If $A = 1$, the model mean flow corresponds to the laminar flow. If $A = 0$, then the shear at the channel center is zero, corresponding to the mean flow having been flattened by the action of Reynolds stress. The real parameter B governs the amplitude of the streamwise streaks. We can assume $B > 0$ since the sign of B does not affect the growth rates.

Now that we have a model of the streamwise velocity component of the streamwise streaks, we may apply the linear stability analysis of the previous section.

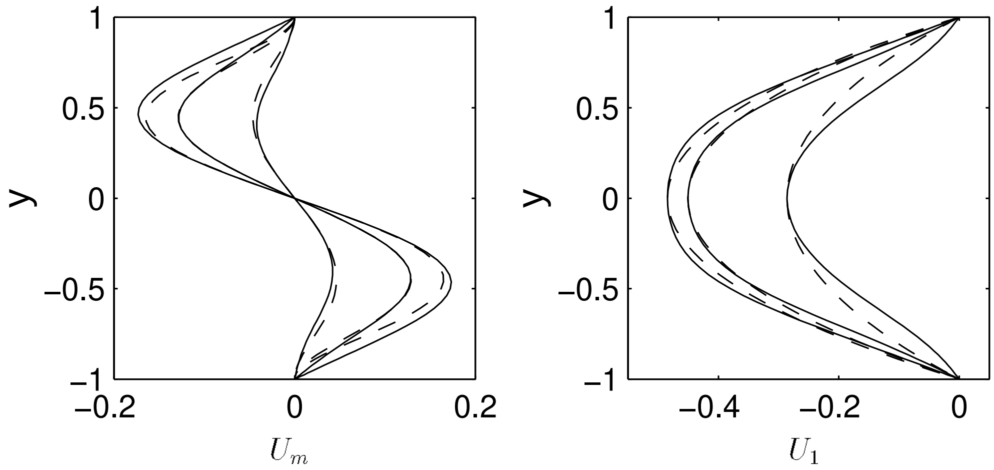

Figure 4.20: Comparison of streak profiles from a Navier–Stokes simulation in PCF and the streak model (4.14). The dashed lines represent the model, and the solid lines are from a simulation of PCF with $R = 500$, $\beta_0 = 2$, and initial vortex amplitude $\epsilon = .0267$ (slightly above neutrality; the same initial data as in Figure 4.1). The left plot shows the modified mean flow $U_m(y,t) = U_0(y,t) - y$ and the right plot shows $U_1(y,t)$ at both $t = 12, 30$ and $t = t_{\max} \approx 49$.

While this model may seem ad hoc, it does an excellent job of predicting the neutral stability of the streamwise streaks. Figure 4.21 shows the neutral stability curves in the A-B-plane for $R = 500, 1000, 2000$ with $\alpha_0 = 1$ as computed by the linear stability analysis. Also shown are measurements of $dU_0/dy(0, t_{\max})$ and $\max_y |U_1(y, t_{\max})|$ from actual simulations with initial vortex amplitudes above and below the threshold amplitude for linearly unstable streaks. As the figure shows, the neutral stability curve generated by the model (4.14) accurately predicts the size of the mean flow modification and streak amplitude necessary for the streaks to be linearly unstable. The neutral stability curve in the A-B-plane is $O(1)$ away from the point $(A, B) = (1, 0)$ which corresponds to the laminar flow. This indicates that

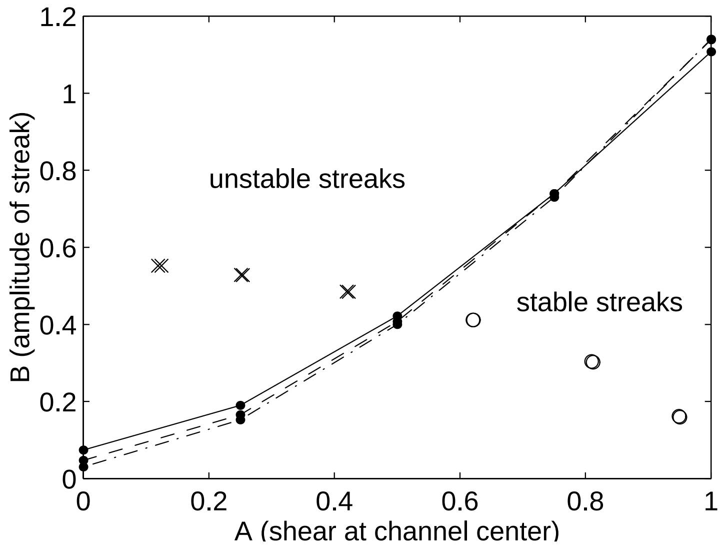

Figure 4.21: Curves of neutral stability in the A-B-plane for the model (4.14) of streamwise streaks in PCF with $\alpha_0 = 1$. The three curves from bottom to top at $A = 0$ correspond to $R = 2000,\ 1000,\ 500$. The circles and crosses are measurements of $\partial U_0/\partial y(0, t_{\max})$ (abscissa) and $|U_1(0, t_{\max})|$ (ordinate) from actual simulations. The streaks are the same ones we "linearized" about in Figure 4.11 corresponding to the six points of largest amplitude on each curve in the right plot. There are three circles or three crosses in each position which correspond to three actual streaks generated from vortices of amplitude ϵ, $\epsilon/2$, $\epsilon/4$ for $R = 500,\ 1000,\ 2000$, respectively.

both U_m and U_1 must have amplitude $O(1)$ for the streaks to be linearly unstable. We offer the following physical interpretation.

Most of the action of the streak instability is near the channel center, where the mean shear profile has been reduced by the action of the Reynolds stress created by the nonlinear interaction of the streaks and vortices; see Figures 4.4 and 4.18. The mean flow is just beginning to develop small shear layers near the walls and a region of low streamwise velocity in the interior of the channel which is largely inviscid in nature. In the interior region, the streaks in our model are of size B and the shear is approximately A. For the streaks to be linearly unstable the time scale t_r for the "roll-up" of the vertical vorticity into vertical vortices must be shorter than the time scale t_s over which the vertical vortices are "sheared out" by the mean shear, that is, $t_r < t_s$ is necessary for unstable streaks. Given that the mean flow is flattening, so that the interior of the flow does not feel the viscous effects produced at the walls, we can expect the inviscid model problem (4.3) to roughly approximate the conditions in the interior of the flow. Thus the time scale for "roll up" follows from the inviscid instability growth rate (4.5), with $S = B$ and $\bar{U} = 0$, and is given approximately by $t_r = C_1(\alpha_0 B)^{-1}$, where C_1 is an $O(1)$ constant. The time scale for shearing (near the channel center) is approximately $t_s(\alpha_0 A)^{-1}$. Thus, the condition $t_r < t_s$ becomes $A < B(C_1)^{-1}$. In other words, the streaks have to be of size $O(1)$ and/or the shear has to be significantly reduced for the streaks to be linear unstable. The neutral stability curves for our model problem in Figure 4.21 indicate that both effects occur. In PCF, the streaks and the reduction of the shear both have to be $O(1)$ (independent of R) for streak instability. The only way this can be achieved along the path to turbulence $(*)$ is to start with streamwise vortices of amplitude $O(R^{-1})$. (It is a standard argument to show that $O(R^{-1})$ vortices are required to generate an $O(1)$ modification of the mean shear; see the appendix of [79] or note 34 at the end of [98].)

We conjecture, based upon the above analysis, that optimal streamwise vortices (whose forms change little at large Reynolds numbers) of amplitude $O(R^{-1})$ are required to generate linearly unstable streaks as $R \to \infty$ in PCF.

Finally, we note that the phase speeds of the disturbances which grow from the unstable streaks are again, as in PPF, determined by the centerline velocity of the mean flow, which in this case is zero. This agrees well with the inviscid model (4.3) with $\bar{U} = 0$.

4.8 Conclusions

Our analysis explains the different scalings for the threshold amplitudes of secondarily unstable streamwise vortices in PCF and PPF. Along the way we observed that vertical shear can have a dual nature in the process of transition described by ($*$). Shear enables the creation of streamwise streaks. However, the shear can also stabilize the streaks, preventing them from breaking down into the wavy streaks that may lead to turbulence.

The stability or instability of the streaks is determined by a competition between the spanwise and vertical shear. In the case of PCF this means that the laminar uniform shear must be flattened by an $O(1)$ modification of the mean flow. Thus, in PCF, the first stage of transition in ($*$) is affected by strongly nonlinear processes. However, this is not at all the case in PPF, where the laminar profile is perfectly suitable for the streak instability. No nonlinear modification of the laminar profile is necessary and the first stage of ($*$) can be regarded as entirely linear. The optimal disturbance, streamwise vortices, grows large by a linear mechanism and leads directly to a secondary linear instability.

We have already seen one sense in which PPF is less stable than PCF, but why does transition occur at lower Reynolds numbers in PCF than in PPF? This is really just a consequence of the arbitrary way in which the Reynolds numbers are defined for these flows. Given the central role of the vertical shear in the transition process, a more meaningful definition of the Reynolds number might be based on the dimensions of a typical region of vertical shear. The Reynolds number we used above is based on the channel half-width and difference between the wall and centerline velocities. In PPF, these scales correspond perfectly to the shear regions between the walls and the centerline, which seem to operate independently in the transition process. However, in PCF, the entire shear region between the walls is involved in transition. This suggests that a Reynolds number based on the channel width and the difference between the wall velocities in PCF might be more meaningful in comparisons of transitional Reynolds numbers. If this different Reynolds number is adopted for PCF, then transition would first occur at approximately 1200–1400 in PCF and at the usual 1000 in PPF.

Chapter 5

Pseudospectra of the Hille-Phillips operator*

In Chapters 2-4 we presented several non-normal matrices and operators A whose corresponding evolution operators e^{tA} displayed transient behavior at finite times that was very different from the asymptotic behavior as $t \to \infty$. Nearly all of those matrices and operators had the property that $\|e^{tA}\|$ could grow transiently for finite t, potentially by many orders of magnitude, but $\|e^{tA}\| \to 0$ as $t \to \infty$ because the spectrum of A was contained in the stable complex half-plane. However, if A is an unbounded operator, the time asymptotic behavior of $\|e^{tA}\|$ is not necessarily determined by the spectrum of A. In this chapter we examine two operators A for which the spectrum of A completely fails to predict the behavior of $\|e^{tA}\|$ as $t \to \infty$.

In 1957 Hille and Phillips [43] presented the first known example of a semigroup

*This chapter is adapted from a paper of the same title, submitted to *Integral Equations and Operator Theory* [1].

e^{tA} such that the norm of the semigroup $\|e^{tA}\|$ is not asymptotically determined by the spectrum of its generator A. Their example is not easily accessible and requires a knowledge of fractional integration operators. In particular, it is not easy to see why $\|e^{tA}\|$ behaves as it does. In this chapter we present a plot of the pseudospectra of A, and some known results connecting pseudospectra with $\|e^{tA}\|$. The plots of pseudospectra yield a graphical representation of the resolvent that makes the mathematically anomalous behavior of $\|e^{tA}\|$ easily understandable — thanks to an elegant result proved by Prüss [75]. Along the way, we also present the pseudospectra of a more elementary example due to Zabczyk [104].

In the next section we discuss the connections between the norm asymptotic behavior of a semigroup and the pseudospectra of its generator. In Sections 5.2–5.3 we meet the Zabczyk and Hille–Phillips examples and their pseudospectra. Some computational details involved in computing the pseudospectra are presented in Section 5.4. Finally, in Section 5.5 we introduce a corollary to Theorem 5.1.1 which applies to the examples considered here.

5.1 $\|e^{tA}\|$ as $t \to \infty$ and pseudospectra

Let $\mathcal{H}$ be a complex Hilbert space with norm $\|\cdot\|$ and let e^{tA} be a C_0-semigroup in $\mathcal{H}$ with generator A. The *exponential type* or *growth bound* of e^{tA} is

$$\omega_0(A) = \lim_{t\to\infty} \frac{\log \|e^{tA}\|}{t} \tag{5.1}$$

(the limit always exists). The *spectral abscissa* of A is

$$\alpha(A) = \sup_{z \in \Lambda(A)} \operatorname{Re} z,$$

where $\Lambda(A)$ denotes the spectrum of A.

Bounded linear operators and normal operators are examples of operators which have the *spectrum determined growth property* [75]. For such an operator A we have $\alpha(A) = \omega_0(A)$; see Corollary 5.1.1 below. However, in the case of unbounded operators, the most we can say in general is $\alpha(A) \leq \omega_0(A)$. Both of the examples we consider demonstrate that this inequality can be strict. In fact, the Hille–Phillips example has the property that $\Lambda(A)$ is empty, so $\alpha(A) = -\infty$, yet $\omega_0(A) = \pi/2$.

When the spectrum of the generator fails to reveal the asymptotic norm behavior of the semigroup, we need to look elsewhere. It is well known that $\|e^{tA}\|$ is related to the size of the resolvent, that is to $\|(\lambda I - A)^{-1}\|$, on certain regions in the complex plane. Pseudospectra provide a convenient language for discussing these matters. Let $\mathcal{B}(\mathcal{H})$ be the set of bounded linear operators in $\mathcal{H}$ and $\mathcal{C}(\mathcal{H})$ the set of densely defined closed linear operators in $\mathcal{H}$. Suppose $A \in \mathcal{C}(\mathcal{H})$ and let $\rho(A)$ denote the resolvent set of A. For any $\epsilon > 0$, we define the *ϵ-pseudospectrum* of A by

$$\Lambda_\epsilon(A) = \{\lambda \in \rho(A) : \|(\lambda I - A)^{-1}\| \geq \epsilon^{-1}\} \cup \Lambda(A).$$

Intuitively, the resolvent norm is infinite in the spectrum, and large in the ϵ-pseudospectrum for small ϵ. An equivalent characterization in terms of operator perturbations is

$$\Lambda_\epsilon(A) = \text{closure}\{\lambda \in \mathbb{C} : \lambda \in \Lambda(A+E) \text{ for some } E \in \mathcal{B}(\mathcal{H}),\ \|E\| \leq \epsilon\}.$$

Note that $\Lambda_0(A) = \Lambda(A)$. For a proof of the equivalence of the above characterizations see Roch and Silbermann [84]. For a general discussion of pseudospectra see Trefethen [93].

To establish the connection between the pseudospectra of a linear operator and its exponential type, we define the *ϵ-pseudospectral abscissa* of a linear operator A,

$$\alpha_\epsilon(A) = \sup_{z\in\Lambda_\epsilon(A)} \operatorname{Re} z, \qquad \text{for } \epsilon > 0.$$

The following results describe the connections between pseudospectra and $\|e^{tA}\|$. These results are for the most part already known, but it is our opinion that they are more intuitive when framed in terms of pseudospectra. In particular, the pseudospectra yield pictures in the complex plane which, at a glance, illuminate the connections between the norm of the resolvent and the asymptotic norm behavior of the semigroup. The key result, Theorem 5.1.1, follows from the characterization of the spectrum of C_0-semigroups on a Hilbert space. Gearhart [26], in 1978, first proved the characterization for contraction C_0-semigroups. The general case was settled independently by Herbst [42] in 1983 and by Howland [45] and Prüss [75] in 1984. See any of these sources for details of the characterization, notably [75]. Prüss was the first to note the connection between the spectral characterization of the semigroup and the exponential type of its generator. Greiner and Nagel [30] also give an excellent overview of the spectral theory of C_0-semigroups on Banach spaces.

Theorem 5.1.1 *Let $\mathcal{H}$ be a Hilbert space with norm $\|\cdot\|$ and let e^{tA} be a C_0-*

semigroup in $\mathcal{H}$ with generator A. Then

$$\omega_0(A) = \inf\{\omega > \alpha(A) : \|(zI - A)^{-1}\| < \infty, \text{for } \operatorname{Re} z \geq \omega\}.$$

Equivalently, in terms of pseudospectra,

$$\omega_0(A) = \lim_{\epsilon \to 0^+} \alpha_\epsilon(A). \tag{5.2}$$

Proof. See any of the above references. □

Theorem 5.1.1 shows that the exponential type of a C_0-semigroup in a Hilbert space is in general determined by the ϵ-pseudospectral abscissas of its generator as $\epsilon \to 0$, not the spectral abscissa. For many operators, notably normal operators and bounded operators, the pseudospectral abscissas converge to the spectral abscissa as $\epsilon \to 0^+$, however, as the examples in this chapter illustrate, this may not happen if the operator is non-normal and unbounded.

As Prüss notes, Theorem 5.1.1 immediately provides a characterization of those C_0-semigroups in a Hilbert space whose norm asymptotic behavior is determined by the spectrum of their generator.

Corollary 5.1.1 *Under the same conditions as in* Theorem 5.1.1, *e^{tA} has the spectrum determined growth property, that is, $\omega_0(A) = \alpha(A)$, if and only if*

$$\alpha(A) = \lim_{\epsilon \to 0^+} \alpha_\epsilon(A).$$

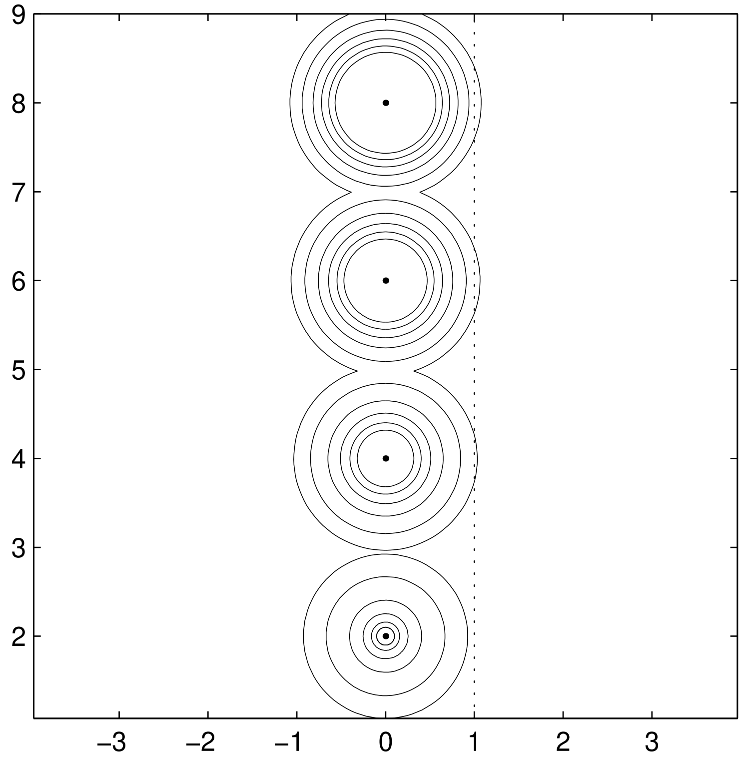

Figure 5.1: Pseudospectra of the Zabczyk operator. Shown are the boundary contours of $\Lambda_\epsilon(A)$ for $\log_{10}\epsilon = -10, -8, -6, -4, -2, -1$. Equivalently, these are contour lines of the resolvent corresponding to $\log_{10}\|(\lambda - A)^{-1}\| = 1, 2, 4, 6, 8, 10$. The dots indicate $\Lambda(A)$ and the dotted line is $\operatorname{Re}\lambda = \omega_0(A)$.

5.2 The Zabczyk operator

Before turning to the Hille–Phillips example, let us consider the far more elementary example published by Zabczyk eighteen years later, in 1975 [104].

In this example we have a C_0-semigroup on ℓ^2 with generator A, for which $\Lambda(A)$ is purely imaginary: $\alpha(A) = 0$, yet $\omega_0(A) = 1$. In fact, for this example we have $\|e^{tA}\| = e^t$ for all $t \geq 0$. Define for $k = 1, 2, \ldots$

$$B_k = \begin{pmatrix} 0 & 1 & & & \\ & 0 & 1 & & \\ & & 0 & \ddots & \\ & & & \ddots & 1 \\ & & & & 0 \end{pmatrix} \in \mathbb{C}^{10k\times 10k}.$$

Thus each B_k is a $10k \times 10k$ Jordan block; the number 10 is arbitrary, chosen to make the figures interesting. Let I_k be the identity matrix of dimension $10k$. Define $A_k = B_k + 2ikI_k$, where $i = \sqrt{-1}$. Finally, define A as the direct sum of the A_k, that is, as the infinite block diagonal matrix

$$A = \begin{pmatrix} A_1 & & & \\ & A_2 & & \\ & & A_3 & \\ & & & \ddots \end{pmatrix},$$

to be considered as an operator on ℓ^2. Since A is block diagonal, it follows that the resolvent $(\lambda I - A)^{-1}$ is also block diagonal for $\lambda \in \rho(A)$. The norm of a block diagonal operator is the supremum of the norms of the diagonal blocks:

$$\|(\lambda I - A)^{-1}\| = \sup_k \|(\lambda I - A_k)^{-1}\|.$$

In particular, for any $\epsilon \geq 0$,

$$\Lambda_\epsilon(A) = \bigcup_{k=1}^{\infty} \Lambda_\epsilon(A_k)\,.$$

As it happens, the pseudospectra of triangular Toeplitz matrices have been studied [81]. The ϵ-pseudospectra of each block A_k are disks of some radii $r(\epsilon, k)$ centered at $2ik$; see Figure 5.1. Note that as we move out out along the positive imaginary axis the radii of the disks are increasing. The matrices A_k are increasingly non-normal, and as k grows, their eigenvalues become increasingly sensitive

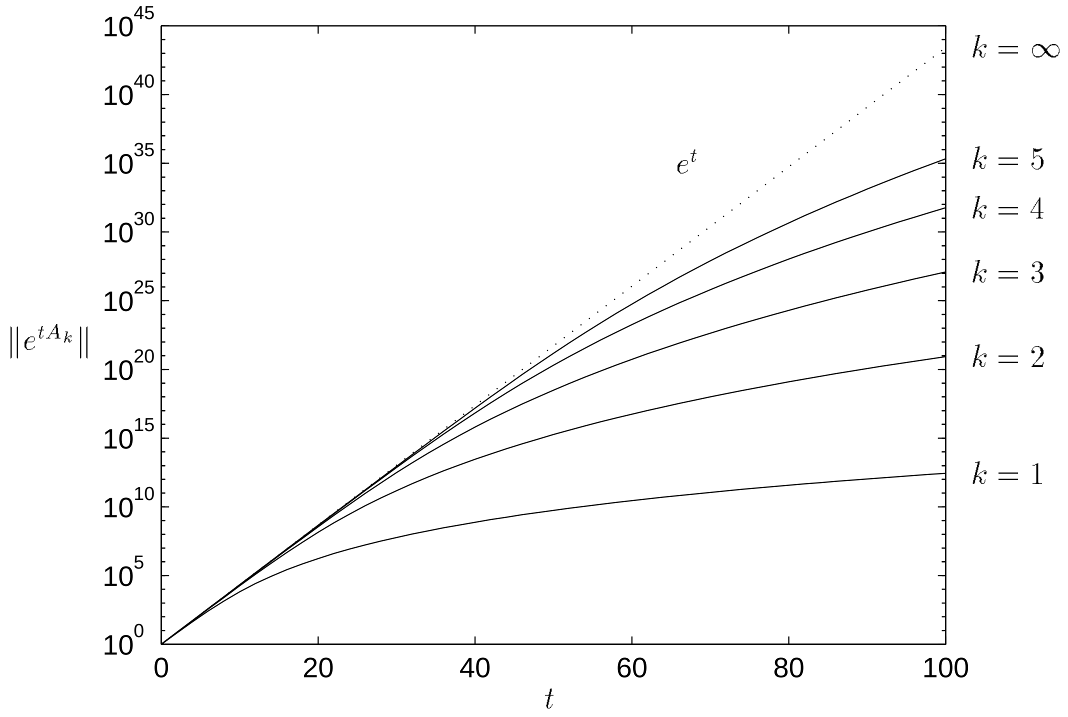

Figure 5.2: Evolution norms for the Zabczyk operator.

to perturbations. For large k and small ϵ, $r(\epsilon, k) \approx \epsilon^{1/(10k)}$. For example, with $\epsilon = 10^{-8}$ and $k = 3$, $r(\epsilon, k) = .5476$ and $\epsilon^{1/(10k)} = .5412$. In the limit, $r(\epsilon, k) \to 1+\epsilon$ as $k \to \infty$.

Figure 5.2 gives some insight into why $\|e^{tA}\| = e^t$ even though $\Lambda(A)$ is purely imaginary. Note that we have

$$\|e^{tA}\| = \sup_k \|e^{tA_k}\| = \sup_k \|e^{tB_k}\|.$$

If we consider the curves $\|e^{tA_k}\|$ for increasing k as shown in the figure, we see that they are approaching the limiting curve e^t. In other words, for any $t > 0$ and $\delta > 0$, we can find a sequence $v \in \ell^2$, with $\|v\| = 1$, such that $\|e^{tA}v - e^t v\| < \delta$. These functions v are *pseudo-eigenfunctions* of A [94]. Even though an eigenfunction u of A can yield only $\|e^{tA}u\| = 1$, the pseudo-eigenfunctions can excite much more growth.

In this example, each A_k has asymptotic behavior consistent with $\alpha(A_k) = 0$, but there is no such behavior that is uniform with respect to k. The infinite extent of the imaginary axis is what makes it possible to capture this non-uniformity in a single operator.

It is worth noting that Renardy [82] constructed, in the same style as the Zabczyk example, an operator A which generates a differentiable semigroup such that the semigroup generated $A + B$ is not differentiable for bounded perturbations B. Thus, he proved that differentiable semigroups are not necessarily preserved under bounded perturbations of their generators.

5.3 The Hille–Phillips operator

The earlier example of Hille and Phillips published in 1957 [43] is more difficult to get our hands on. The example is based on the Riemann–Liouville integral of fractional order. Here we take $\mathcal{H} = \mathcal{L}^2(0,1)$ and define

$$[J(\xi)f](x) = \frac{1}{\Gamma(\xi)} \int_0^x (x-u)^{\xi-1} f(u)\, du \tag{5.3}$$

for $\operatorname{Re}\xi > 0$, $x \in [0,1]$. Hille and Phillips showed that $J(\xi)$ is a C_0-semigroup for $\operatorname{Re}\xi > 0$ and also gave explicit formulas for its generator A and its resolvent. Furthermore, they showed that A has empty spectrum.

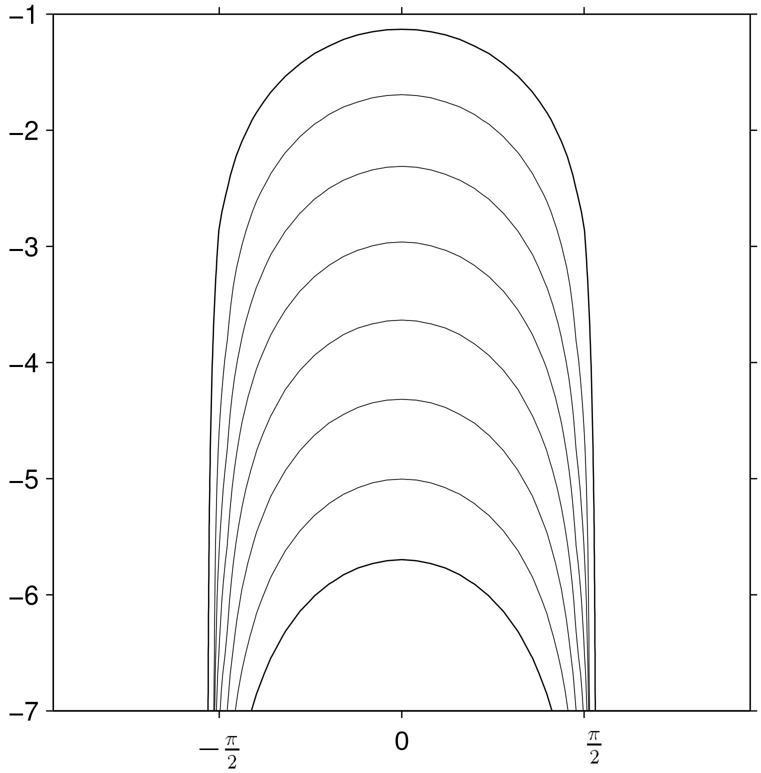

Figure 5.3: Pseudospectra of the Hille–Phillips operator. Shown are the boundary contours of $\Lambda_\epsilon(B)$, $\epsilon = 10^{-1}, 10^{-2}, \ldots, 10^{-128}$.

Hille and Phillips further showed, via some results due to Kober [53], that the operator $J(\xi)$ can be extended to purely imaginary values of the parameter $\xi = i\eta$, $\eta \in \mathbb{R}$. It is this extended operator which yields the example we wish to explore. If we restrict ourselves to $\eta \geq 0$, then $J(i\eta)$ is a C_0-semigroup on $\mathcal{H}$ with generator B, $B = iA$. (This restriction is not essential, for $J(i\eta)$ is in fact a group.) Thus the generator in this case has no spectrum, yet they show via another lemma of Kober's that

$$\|J(i\eta)\| = e^{\frac{\pi}{2}|\eta|} \qquad \text{for all } \eta \in \mathbb{R}.$$

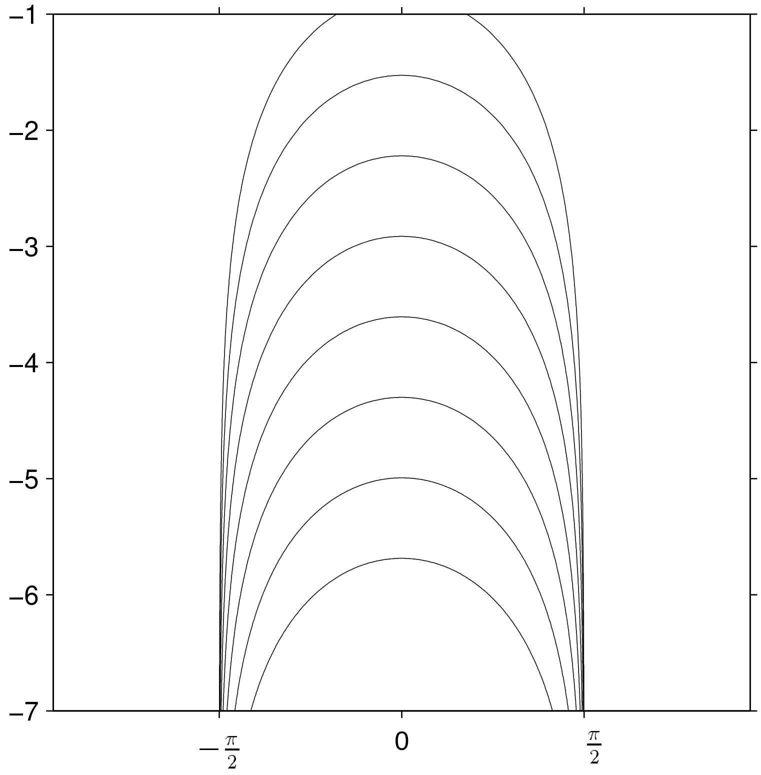

Figure 5.4: Model of the ϵ-pseudospectra of the Hille–Phillips operator. Shown are the curves corresponding to $\epsilon = 10^{-1}, 10^{-2}, \ldots, 10^{-128}$.

Therefore $J(i\eta)$ has exponential type $\omega_0(B) = \pi/2$, but this is not determined by the spectral properties of B. Instead we refer to the pseudospectra of B; see Figure 5.3.

A glance at the pseudospectra shows us what is happening. Even though B has no spectrum, the norm of the resolvent grows doubly exponentially as $\operatorname{Im}\lambda \to -\infty$ inside the strip $|\operatorname{Re}\lambda| < \pi/2$. Thus as far as norm asymptotics are concerned, the semigroup generated by B behaves as though the region inside the strip were the spectrum. Along the line $\operatorname{Re}\lambda = \pi/2$ we see that the resolvent grows unboundedly, that is, $\Lambda_\epsilon(B)$ intersects this line for every $\epsilon > 0$.

To develop some intuition about this problem, consider the following simple model proposed by L.N. Trefethen, based on techniques for analyzing pseudospectra of Toeplitz matrices and Wiener-Hopf integral operators by means of the analytic function known as the "symbol"; see [9, 77, 81]. The operator $J(1)$ is simply the definite integral from 0 to $\mathcal{H}$. Since this operator is e^A, we would like to, in some sense, take the logarithm. $J(1)$ maps $e^{\lambda x}$ to $(e^{\lambda x} - 1)/\lambda$. If $\operatorname{Re}\lambda \gg 0$, then -1 will be much smaller than $e^{\lambda x}$, so we have an ϵ-pseudo-eigenvector for $\epsilon \approx e^{-\operatorname{Re}\lambda}$. Thus the ϵ-pseudospectrum of the integration operator, for small ϵ, should be approximately the image of the curve $\operatorname{Re}\lambda = -\log\epsilon$ under the map λ^{-1}. Now we take the logarithm, and multiply by i (since $B = iA$). The result is our model of the pseudospectra of the Hille–Phillips operator: for small ϵ, $\Lambda_\epsilon(B)$ is bounded approximately by the image of the line $\operatorname{Re}\lambda = -\log\epsilon$ under the map $-i\log\lambda$. See Figure 5.4. In particular, along the negative imaginary axis we predict:

$$\|(\lambda I - B)^{-1}\| \approx e^{e^{|\lambda|}}.$$

5.4 Computations

The computation of the pseudospectral contours in the Zabczyk example is straightforward. As mentioned above, the pseudospectra of each block are disks of some radius centered at the eigenvalues of A. It is just a matter of using a zerofinding algorithm to solve for $r(\epsilon, j)$ and then feeding the information to a contour plotter.

On the other hand, we found the computation of the resolvent norm for the Hille–Phillips example to be quite challenging. Hille and Phillips give an explicit formula for the resolvent, obtained by Laplace transformation of the semigroup (5.3):

$$[R(\lambda; B)f](x) = \int_0^x K(x-u;\lambda) f(u)\,du. \tag{5.4}$$

The kernel of this Volterra integral operator is given by

$$K(s;\lambda) = -\frac{i}{s}\int_0^\infty \frac{e^{i\lambda y}s^y}{\Gamma(y)}\,dy. \tag{5.5}$$

There are two difficulties in attempting to compute the norm of (5.4). The first is that (5.5) has an oscillatory integrand, particularly as $\operatorname{Re}\lambda$ gets large. The second is that functions f_λ for which $\|R(\lambda;B)f_\lambda\| \approx \|R(\lambda;B)\|$ are difficult to model numerically, for they have singularities in their derivatives at the endpoints and are more oscillatory as $\operatorname{Im}\lambda$ gets large and negative. The kernel also has a singularity at $s=0$.

The first problem can be dealt with by a transformation suggested by Richard Chen [12]. We sketch some of the details here. Consider the integral

$$g(z) = \int_0^\infty \frac{z^y}{\Gamma(y)}\,dy,$$

where $z = re^{i\theta}$, with $|\theta| < \pi$. Let $g_\theta(r)$ denote $g(z)$ with θ fixed. Applying the Laplace transform $\mathcal{L}$ yields for $s > 1$

$$[\mathcal{L}g_\theta](s) = \int_0^\infty e^{-sr} g_\theta(r)\,dr = \frac{1}{s(\log s - i\theta)^2}.$$

Now, inverse Laplace transforming and integration by parts yields, for $c > 1$,

$$g_\theta(r) = \frac{r}{2\pi i}\int_{c-i\infty}^{c+i\infty} \frac{e^{rs}}{\log s - i\theta}\,ds. \tag{5.6}$$

The integrand now has a pole at $e^{i\theta}$, but since $|\theta| < \pi$, we can evaluate (5.6) via a contour integral by wrapping the branch cut along the negative real axis. This is valid for $|\theta| < \pi$, so after contour integration,

$$g(z) = ze^z + r \int_0^\infty \frac{e^{-ry}}{(\log y - i\theta)^2 + \pi^2}\, dy. \tag{5.7}$$

Note that (5.7) has much nicer numerical properties than (5.5), due to the rapidly convergent integral (when $r \neq 0$) and the absence of an oscillatory integrand. This formula can be used to express the kernel (5.5) as the sum of an exponential part and an easily computed integral. Let $\lambda = a + ib$ and substitute $z = se^{i\lambda} = se^{-b}e^{ia}$. Then (5.5) becomes

$$K(s;\lambda) = -ie^{i\lambda}e^{se^{i\lambda}} - ie^{-b} \int_0^\infty \frac{e^{-se^{-b}y}}{(\log(y) + ia)^2 + \pi^2}\, dy. \tag{5.8}$$

Note that the integral in (5.8) diverges when $s = 0$.

The second problem mentioned above is harder to deal with. Inside the half-strip $S = \{|\operatorname{Re}\lambda| < \pi/2, \operatorname{Im}\lambda > 1\}$, the exponential part of the kernel dominates and almost any method seems to work, provided one pays some attention to behavior near the endpoints. One simple approach is to form the Galerkin projection of (5.4) onto some subspace of $\mathcal{L}^2(0,1)$ that contains reasonable approximations to the functions f_λ. This means we need to choose a subspace that can approximate the endpoint singularities. One way to achieve this is to simply choose piecewise linear polynomials with breaks clustered near the endpoints of $[0,1]$, say, at N Chebyshev points. If we form the Galerkin projection of (5.4) onto this basis, then we get convergence to 3 digits for moderate values of $N \approx 40$.

However, for λ outside of S, the integral part of (5.8) dominates the kernel. The accurate evaluation of this integral for s near 0 is important because of the convolution nature of the resolvent, but unfortunately, this integral diverges when $s = 0$ and its accurate evaluation for small values of s is difficult. We have not entirely surmounted this difficulty. Better but not completely satisfactory results can be achieved by using a power method like that used to estimate the dominant eigenvalue of a matrix. In this method we use the adjoint $R^*(\lambda; iA)$, which has a similar but not identical form to (5.4). Using the same subspace as above (piecewise linear polynomials) we start with some random initial guess f_0 of norm 1 and iteratively form $f_{j+1} = R^*(\lambda; B)R(\lambda; B)f_j$. This is accomplished by applying $R(\lambda; B)$ followed by $R^*(\lambda; B)$; the product R^*R is never formed explicitly. The square root of the norm of f_{j+1} is taken as an estimate of $\|R(\lambda; B)\|$, f_{j+1} is renormalized, and we iterate until satisfactory convergence is achieved. Each evaluation of $R(\lambda; B)f_j$, or the analogous equation with the adjoint, is handled by the adaptive routines in QUADPACK [74]. In principle, this method should converge. Unfortunately, though it achieves better results for λ outside of S, it generally fails to converge for $\lambda \in \{\operatorname{Im}\lambda < -3, \operatorname{Re}|\lambda| > \pi/2\}$. In that region, the curves shown in Figure 5.3 are those suggested by experiments and theoretical considerations like Corollary 5.5.1, below.

5.5 A corollary

The two examples above both have the curious property that the norm of the semigroup is exactly exponential:

$$\|e^{tA}\| = e^{t\omega_0(A)} \qquad \text{for all } t \geq 0.$$

In this situation we can make a much stronger statement than usual about the growth of the resolvent in the half plane $\operatorname{Re}\lambda > \omega_0(A)$.

Corollary 5.5.1 *Under the same conditions as in* Theorem 5.1.1, *the following conditions are equivalent:*

$$\|e^{tA}\| = e^{t\omega}, \qquad \text{for all } t \geq 0. \tag{5.9}$$

$$\sup_{\operatorname{Re}\lambda=\mu>\omega} \|(\lambda I - A)^{-1}\| = \frac{1}{\mu-\omega}, \qquad \text{for all } \operatorname{Re}\lambda > 0. \tag{5.10}$$

$$\alpha_\epsilon(A) = \omega + \epsilon, \qquad \text{for all } \epsilon > 0. \tag{5.11}$$

Proof. The equivalence of (5.11) and (5.10) is just a matter of the definition of pseudospectra. Thus it is enough to show the equivalence of (5.9) and (5.11).

First we show that (5.9) implies (5.11). Assume (5.9). The fact that $\alpha_\epsilon(A) \leq \omega + \epsilon$ is the Hille–Yosida Theorem written in terms of pseudospectra. See Pazy [72], for example. By (5.1), $\omega_0(A) = \omega$. Theorem 1 tells us that the line $\operatorname{Re} z = \omega$ intersects all of the pseudospectra of A. Therefore for any $\delta > 0$, there exists y_δ such that $\omega + iy_\delta \in \Lambda_\delta(A)$. It is not hard to see that $\Lambda_{\epsilon+\delta}(A) \supseteq \Lambda_\delta(A) + \Delta_\epsilon$, where Δ_ϵ is a closed disk of radius ϵ. Hence $\omega + \epsilon + iy_\delta \in \Lambda_{\epsilon+\delta}(A)$, so $\alpha_{\epsilon+\delta}(A) \geq \omega + \epsilon$. Finally, since this inequality is true for every $\delta > 0$ and $\alpha_\epsilon(A)$ is a continuous function of ϵ, we have $\alpha_\epsilon(A) \geq \omega + \epsilon$.

Now we show that (5.11) implies (5.9). Assume (5.11). Again, by the Hille–Yosida Theorem, $\|e^{tA}\| \leq e^{\omega t}$. Now suppose $\|e^{t_0 A}\| < e^{\omega t_0}$ for some $t_0 > 0$. It follows that for any integer $n > 0$, $\|e^{nt_0 A}\| < e^{\omega t_0 n}$. Now by (5.1), $\omega_0(A) < \omega$, but by (5.2), this contradicts (5.11). $\square$

Appendix A

Outline of numerical methods used in streak stability investigations

Essentially four different numerical techniques are employed in Chapter 4 in our investigations of the linear stability of streamwise streaks in plane Couette flow and plane Poiseuille flow:

1. DNS — direct numerical simulation of the Navier–Stokes equations. (Fortran, based on the code of Lundbladh, Henningson, and Johansson [62])

2. FDNS — direct numerical simulation of the Navier–Stokes equations in which the streamwise independent portion of the velocity field is frozen (not allowed to evolve). (Fortran, based on an adaptation of the code used for DNS)

3. MAL — matrix analysis of the linearization of the Navier–Stokes equations about the laminar flow. (MATLAB, based on codes of Reddy and Baggett)

4. MAS — matrix analysis of the linearization of the Navier–Stokes equations about the streamwise streaks. (MATLAB, based on the code of Reddy [79])

MAL was used to generate the optimal streamwise vortices of [11] which we used as the initial conditions in our study. DNS was used to investigate the generation of streamwise streaks from streamwise vortices and the breakdown of streamwise streaks into wavy streaks. FDNS was used to study the stability of the streamwise streaks to perturbations which broke their streamwise independent symmetry. Finally, MAS was used to examine the spectrum and eigenfunctions of the linearization of the Navier–Stokes equations about the streamwise streaks.

Table A.1: The numerical method used to generate each figure in Chapter 4

Numerical method	Figure number
DNS	4.1, 4.2, 4.3, 4.4, 4.8, 4.10, 4.20
FDNS	4.11, 4.12, 4.13, 4.14, 4.17
MAL	4.6, 4.7
MAS	4.2, 4.15, 4.16, 4.17, 4.18, 4.19, 4.21

Table A.1 lists the primary numerical method used to generate the data in each figure appearing in Chapter 4 (two figures are not listed — Figure 4.5, which is a schematic, and Figure 4.9, which was generated by simply plotting the data from a two-mode truncation of the solution of equation (4.3)). Of course, the data in nearly every figure depends on the use of MAL to generate the optimal streamwise vortices used as initial conditions and DNS to simulate the production of the streamwise streaks whose stability we subsequently studied. For instance, each data point on the streak instability growth rate versus initial vortex amplitude curves in Figure 4.11 requires a combination of MAL (to generate the streamwise vortices), DNS (to generate the streamwise streaks), and FDNS (to determine the growth or decay rate of modes with a particular streamwise wavenumber due to the linear instability or stability of the streamwise streaks).

The purpose of this appendix is to present some additional details of the above numerical methods. We describe the spectral method and code used for the DNS in Section A.1 and explain how we employed the simulation code in the investigations of Chapter 4. We also list the considerable computing resources brought to bear on this problem. We explain how the code was modified for the FDNS in Sec A.2. In Section A.3 we briefly describe the two matrix analysis numerical methods, MAL and MAS, and their use in our investigations.

A.1 Direct numerical simulations

Incompressible flows in plane channels, with their particularly simple geometry, are perhaps the easiest flows to simulate numerically. However, the simulation of such a flow, even before the onset of turbulence, is a big computation. Since the flow is homogeneous in the streamwise and spanwise directions, it is assumed that the flow is periodic in those directions, but even in this simplified geometry, finite difference methods do not work well for high accuracy simulations and spectral methods are needed.

We used the spectral simulation code for plane Couette and Poiseuille flows written by Lundbladh, Henningson, and Johansson (hereafter LHJ) [62], to whom we are extremely grateful, at the Aeronautical Research Institute of Sweden. The spectral integration method used in their algorithm is due to Greengard [29]. The LHJ code has been used in a number of investigations including the simulation of turbulent spots in plane Couette flow [64], the simulation of subcritical transition from localized disturbances [38] and from a pair oblique waves [89] in plane Poiseuille flow, and the simulation of the breakdown of streamwise streaks in plane Couette and plane Poiseuille flows [79].

The code itself consists of approximately 8000 lines of Fortran, including a library of vectorized FFT routines. The simulation suite also includes a pre-processor for generating the initial velocity fields and post-processing routines for graphing the velocity field and amplitude statistics. The LHJ code has some parallelism enabled with compiler directives for Alliant and Cray parallel computers.

Most of our investigations of streamwise streaks and their stability were done by running the LHJ code (and modified versions of it) on individual nodes of the IBM SP2 at the Cornell Theory Center, for whose support we are grateful (we used approximately 100 hours of CPU time for the results in this thesis, and another 1100 hours in preliminary investigations). The SP2 consists of 512 nodes with distributed memory. Each node is based on a single RISC System/6000 processor with a peak performance of 266 MFLOPS. A typical run took approximately 1–1.5 hours, though some higher resolution simulations took several hours. The LHJ code was ported to the SP2 by Anne Trefethen, whose help was indispensable. She also converted the parallelization parts of the code so it would run in parallel on an SGI Power Challenge — a 16 node, shared memory computer. The simulation running in parallel on 4 nodes of the SGI was approximately 3 times faster than the simulation running in serial on a single node — a typical run took approximately 15 minutes. In the end, however, most of the simulations using the LHJ code (DNS and FDNS) and the MATLAB codes for the MAS were executed on individual nodes of the SP2. A few of the simulations, as well as the MAL (again in MATLAB), were run on on Sparc 5 and Sparc 10 workstations in Cornell's Center for Applied Mathematics.

Here is a brief description of how the LHJ code works. The starting point is the dimensionless incompressible Navier–Stokes equations for the channel flow, here written in vector notation,

$$\begin{gathered}\frac{\partial \mathbf{u}}{\partial t} + (\mathbf{u}\cdot\nabla)\mathbf{u} = -\nabla p + \frac{1}{R}\Delta\mathbf{u}, \\ \nabla\cdot\mathbf{u} = 0,\end{gathered} \tag{1.1}$$

where $\mathbf{u} = (u, v, w)$ are the streamwise, spanwise, and vertical velocities, respectively, and p is the pressure. The respective positions are x, y, and z. The Reynolds number $R = hV_d/\nu$, where h is the channel half-width, V_d the difference between the wall and centerline velocities, and ν the kinematic viscosity. The boundary conditions are $u(y=\pm1) = v(y=\pm1) = \frac{\partial}{\partial y}v(y=\pm1) = w(y=\pm1) = 0$. The solution is periodic in the unbounded directions with the fundamental domain defined by

$$x \in [-L_x/2, L_x/2], \quad y \in [-1,1], \quad z \in [-L_z/2, L_z/2]. \tag{1.2}$$

The streamwise and spanwise periodic directions are discretized by Fourier series.

The streamwise velocity component u becomes

$$u(x,y,z,t) = \mathrm{Re}\Big[\sum_{l=-(\frac{N_x}{2}-1)}^{\frac{N_x}{2}-1} \sum_{m=-(\frac{N_z}{2}-1)}^{\frac{N_z}{2}-1} \hat{u}_{lm}(y,t) e^{i(2\pi lx/L_x + 2\pi mz/L_z)}\Big], \tag{1.3}$$

where $N_x - 1$ and $N_z - 1$ are the numbers of Fourier modes in the respective directions. The expansions of v, w, and p are similar. The vertical direction is discretized by Chebyshev series, so that each Fourier coefficient in the above expansion of u, for instance, is written as a sum of the first N_y Chebyshev polynomials with time dependent coefficients. The time stepping is done by a semi-implicit scheme. The linear terms are discretized implicitly in time by a second order accurate Crank-Nicolson scheme, while the nonlinear advective terms are discretized explicitly in time by a four stage Runge–Kutta scheme (other lower order schemes are included with the code). For each time step, the linear terms are computed in Fourier space and the nonlinear terms are computed in physical space, with FFT's being used to transform between the spaces — a pseudospectral method. See [62] for a complete description.

In all of the simulations in Chapter 4, we used a periodic box of dimensions $8\pi \times 2 \times \pi$ in the x, y, and z directions, which corresponds to $L_x = 8\pi$ and $L_z = \pi$. In most of the simulations, 32, 49, and 32 points (N_x, N_y, and N_z) were used in the respective directions (all of the FFT's were dealiased by the 3/2 rule). We increased the respective number of points to 48, 73, and 48 in a few simulations with the modified code (FDNS — detailed in the next section) to check the accuracy of the streak instability growth rates reported in Section 4.4; no differences were observed at the higher resolution. The plots in Figures 4.1, 4.3, 4.4, 4.8, 4.10 and 4.20 were produced from a simulation at the higher resolution.

In our investigations, we always added streamwise vortices of the form (4.1) and amplitude ϵ (as determined by $\epsilon = 2\sqrt{E}$, where E is the energy density as defined by (4.6)) with spanwise wavenumber $\beta_0 = 2$ to the laminar flow at $t = 0$. In the expansion of the velocity components (1.3) this corresponds to adding Fourier modes with $l = 0$ and $m = \pm 1$ (recall that $L_z = \pi$) whose Fourier coefficients are the Chebyshev expansions of the optimal streamwise vortices of Butler and Farrell [11] (normalized so that the vortices have amplitude ϵ). We will describe briefly how the optimal streamwise vortices were obtained in Section A.3.

We used DNS in two ways in Chapter 4. One way was in full simulations of the transition process (Figures 4.1, 4.2, 4.3, 4.4, 4.8, 4.10, and 4.20). In those simulations, along with the streamwise vortices, noise was added at $t = 0$ to break the streamwise independent symmetry of the streamwise vortices (without which transition could not occur). The y-dependence of the noise was in the form of Stokes modes with randomly chosen coefficients. The noise, of mean amplitude approximate 10^{-5}, was added at each of the wavenumbers in the expansion (1.3).

The other way in which DNS was used was to produce streamwise streaks so that we could investigate their stability. Optimal streamwise vortices with spanwise wavenumber $\beta_0 = 2$ were again added to the laminar flow at $t = 0$, but no noise was added because we wanted clean, purely two-dimensional streaks. As the streaks grew, nonlinear interactions resulted in the production of harmonics $(2\beta_0, 3\beta_0, \ldots)$ and mean flow modification. However, we were most interested in the linear growth of streaks, which occurs only in the $\beta_0 = 2$ mode. Thus the initial velocity field was integrated from time $t = 0$ to time $t = t_{\max}$, which is the time when the amplitude of all components of the $\beta_0 = 2$ mode (corresponding to $l = 0$ and $m = \pm 1$) is maximized. The velocity field was, of course, purely two-dimensional throughout these simulations, but we did not exploit this symmetry.

The two-dimensional streamwise streak velocity field used in the streak stability investigations of Section 4.4 includes all of velocity components of all of the streamwise independent modes, that is, it is the entire velocity field at time $t_{\max}$ as described in the previous paragraph. (The streamwise streaks used in the MAS were formed from only the streamwise velocity components of that field; see Section A.3.) It has components $u(y, z, t_{\max})$, $v(y, z, t_{\max})$, $w(y, z, t_{\max})$, where u is given by

$$u(x, y, z, t_{\max}) = \mathrm{Re}\Big[\sum_{m=-(\frac{N_z}{2}-1)}^{\frac{N_z}{2}-1} \hat{u}_{0m}(y, t_{\max}) e^{i2\pi m z/L_z}\Big], \tag{1.4}$$

where the $\hat{u}_{0m}(y, t_{\max})$ are sums of Chebyshev polynomials, with time-dependent coefficients, as described above. The expansions for v and w are similar. The modified LHJ simulation code (FDNS), in which this velocity field is held fixed to study its linear stability, is described in the next section.

We would like to comment that it has not been until the 1990s that high-accuracy spectral computations like these for incompressible flows have been routinely feasible. This is one of the major reasons, though not the only one, why so much progress has been made in the in the understanding of the fundamental phenomena of transition in the past few years.

A.2 Simulations with frozen streamwise independent velocity field

In Section 4.4 we studied the dependence of the streak instability growth rate on the amplitude of the initial streamwise vortices. The essence of the procedure was to first generate clean streamwise streaks by DNS as described in the previous section. Second, noise was added to all of the velocity components of the modes with a particular streamwise wavenumber (corresponding to a particular choice of $\pm l$ in (1.3), for instance, $\alpha_0 = 0.5$ corresponds to $l = \pm 2$ ($L_x = 8\pi$) and all m). Third, the resulting velocity field was integrated, but the streamwise independent part of the velocity field was not allowed to evolve. This third step is the FDNS, which we describe in this section.

The code used for the FDNS was a slightly modified version of the LHJ code. The idea was to treat the streamwise streaks, that is, the streamwise independent velocity field $(u(y,z,t_{\max}), v(y,z,t_{\max}), w(y,z,t_{\max}))$, as constant, while allowing only the streamwise dependent modes to evolve. In this way, we simulated a linear stability analysis of steady-state streaks. To accomplish this we modified the LHJ code so that at the beginning of each iteration (there are several iterations within each physical time step because of the four stage Runge-Kutta scheme), all of the streamwise independent ($l = 0$) modes were reset to their values from time $t_{\max}$. Specifically, the streamwise independent modes were reset before the nonlinear terms were computed in each iteration. Therefore, the evolving streamwise dependent modes interacted nonlinearly with only with the frozen (from time $t_{\max}$) streamwise independent modes (and, as detailed in Chapter 4, the streamwise dependent modes interacted nonlinearly amongst themselves, producing negligible harmonics).

As noted in Table A.1, the FDNS numerical method was used to generate the data in Figures 4.11, 4.12, 4.13, and 4.14, and some of the data in Figure 4.17. The ideas behind using the FDNS, essentially doing long-time integrations to study the linear stability of steady states, are standard. Reddy, Schmid, and Baggett [79] did essentially the same thing in their study of the linear stability of streamwise streaks, except that the entire velocity field was allowed to evolve. In that case, the slow viscous decay of the streaks made it difficult to examine the growth rates of particular oblique modes. That difficulty is what motivated us to modify the LHJ code for FDNS.

A.3 Matrix analysis methods

Two different matrix analysis methods were used in our investigations, MAS and MAL. Recall that MAS and MAL are the acronyms we gave to matrix analysis of the linearization of the Navier–Stokes equations about the streamwise streaks and the laminar flow, respectively.

The MAS code was written by Satish Reddy at Oregon State University and was used in the numerical investigation of the stability of streamwise streaks in plane Couette and plane Poiseuille flow in [79]. It is based on a standard linear stability analysis in which the Navier–Stokes equations are linearized about the streamwise streaks. The perturbation quantities are expanded in Fourier modes in the unbounded directions and Chebyshev polynomials in the bounded wall direction. The time-dependence of the perturbations is assumed to be of the form $e^{i\sigma t}$ ($\sigma \in \mathbb{C}$) resulting in an eigenvalue problem for the eigenvalue σ. Similar linear stability analyses may be found in [24, 25, 35, 61, 97, 103].

The vertical and spanwise velocity components of the streamwise streaks are assumed to be zero, and it is assumed that the streaks are a steady state. The streamwise velocity component of the streaks has the form, as stated in Chapter 4,

$$U(y,z) = \sum_{k=0}^{\infty} U_k(y) \cos k\beta_0 z, \tag{1.5}$$

where the U_k are real. The precise form of the perturbation quantities was given in Chapter 4. The $U_k(y)$, as well as the Fourier coefficients of the perturbation quantities were expanded in the first n_y Chebyshev polynomials. Similarly, the Fourier series in (1.5) must be truncated. Based upon the results in [79], we used $n_y = 33$ in all of our investigations, and the first 8 terms in (1.5) (except where noted in Chapter 4). In Reddy's code the number of Fourier modes used in the expansions of the perturbation quantities is increased until successive approximations to the growth rate $\mathrm{Im}[\sigma]$ vary by less that 0.5%.

The streamwise velocity component of the streamwise streaks at time $t_{\max}$ used in the MAS code is determined by the DNS as described in Section A.1. The actual matrices, whose eigenvalues (and in some cases, eigenfunctions) we solved for in MATLAB, had dimensions typically ranging from 400 to 800 (depending on how many terms were necessary to achieve converged growth rates).

The other matrix analysis method used in Chapter 4 was MAL. This was used to generate the optimal streamwise vortices of [11] which were the initial conditions in our study. The Navier–Stokes equations are linearized about the laminar flow and discretized exactly as they were for MAS. Let $\mathcal{L}$ be the matrix which governs the evolution of streamwise independent perturbations with spanwise wavenumber $\beta_0 = 2$ in the discretized, truncated equations. $\mathcal{L}$ is a discrete approximation to the familiar Orr–Sommerfeld/Squire operator of hydrodynamic stability theory.

The idea is to find the vector v_0 (the Chebyshev coefficients of the streamwise vortices) such that $e^{-it\mathcal{L}}v_0$ achieves the greatest possible transient growth in the energy norm; see Figure 1.1 in Chapter 1. This is accomplished by applying the singular value decomposition to the matrix $We^{-it\mathcal{L}}W^{-1}$. The matrix W is a weight matrix determined so that $\|Wv\|_2 = \|v\|_{\mathrm{energy}}$, where $\|\cdot\|_2$ is the usual Euclidean vector norm, and v is the vector of Chebyshev coefficients.

The MAL codes were written and executed in MATLAB. The matrices were typically of size 100–150. Further details on optimal perturbations in shear flows may be found in [11]. A detailed description of the discretization and the weight matrices is contained in [80].

Bibliography

[1] J.S. Baggett. Pseudospectra of the Hille–Phillips operator. *Submitted to Integral Equations and Operator Theory*, 1996.

[2] J.S. Baggett, T.A. Driscoll, and L.N. Trefethen. A mostly linear model of transition to turbulence. *Phys. Fluids*, 7(4):833–838, 1995.

[3] J.S. Baggett and L.N. Trefethen. Low-dimensional models of subcritical transition to turbulence. *To appear in Phys. Fluids*, 1996.

[4] A.A. Bakchinov, G.R. Grek, B.G.B. Klingmann, and V.V. Kozlov. Transition experiments in a boundary layer with embedded streamwise vortices. *Phys. Fluids*, 7:820–832, 1995.

[5] D.J. Benney and L.H. Gustavsson. A new mechanism for linear and nonlinear hydrodynamic instability. *Stud. Appl. Math.*, 64:185–209, 1981.

[6] L.P. Bernal and A. Roshko. Streamwise vortex structures in plane mixing layers. *J. Fluid Mech.*, 170:499–525, 1986.

[7] L. Boberg and U. Brosa. Onset of turbulence in a pipe. *Z. Naturforschung*, 43a:697–726, 1988.

[8] A. Bottaro and B.G.B. Klingmann. On the linear breakdown of Görtler vortices. *Eur. J. Mech. B/Fluids*, 15(3), 1996.

[9] A. Böttcher. Pseudospectra and singular values of large convolution operators. *J. Integral Eq. Appl.*, 6:267–301, 1994.

[10] S. Bottin, O. Dauchot, and F. Daviaud. Transition to turbulence in plane Couette flow: The streamwise vortices role. *Submitted to J. Fluid Mech.*, 1996.

[11] K.M. Butler and B.F. Farrell. Three-dimensional optimal perturbations in viscous shear flow. *Phys. Fluids*, 4:1637–1650, 1992.

[12] R. Chen. Personal communication. Yale University, March 1994.

[13] R.M. Clever and F.H. Busse. Instabilities of longitudinal rolls in the presence of Poiseuille flow. *J. Fluid Mech.*, 229:517–529, 1991.

[14] R.M. Clever and F.H. Busse. Three-dimensional convection in a horizontal fluid layer subjected to constant shear. *J. Fluid Mech.*, 234:511–527, 1992.

[15] A.J. Conley. Centrifugal destabilization and restabilization of plane shear flows. Technical Report MCS-P511-0395, Argonne National Laboratory, 1995.

[16] A.J. Conley and H.B. Keller. Wavy vortices in plane Couette flow. Technical Report MCS-P495-0195, Argonne National Laboratory, 1995.

[17] O. Dauchot and F. Daviaud. Finite amplitude perturbation and spots growth mechanism in plane Couette flow. *Phys. Fluids*, 7:335–343, 1995.

[18] O. Dauchot and F. Daviaud. Streamwise vortices in plane Couette flow. *Phys. Fluids*, 7:901–903, 1995.

[19] F. Daviaud, J. Hegseth, and P. Bergé. Subcritical transition to turbulence in plane Couette flow. *Phys. Rev. Lett.*, 69:901–903, 1992.

[20] S.J. Davies and C.M. White. An experimental study of the flow of water in pipes of rectangular section. *Proc. Roy. Soc. Lond.*, 119:92–107, 1928.

[21] B. Diedrichs. *Linear and non-linear growth of disturbances in channel flows.* PhD thesis, Luleå University of Technology, Sweden, 1996.

[22] P.G. Drazin and W.H. Reid. *Hydrodynamic Stability.* Cambridge University Press, 1981.

[23] T. Ellingsen and E. Palm. Stability of linear flow. *Phys. Fluids*, 18:487–488, 1975.

[24] W.H. Finlay, J.B. Keller, and J.H. Ferziger. Instability and transition in curved channel flow. *J. Fluid Mech.*, 194:417–456, 1988.

[25] T.M. Fischer and U. Dallmann. Primary and secondary instability analysis of three-dimensional boundary-layer flow. *Phys. Fluids*, 3:2378–2391, 1991.

[26] L. Gearhart. Spectral theory for contraction semigroups on Hilbert space. *Trans. Amer. Math. Soc.*, 236:385–394, 1978.

[27] T. Gebhardt and S. Grossmann. Chaos transition despite linear stability. *Phys. Rev. E*, 50:3705–3711, 1994.

[28] I.C. Gohberg and M.G. Kreĭn. *Introduction to the Theory of Linear Nonselfadjoint Operators.* Amer. Math. Soc., 1969.

[29] L. Greengard. Spectral integration and two-point boundary value problems. Technical Report YALEU/DCS/RR-646, Yale University, 1989.

[30] G. Greiner and R. Nagel. *One-parameter Semigroups of Positive Operators*. Lecture Notes in Mathematics (1184). Springer-Verlag, 1980.

[31] L.H. Gustavsson. Resonant growth of three-dimensional disturbances in plane Poiseuille flow. *J. Fluid Mech.*, 112:253–264, 1981.

[32] L.H. Gustavsson. Direct resonance of nonaxisymmetric disturbances in plane Poiseuille flow. *Stud. Appl. Math.*, 80:95–108, 1989.

[33] L.H. Gustavsson. Energy growth of three-dimensional disturbances in plane Poiseuille flow. *J. Fluid Mech.*, 224:241–260, 1991.

[34] L.H. Gustavsson and L.S. Hultgren. A resonance mechanism in plane Couette flow. *J. Fluid Mech.*, 98:149–159, 1980.

[35] P. Hall and N.J. Horseman. The linear inviscid instability secondary instability of longitudinal vortex structures in boundary-layers. *J. Fluid Mech.*, 232:357–375, 1991.

[36] J.M. Hamilton and F.H. Abernathy. Streamwise vortices and transition to turbulence. *J. Fluid Mech.*, 264:185–212, 1994.

[37] J.M. Hamilton, J. Kim, and F. Waleffe. Regeneration mechanisms of near-wall turbulence structures. *J. Fluid Mech.*, 287:317–348, 1995.

[38] D.S. Henningson and P.H. Alfredsson. The wave structure of turbulent spots in plane Poiseuille flow. *J. Fluid Mech.*, 178:405, 1989.

[39] D.S. Henningson and S.C. Reddy. On the role of linear mechanisms in transition to turbulence. *Phys. Fluids*, 6:1396–1398, 1994.

[40] D.S. Henningson and P.J. Schmid. Vector eigenfunction expansions for plane channel flows. *Stud. Appl. Math.*, 87:15–43, 1992.

[41] T. Herbert. Periodic secondary motions in a plane channel. In A.I. van de Vooren and P.J. Zandbergen, editors, *Proc. 5th Int. Conf. Numer. Methods Fluid Dyn.*, pages 235–240. Springer–Verlag, 1976.

[42] T. Herbert. On perturbation methods in nonlinear stability theory. *J. Fluid Mech.*, 126:167–186, 1983.

[43] E. Hille and R.S. Phillips. *Functional Analysis and Semi-groups*. American Mathematical Society, 1957.

[44] C.M. Ho and P. Huerre. Perturbed free shear layers. *Ann. Rev. Fluid Mech.*, 16, 1984.

[45] J.S. Howland. On a theorem of Gearhart. *Integral Equations and Operator Theory*, 7:138–142, 1984.

[46] C. Johnson, R. Rannacher, and M. Boman. On transition to turbulence and error control in CFD. Technical Report 1994-26, Dept. of Math., Chalmers Inst. of Tech., 1994.

[47] Lord Kelvin. On the stability of steady and of periodic fluid motion. *Phil. Mag. (5)*, 23:459–464,529–539, 1887.

[48] Lord Kelvin. Stability of fluid motion—rectilinear motion of viscous fluid between two parallel plates. *Phil. Mag. (5)*, 24:188–196, 1887.

[49] J. Kim, P. Moin, and R. Moser. Turbulence statistics in fully developed channel flow at low Reynolds number. *J. Fluid Mech.*, 177:133–166, 1987.

[50] J. Kim and R.D. Moser. On the secondary instability in plane Poiseuille flow. *Phys. Fluids*, 1:775–777, 1989.

[51] S.J. Kline, W.C. Reynolds, F.A. Schraub, and P. Runstadler. The structure of turbulent boundary layers. *J. Fluid Mech.*, 30:741–773, 1967.

[52] B.G.B. Klingmann. On transition due to three-dimensional disturbances in plane Poiseuille flow. *J. Fluid Mech.*, 240:167–195, 1992.

[53] H. Kober. On a theorem of Schur and on fractional integrals of purely imaginary order. *Trans. Amer. Math. Soc.*, 50:160–174, 1941.

[54] V.V. Kozlov and B.G.B. Klingmann. The influence of riblets on a boundary layer with embedded streamwise vortices. *Phys. Fluids*, 7, 1995.

[55] G. Kreiss, A. Lundbladh, and D.S. Henningson. Bounds for threshold amplitudes in subcritical shear flows. *J. Fluid Mech.*, 270:175–198, 1994.

[56] M.T. Landahl. A note on an algebraic instability of inviscid parallel shear flows. *J. Fluid Mech.*, 98:243–251, 1980.

[57] J.C. Lasheras and H. Choi. Three-dimensional instability of a plane free shear layer: An experimental study of the formation evolution of streamwise vortices. *J. Fluid Mech.*, 189:53–86, 1988.

[58] C. Le Cunff and A. Bottaro. Linear stability of shear profiles and relation to the secondary instability of Dean flow. *Phys. Fluids*, 5:2161–2171, 1993.

[59] M.J. Lee, J. Kim, and P. Moin. Structure of turbulence at high shear rate. *J. Fluid Mech.*, 216:561–583, 1990.

[60] H.J. Leutheusser and V.H. Chu. Experiments on plane Couette flow. *J. Hydraul. Div. Amer. Soc. Civ. Eng.*, 97:1269–1284, 1971.

[61] F. Li and M.R. Malik. Fundamental and subharmonic secondary instabilities of Görtler vortices. *J. Fluid Mech.*, 297:77–100, 1995.

[62] A. Lundbladh, D.S. Henningson, and A.V. Johansson. An efficient spectral integration method for the solution of the Navier-Stokes equations. Technical Report FFA TN 1992-28, The Aeronautical Research Institute of Sweden, 1992.

[63] A. Lundbladh, D.S. Henningson, and S.C. Reddy. Threshold amplitudes for transition in channel flows. In *Transition, Turbulence, and Combustion*. Kluwer Academic Publishers, The Netherlands, 1994.

[64] A. Lundbladh and A.V. Johansson. Direction simulation of turbulent spots in plane Couette flow. *J. Fluid Mech.*, 229:499–516, 1991.

[65] O.J.E. Matsson and P.H. Alfredsson. Experiments on instabilities in curved channel flow. *Phys. Fluids*, 4:1666–1676, 1992.

[66] M. Matsubara and P.H. Alfredsson. Free stream turbulence induced by boundary layer transition. *Bull. Amer. Phys. Soc.*, 40:1956, 1995.

[67] L.D. Meshalkin and Ia. G. Sinai. Investigation of the stability of a stationary solution of a system of equations for the plane movement of an incompressible viscous liquid. *J. Appl. Math. Mech. (PMM)*, 25:1700–1705, 1961.

[68] M. Nagata. Three-dimensional finite-amplitude solutions in plane Couette flow: Bifurcation from infinity. *J. Fluid Mech.*, 217:519–527, 1990.

[69] M. Nishioka, S. Iida, and Y. Ichikawa. An experimental investigation of the stability of plane Poiseuille flow. *J. Fluid Mech.*, 72:731–751, 1975.

[70] W.M. Orr. The stability or instability of the steady motions of a perfect liquid and a viscous liquid. *Proc. Roy. Irish Acad.*, 27:9–138, 1907.

[71] S.A. Orszag and A.T. Patera. Secondary instability of wall bounded shear flows. *J. Fluid Mech.*, 112:347–385, 1983.

[72] A. Pazy. *Semigroups of Linear Operators and Applications to Partial Differential Equations*. Springer-Verlag, 1983.

[73] P. Petitjeans and J.E. Wesfreid. Structure and perturbation in Görtler vortex flow. In C.D. Andereck and F. Hayoth, editors, *Ordered and Turbulent Patterns in Plane Couette Flow*. Publ. Press, 1992.

[74] R. Piessens, E. de Doncker-Kapenge, C.W. Ueberhuber, and D.K. Kahaner. QUADPACK*: a Subroutine Package for Automatic Integration*. Springer-Verlag, 1983.

[75] J. Prüss. On the spectrum of C_0-semigroups. *Trans. Amer. Math. Soc.*, 284:847–857, 1984.

[76] Lord Rayleigh. On the stability, or instability, of certain fluid motions. *Proc. Roy. Soc. Lond.*, 11:57–70, 1880.

[77] S.C. Reddy. Pseudospectra of Wiener–Hopf integral operators and constant-coefficient differential operators. *J. Integral Eq. Appl.*, 5:369–403, 1993.

[78] S.C. Reddy and D.S. Henningson. Energy growth in viscous channel flows. *J. Fluid Mech.*, 252:209–238, 1993.

[79] S.C. Reddy, P.J. Schmid, and J.S. Baggett. On stability of streamwise streaks and transition to turbulence in plane channel flows. *Submitted to J. Fluid Mech.*, 1996.

[80] S.C. Reddy, P.J. Schmid, and D.S. Henningson. Pseudospectra of the Orr-Sommerfeld operator. *SIAM J. Appl. Math.*, 53:15–47, 1993.

[81] L. Reichel and L.N. Trefethen. Eigenvalues and pseudo-eigenvalues of Toeplitz matrices. *Lin. Alg. Applics.*, 162:153–185, 1992.

[82] M. Renardy. On the stability of differentiability of semigroups. *Semigroup Forum*, 51:343–346, 1996.

[83] O. Reynolds. An experimental investigation of the circumstances which determine whether the motion of water shall be direct or sinuous, and of the law of resistance in parallel channels. *Proc. Roy. Soc. Lond.*, 174:935–982, 1883.

[84] S. Roch and B. Silbermann. *C^*-algebra techniques in numerical analysis.* Preprint, 1994.

[85] M.M. Rogers and R.D. Moser. The three dimensional evolution of a plane mixing layer: The Kelvin Helmholtz rollup. *J. Fluid Mech.*, 243:183, 1992.

[86] V.A. Romanov. Stability of plane-parallel Couette flow. *Fun. Anal. Applic.*, 7:137–146, 1973.

[87] H. Salwen, F.W. Cotton, and C.E. Grosch. Linear stability of Poiseuille flow in a circular pipe. *J. Fluid Mech.*, 98:273–284, 1980.

[88] W.S. Saric. Görtler Vortices. *Ann. Rev. Fluid Mech.*, 26:137–146, 1994.

[89] P.J. Schmid and D.S. Henningson. A new mechanism for rapid transition involving a pair of oblique waves. *Phys. Fluids*, 4:1986–1989, 1992.

[90] R. Shanthini. Degeneracies of the temporal Orr–Sommerfeld eigenmodes in plane Poiseuille flow. *J. Fluid Mech.*, 204:13–34, 1989.

[91] J.D. Swearingen and R.G. Blackwelder. The growth and breakdown of streamwise vortices in the presence of a wall. *J. Fluid Mech.*, 182:255–290, 1987.

[92] N. Tillmark and P.H. Alfredsson. Experiments on transition in plane Couette flow. *J. Fluid Mech.*, 235:89–102, 1992.

[93] L.N. Trefethen. Pseudospectra of linear operators. In *ICIAM '95: Proceedings of the Third International Congress on Industrial and Applied Mathematics*. Akademie–Verlag, Berlin, 1995. Also to appear in *SIAM Review*.

[94] L.N. Trefethen. *Spectra and Pseudospectra: The Behavior of Non-Normal Matrices and Operators*. In preparation, 1996.

[95] L.N. Trefethen, A. Trefethen, S.C. Reddy, and T.A. Driscoll. Hydrodynamic stability without eigenvalues. *Science*, 261:578–584, 1993.

[96] F. Waleffe. On the three-dimensional instability of strained vortices. *Phys. Fluids*, 2:76–80, 1990.

[97] F. Waleffe. Hydrodynamic stability and turbulence: beyond transients to a self-sustaining process. *Stud. Appl. Math.*, pages 319–343, 1995.

[98] F. Waleffe. Non-linear normality versus non-normal linearity. *Phys. Fluids*, 7:3060–3066, 1995.

[99] F. Waleffe, J. Kim, and J. Hamilton. On the origin of streaks in turbulent shear flows. In *Turbulent Shear Flows 8*, pages 37–49. Springer–Verlag, 1993.

[100] I.J. Wyganski and F.H. Champagne. On transition in a pipe. Part 1. The origin of puffs and slugs and the flow in a turbulent slug. *J. Fluid Mech.*, 59:281–335, 1973.

[101] I.J. Wyganski, M. Sokolov, and D. Friedman. On transition in a pipe. Part 2. The equilibrium puff. *J. Fluid Mech.*, 69:283–304, 1975.

[102] Z. Yang. *A single streamwise vortical structure and its instability in shear flow*. PhD thesis, Harvard University, 1987.

[103] X. Yu and J.T.C. Liu. On the mechanism of sinuous and varicose modes in 3-dimensional viscous secondary instability of nonlinear Görtler rolls. *Phys. Fluids*, 6:736–750, 1994.

[104] J. Zabczyk. A note on C_0-semigroups. *Bull. Acad. Polon. Sci.*, 23:895–898, 1975.

[105] O.Y. Zikanov. On the instability of pipe Poiseuille flow. *To appear in Phys. Flu.*, 8(11), 1996.